Design of microlaser in medium infrarer wavelengnth range for biomedicine and environmental monitoring

Giuseppe Palma

ANNÉE 2017

THÈSE / UNIVERSITÉ DE RENNES 1
sous le sceau de l'Université Bretagne Loire

En Cotutelle Internationale avec
Politecnico di Bari, Italie

pour le grade de

DOCTEUR DE L'UNIVERSITÉ DE RENNES 1

Mention : Sciences des Matériaux

Ecole doctorale Sciences de la Matière

présentée par

Giuseppe Palma

préparée à l'unité de recherche 6226 ISCR
Institut des Sciences Chimiques de Rennes
UFR Sciences et Propriétés de la Matière

Design of microlaser in medium infrared wavelength range for biomedicine and environmental monitoring

Thèse rapportée par :

Mariola RAMIREZ
Professeur, Universidad Autónoma de Madrid / *rapporteur*

Brigitte BOULARD
Professeur, Université du Maine / *rapporteur*

et soutenue à Bari
le 20 avril 2017

devant le jury composé de :

Andrea CUSANO
Professeur, Università del Sannio / *examinateur*

Luca MAINETTI
Professeur, Università del Salento / *examinateur*

Guido PERRONE
Professeur, Politecnico di Torino / *examinateur*

Romano GIANNETTI
Professeur, Universidad Pontificia Comillas / *examinateur*

Francesco CORSI
Professeur, Politecnico di Bari / *examinateur*

Yann GUEGUEN
Maître de conférences, Université de Rennes1 / *examinateur*

Alla mia famiglia

La vita non è facile per nessuno. Ma cosa importa? Dobbiamo perseverare e soprattutto aver fiducia in noi stessi. Dobbiamo credere che siamo dotati di qualcosa e che questo qualcosa debba essere raggiunto.

Life is not easy for any of us. But what of that? We must have perseverance and above all confidence in ourselves. We must believe that we are gifted for something, and that this thing, at whatever cost, must be attained.

La vie n'est facile pour aucun de nous. Mais quoi, il faut avoir de la persévérance, et surtout de la confiance en soi. Il faut croire que l'on est doué pour quelque chose, et que, cette chose, il faut l'atteindre coûte que coûte.

Marie Curie

Number rules the universe

Pythagoras

Acknowledgements

I would like to thank my academic supervisor, Professor Francesco Prudenzano, for his support and guidance, which he has provided throughout my PhD. His scientific intuition and insights have always been very helpful. In addition to the scientific side, he has been a life mentor for me and I will be forever grateful for this.

I would like to thank also my academic supervisor in France, Professor Virginie Nazabal, and her collaborator Dr. Florent Starecki. They have provided me with invaluable help and great insights into different areas of Material Science. It has been a pleasure for me to stay in 'Glass and Ceramics group' of University of Rennes. They welcomed me from the first day and made me feel at home.

In addition I am honored to have had the opportunity to collaborate with Professor Loic Boidiou and Professor Joel Charrier from the 'Foton' group of University of Rennes, Professor Tetsuji Yano, Professor Tetsuo Kishi and Dr. Tsutaru Kumagai from the Tokyo Institute of Technology and Professor Gualtiero Nunzi Conti from the Institute of Applied Physics "Nello Carrara". I have greatly profited from their knowledge and experience.

I wish to thank a special group of people. During my academic path, I have interacted with other many colleagues with which I have shared successes as well as failures. I would like to thank: Giuseppe Caforio, William Scarcia, Emiliano Bianco, Piero Gigantiello, Stefano Nigri,

Giovanni Vitale and Christian Falconi. Special thanks go to Enza Portosi and Vito Recchia, they have supported and helped me many times.

I would like to thank Ilia Korolkov, Thomas Halenkovic and Deepak Patil, my best friends during my stays in France. The time spent with them has been great. I am fortunate to have met all of them.

Last but not least, I would like to thank my family and my long-standing friends. I wish to thank my parents, my mother Genny and my father Tommaso. I deeply admire them and I am very grateful to them for their support. I thank my brother Gianpiero with Maria, my sister Mariantonietta with Maurizio. They love and help me in any circumstances. I thank a lot my nephew Marco, he is a source of motivation for me and I am very proud of him.

I thank all my friends: Fabio and Concetta with the little Niccolò, Maria and Andrea and their parents. They enrich my life and make me feel part of a big family.

My academic path was quite long and hard, but with the support of all these people I was able to complete it.

It is to them, I wish to dedicate this thesis.

Bari, February 3rd 2017.

Ringraziamenti

Vorrei ringraziare innanzitutto il mio supervisore, il Professor Francesco Prudenzano, per essere stato mio sostegno e guida durante tutto il percorso di dottorato. La sua intuizione scientifica e la sua profonda conoscenza nel campo mi sono state di enorme aiuto. Lo ringrazio anche per il suo lato umano, per me è stato un modello di vita e gli sarò sempre grato.

Vorrei ringraziare anche il mio supervisore in Francia, la Professoressa Virginie Nazabal, ed il suo collaboratore Dr. Florent Starecki. Mi hanno fornito un aiuto prezioso e mi hanno introdotto nel campo a me poco conosciuto della Scienza dei Materiali. È stato un grande piacere essere stato ospitato dal gruppo "Glass and Ceramics" dell'Università di Rennes. Mi hanno accolto fin dal primo giorno e mi ha fatto sentire a casa.

Inoltre sono davvero onorato di aver avuto l'opportunità di collaborare con il Professor Loic Boidiou ed il Professor Joel Charrier del gruppo "Foton" dell'Università di Rennes, con il Professore Tetsuji Yano, con il Professore Tetsuo Kishi ed il Dr. Tsutaru Kumagai del Tokyo Institute of Technology e con il Professore Gualtiero Nunzi Conti dell'Istituto di Fisica Applicata "Nello Carrara". Ho fatto tesoro dalla loro conoscenza ed esperienza.

Desidero poi ringraziare un gruppo speciale di persone. Durante il mio percorso universitario, ho incontrato molti colleghi con i quali ho condiviso successi ed insuccessi. Vorrei ringraziare in particolare:

Giuseppe Caforio, William Scarcia, Emiliano Bianco, Piero Gigantiello, Stefano Nigri, Giovanni Vitale e Christian Falconi. Un ringraziamento particolare va a Enza Portosi e Vito Recchia, essi mi hanno sostenuto ed aiutato molte volte. Vorrei ringraziare inoltre Ilia Korolkov, Thomas Halenkovic e Deepak Patil, i miei più stretti amici durante i soggiorni in Francia. Il tempo trascorso con loro è stato straordinario. Mi ritengo davvero fortunato di aver conosciuto tutti loro.

Ultimo ma non meno importante, vorrei ringraziare la mia famiglia e i miei amici di vecchia data. Desidero ringraziare i miei genitori, mia madre Genny e mio padre Tommaso. Provo profonda ammirazione per loro e gli sono estremamente grato per il supporto che non mi hanno mai fatto mancare. Ringrazio mio fratello Gianpiero con Maria e mia sorella Mariantonietta con Maurizio, per il loro amore ed il loro sostengono in ogni circostanza. Ringrazio in particolare mio nipote Marco, mia fonte di motivazione e di cui sono estremamente orgoglioso.

Ringrazio poi tutti i miei amici: Fabio e Concetta con il piccolo Niccolò, Maria e Andrea ed i loro genitori. Arricchiscono la mia vita e mi fanno sentire parte di una grande famiglia.

Il mio percorso accademico è stato piuttosto lungo e difficile, ma con il supporto di tutte queste persone ho potuto completarlo.

È a tutti loro che voglio dedicare questa tesi.

Bari, 3 febbraio 2017.

Abstract

Optical micro-resonators represent one of the most important devices in photonics. A special kind is constituted by the WGM resonators, i.e. devices with circular symmetry such as spheres, rings, disks and toroids. They are characterized by very small dimensions, exceptionally quality factor and very low modal volume becoming a valuable alternative to the traditional optical micro-resonators, such as Fabry-Pérot cavities. These devices allow applications in several fields, such as sensing, optical filtering and nonlinear optics. In particular, different applications in biology and medicine, molecular spectroscopy, environmental monitoring, astronomy and astrophysics are feasible in Mid-Infrared wavelength range. For example, it includes a lot of strong vibrational transitions that act as "fingerprints" of many bio-molecules and organic species allowing the develop of innovative spectroscopic applications and novel sensors. In addition, the earth's atmosphere is transparent in two atmospheric transmission windows at 3–5 μm and 8–13 μm and then applications such as remote explosive detection, e.g. in airports and for border control, and covert communication systems are feasible. The wide transparency window of chalcogenide glasses in Mid-Infrared makes possible the development of several devices. Chalcogenide glasses are characterized by good mechanical strength and chemically durability in water and atmosphere. Furthermore, the high refractive index, high quantum efficiency, the low phonon energy and high rare-earth solubility enables the emissions at long wavelengths.

In this thesis, the design of innovative chalcogenide devices for applications in Mid-Infrared is investigated using an ad-hoc home-made computer code. The devices are based on three kinds of micro-resonators: microspheres, micro-disks and microbubbles. The WGM resonators are efficiently excited by using tapered fiber and ridge waveguides.

A novel design procedure is developed using the particle swarm optimization approach (PSO). It allows to maximize the gain of an amplifier based on an erbium-doped microsphere lasing at 2.7 μm.

An innovative technique in order to characterize the spectroscopic properties of rare-earth is developed integrating the WGM electromagnetic investigation with PSO algorithm. The method is based on two subsequent steps: in the first one, the geometrical parameters are recovered, in the second one, the spectroscopic parameters. The recovered values are affected by an error less than that provided by high-cost measurement instruments. Furthermore, the procedure is very versatile and could be applied to develop innovative sensing systems.

Interesting applications could be obtained exciting the micro-resonator by a tapered fiber with two identical LPGs on the sides. Indeed the LPGs can select the fiber modes coupling with the WGM resonator. Using different pairs of identical LPGs operating in different wavelength bands, it is possible to selective couple different micro-resonators by using the same optical fiber. An ad-hoc computer code is developed and validated and it demonstrated the feasibility of a microbubble glucose sensor.

In order to obtain a compact and cost-saving light source in Mid-Infrared, rare-earth doped micro-disk are investigated. A computer code is

developed in order to simulate a rare-earth doped micro-disk coupled to two ridge waveguide, one at signal wavelength and the other one at pump wavelength. The model is validated using an erbium-doped micro-disk emitting at 4.5 µm. A very promising device for application in Mid-Infrared is obtained using a praseodymium-doped micro-disk emitting at 4.7 µm.

Sintesi

I micro-risonatori ottici svolgono un ruolo importantissimo nella fotonica moderna. In particolare negli ultimi anni l'attenzione si è concentrata sui micro-risonatori a simmetria circolare, come ad esempio micro-sfere, micro-anelli, micro-dischi e micro-toroidi. Essi sono caratterizzati da dimensioni particolarmente ridotte, fattori di qualità eccezionalmente alti e volumi modali bassissimi diventando così una valida alternativa ai tradizionali micro-risonatori ottici come le cavità Fabry-Pérot. Questi dispositivi trovano applicazione in numerosi ambiti, come la sensoristica, il filtraggio ottico e l'ottica non lineare. Numerose ed interessanti sono le applicazioni di tali strutture nel medio infrarosso in ambiti come la biologia e la medicina, la spettroscopia molecolare, il monitoraggio ambientale, l'astronomia e l'astrofisica. Ad esempio, nel medio infrarosso si trovano numerose transizioni vibrazionali che agiscono come 'impronte digitali' di bio-molecole e specie organiche consentendo così lo sviluppo di innovative applicazioni spettroscopiche e di nuovi sensori. Inoltre, l'atmosfera terrestre presenta due finestre di trasparenza a 3 – 5 μm e 8 – 13 μm rendendo così possibili applicazioni come il rilevamento remoto di esplosivi, ad esempio in aeroporti e ai controlli di confine, e sistemi di telecomunicazioni protetti. Per sfruttare tali potenzialità, è necessario utilizzare vetri che siano trasparenti nel medio infrarosso, come ad esempio i vetri calcolgenuri. I vetri calcolgenuri sono caratterizzati da una buona resistenza meccanica e chimica in acqua e atmosfera. Inoltre presentano alto indice di rifrazione, alta efficienza

quantica, bassa phonon energy e alta solubilità alle terre rare consentendo l'emissione di luce alle alte lunghezze d'onda.

Obiettivo di questa tesi è stato la progettazione di innovativi dispositivi in vetro calcogenuro per applicazioni nel medio infrarosso utilizzando codice home-made scritto appositamente. L'attenzione si è concentrata su tre tipologie di dispositivi: micro-sfere, micro-dischi e micro-bolle. Per eccitare il campo elettromagnetico all'interno di queste strutture si possono utilizzare differenti metodi, ma i più efficienti fanno uso del campo evanescente di fibre ottiche rastremate (taper) o di guide d'onda opportunamente progettate.

Un primo ambito di ricerca ha riguardato lo sviluppo di una nuova procedura di progettazione di amplificatori a micro-risonatore utilizzando l'algoritmo particle swarm optimization (PSO). Tale approccio ha consentito di massimizzare il guadagno di un amplificatore realizzato da una micro-sfera drogata con Erbio che emette luce a 2.7 μm.

Una diversa attività di ricerca ha consentito di definire un innovativo approccio alla caratterizzazione spettroscopica delle terre rare integrando lo studio elettromagnetico dei WGM eccitati in una micro-sfera con l'algoritmo PSO. Il metodo è basato su due passaggi successivi: nel primo vengono recuperati i parametri geometrici della struttura, nel secondo i parametri spettroscopici. Il tool complessivo consente di ricavare i parametri spettroscopici con un errore minore di quello generalmente ottenuto utilizzando strumentazione di misura estremamente costosa. Inoltre la procedura sviluppata è estremamente

versatile e potrebbe essere applicata per progettare innovativi sistemi per la sensoristica.

Un'ulteriore attività ha riguardato le interessanti applicazioni che possono essere ottenute eccitando un micro-risonatore per mezzo di una fibra ottica rastremata avente due identici LPG (Long Period Grating) ai lati. Infatti gli LPG possono essere utilizzati per selezionare quale modo di core della fibra deve essere accoppiato con il risonatore WGM. Facendo uso di diverse coppie di LPG che lavorano a differenti lunghezze d'onda, è possibile accoppiare selettivamente differenti micro-risonatori utilizzando una stessa fibra ottica ed ottenendo così un sistema di sensing distribuito. Un codice ad-hoc è stato sviluppato e validato. Inoltre, sono stati condotti studi preliminari su sensori a micro-bolla che hanno dimostrato la fattibilità di un sensore sensibile alla concentrazione di glucosio.

Ultimo ambito di ricerca ha riguardato i sistemi laser basati su micro-dischi drogati con terre-rare. L'industria fotonica tende a privilegiare strutture planari perché più compatte, più facilmente integrabili e più economiche da realizzare. Anche in questo caso è stato sviluppato un codice numerico con lo scopo di simulare un micro-disco drogato con terre-rare e accoppiato a due guide d'onda di tipo ridge, una per il segnale utile ed una per il segnale di pompa. Il modello è stato validato utilizzando un micro-disco drogato con Erbio e che emette luce a 4.5 μm. Successivamente il modello è stato utilizzato per progettare un innovativo e promettente micro-disco drogato con Praseodimio e che emette a 4.7 μm.

Résumé

Les micro-résonateurs optiques comptent parmi les dispositifs les plus importants en photonique. Les résonateurs WGM sont assez particuliers. Il s'agit de composant présentant une symétrie circulaire comme c'est le cas des sphères, des anneaux, des disques et des tores. Les résonateurs WGM sont de très petites dimensions. Ils présentent un facteur de qualité exceptionnel et un volume modal très faible et constituent une alternative intéressante aux micro-résonateurs optiques traditionnels, tels que les cavités Fabry-Pérot. Ces appareils peuvent être utilisés dans plusieurs domaines, notamment la télédétection, le filtrage optique et l'optique non linéaire. D'autres applications sont possibles en biologie, médecine, spectroscopie moléculaire, surveillance environnementale, astronomie et astrophysique grâce à l'exploitation du rayonnement moyen infrarouge. Les micro-résonateurs optiques comportent un grand nombre de transitions vibrationnelles qui agissent comme des «empreintes» pour de nombreuses molécules organiques permettant le développement d'applications spectroscopiques innovantes et de nouveaux capteurs. Il convient de noter que l'atmosphère de la terre est transparente au niveau des deux fenêtres de transmission atmosphérique. La première est comprise entre 3 et 5 μm et la seconde entre 8 et 13 μm, ce qui rend possible des applications telles que la détection d'explosifs à distance dans les aéroports ou dans le cadre du contrôle aux frontières ainsi que le brouillage de communication

confidentielles. La large fenêtre de transparence en verres de chalcogénures dans le domaine spectral infrarouge rend envisageable le développement de nombreuses applications. Les verres de chalcogénure sont caractérisés par une bonne résistance mécanique et une durabilité chimique suffisante dans l'eau et l'atmosphère. Par ailleurs, l'indice de réfraction élevé, le rendement quantique élevé, l'énergie de phonon faible et la solubilité importante des terres rares permettent des émissions dans le domaine spectral du moyen IR.

Dans cette thèse, la conception de dispositifs innovants en chalcogénure pour des applications utilisant le moyen infrarouge est étudiée en utilisant un code d'ordinateur personnel formé de façon aléatoire. Les appareils reposent sur des trois types de micro-résonateurs : les microsphères, les micro-disques et les microbulles. Les résonateurs WGM sont efficacement excités à l'aide de fibres nervurées et de guides d'ondes optiques de forme conique.

Le nouveau procédé de conception est développé en utilisant la méthode d'optimisation par essaims particulaires (PSO). Elle permet de maximiser le gain d'un amplificateur reposant sur une microsphère d'émission laser dopée à l'erbium à 4,5 μm.

Une technique innovante permettant de caractériser les propriétés spectroscopiques de la terre rare intégrant la recherche électromagnétique en mode WGM grâce à l'algorithme PSO a été développée. La méthode est basée sur deux étapes successives : dans la première, les paramètres géométriques sont récupérés tandis que les paramètres spectroscopiques

le sont dans la seconde. Les valeurs récupérées sont entachées d'une erreur inférieure à celle prévue par les instruments de mesure ayant un coût élevé. La procédure est très polyvalente. Elle peut être appliquée à la conception de systèmes de détection innovants.

Des applications intéressantes peuvent être obtenues en excitant le micro-résonateur avec une fibre conique présentant deux LPG identiques sur les côtés. En effet, les FLP peuvent sélectionner le couplage de modes de fibre avec le résonateur WGM. En utilisant différentes paires de FLP identiques, opérant dans différentes bandes de longueurs d'onde, il est possible de coupler de façon sélective différents résonateurs à l'aide de la même fibre optique. Un code informatique aléatoire a été développé et validé. Il a démontré la faisabilité d'un capteur de microbulles de glucose.

Un microdisque en terre rare dopé est étudié pour obtenir une source de lumière compacte et économique dans l'infrarouge moyen. Un code informatique est développé afin de simuler un micro-disque de terre rare dopé et associé à deux guides d'ondes nervurés, un pour le signal et l'autre pour la pompe. Le modèle est validé à l'aide d'un micro-disque dopée à l'erbium émettant à 4,5 μm. Ce dispositif très prometteur pour des applications dans le moyen infrarouge est obtenu en utilisant un micro-disque de praséodyme dopé émettant à 4,7 μm.

Contents

Acknowledgements v

Ringraziamenti vii

Abstract ix

Sintesi xii

Résumé xv

Contents xviii

Introduction 1

Chapter 1 : Whispering Gallery Mode resonator 4

1.1. Introduction 4

1.2. Planar and spherical structures 5

1.3. Analytical model of a microsphere 6

1.4. Cylindrical resonator 11

1.4.1. Dielectric micro-disk 12

1.5. Whispering gallery mode Approximation 14

1.6. Losses in WGM micro-resonator 18

Chapter 2 : Rare-earth doped system 23

2.1. Introduction 23

2.2. Micro-resonator-based laser system 24

2.3. Coupling mode theory 25

2.4. Erbium-doped glass 29

2.5. Praseodymium-doped glass 34

Chapter 3 : Design of rare-earth doped microsphere amplifier for bio-sensing 37

3.1. Introduction 37

3.2. Particle Swarm Optimization (PSO) algorithm 38

3.3. Rare-earth doped chalcogenide microspheres 42
3.4. Synthesis of chalcogenide microspheres 45
3.5. Design of Er^{3+}:$Ga_5Ge_{20}Sb_{10}S_{65}$ microsphere amplifier 49
3.6. Summary 60
Chapter 4 : Modeling of microspheres for spectroscopic characterization 61
4.1. Introduction 61
4.2. Microsphere for characterization using PSO 62
4.3. Rare-earth spectroscopic characterization 64
4.3.1. Design of the erbium-doped amplifier for sensing 68
4.3.2. Rare-earth characterization via PSO algorithm 72
4.4. PSO convergence 78
4.5. Characterization sensibility to the input parameter 82
4.6. Summary 84
Chapter 5 : Enhanced optical sensing via microsphere WGM resonance 85
5.1. Introduction 85
5.2. Bio-detection via chalcogenide microspheres 86
5.3. Double step approach for optical sensing 89
5.4. Design of the set-up and simulated results 93
5.4.1. Design of the reference system RSS 93
5.4.2. Suitable choice of pump powers 98
5.4.3. Gain sensitivity to the fabrication tolerance 100
5.4.4. Gain sensitivity to rare-earth coefficients 103
5.5. CPSO characterization 106
5.6. Double-step CPSO: geometrical characterization 110

5.7. Double-step CPSO: rare-earth characterization 113
5.8. Summary 120
Chapter 6 : Design of microspheres and microbubbles for environmental and biological monitoring 121
6.1. Introduction 121
6.2. Sensing via microsphere and microbubble 122
6.3. Theory 123
6.3.1. Analytical model of a microsphere 125
6.3.2. Analytical model of a microbubble 128
6.4. Coupling mode theory 129
6.5. Numerical results 132
6.6. Summary 138
Chapter 7 : Rare-earth doped micro-disks for Mid-Infrared applications 139
7.1. Introduction 139
7.2. Rare-earth doped micro-disks 140
7.3. Erbium-doped micro-disks 142
7.3.1. Design of an erbium-doped micro-disk 144
7.3.2. Numerical results 147
7.4. Praseodymium-doped micro-disks 153
7.4.1. Design of a praseodymium-doped micro-disk 154
7.4.2. Numerical Results 162
7.5. Summary 169
Conclusions 170
List of publications 173
Bibliography 178

Introduction

Several applications in biology, molecular spectroscopy and environmental monitoring are feasible in Mid-Infrared wavelength range (between 2.5 and 25 μm). As example, many organic species and bio molecules exhibit strong vibrational transitions in this wavelength range. These transitions can be used as "fingerprints" in order to implement innovative spectroscopic and bio-molecular sensing devices. Furthermore, two atmospheric transmission windows in Mid-Infrared (at 3–5 μm and 8–13 μm) could allow applications such as innovative communication systems and remote explosive detection in airports or for border control.

Chalcogenide glass exhibits a wide transparent window in Mid-Infrared [1]. These innovative glasses are characterized by good mechanical strength, high refractive index, chemically durability in water and atmosphere, high nonlinearity, photosensitivity [1]. Furthermore, chalcogenide glasses have high rare-earth solubility, low phonon energy, large radiative decay rates and high quantum efficiency. Consequently, these glasses are suitable host material for efficient emission in Mid-Infrared at wavelengths that cannot be achieved with silica glass.

The role of optical resonators devices in modern photonics is considerably increased. These devices are fundamental in a wide variety of applications, such as sensing, optical filtering and nonlinear optics. In traditional optical micro-resonators, such as Fabry-Pérot cavities, the light oscillation is achieved by using mirrors. The main drawbacks of Fabry-Pérot cavities are the limited compactness and the high cost. The current photonics industry needs a high integration density. Fabry-Pérot cavities

do not fit for this request. In the last years, a feasible alternative approach has been the use of dielectric microcavities with circular symmetry such as rings, disks, spheres and toroids. The whispering gallery modes theory well-describes the light propagation in these structures [1]. WGMs in micro-resonators are excited using the evanescent field provided by prisms, waveguides or tapered optical fibers. WGM resonators are characterized by small diameters varying from micrometers to hundreds of micrometers, potentially low material absorption and minimal reflection losses. These characteristics involve extraordinary properties, such as very high power density, extremely small mode volume, very narrow spectral linewidth and very high quality factors Q [2].

In this thesis, sensors and light-emitting sources working in Mid-Infrared range are designed. These devices are based on WGM resonators made of chalcogenide glass. Using commercial and home-made software these devices are simulated. The home-made computer code modeling is based on electromagnetic mode analysis, the coupled mode theory and the rate equations describing the rare earth ions behavior.

The first chapter reports a brief introduction on WGM resonators.

The second chapter reports a description of rare-earth doped systems.

The third chapter reports an innovative method to design a rare-earth doped microsphere using a global optimization approach: particle swarm optimization.

The fourth and fifth chapters report a novel approach for the characterization of spectroscopic parameters of a rare-earth doped microsphere. The approach can be easily extended to other sensing systems.

The sixth chapter reports the design of a praseodymium-doped micro-disk in order to obtain a laser source in Mid-Infrared.

The seventh chapter reports a preliminary study of a home-made code simulating microsphere and microbubbles for bio-sensing applications.

Chapter 1

Whispering Gallery Mode resonator

1.1. Introduction

Micro-resonators with circular geometry supports a special kind of optical modes called whispering gallery mode (WGM). Light is confined via total internal reflection at the boundary between the micro-resonator dielectric surface and the surrounding medium [1]. The light travels for several hundreds of round trips along circular orbits. This originates peculiar properties, such as: very high power density, extremely small mode volume, very high quality factors Q and narrow spectral linewidth [2]. Furthermore, WGM resonators are characterized by very small sizes (diameters vary from several micrometers to hundreds of micrometers) and minimal reflection losses. All these properties make WGM resonators a valuable alternative to the traditional optical micro-resonators, such as the Fabry-Pérot cavities, because of their compactness and cost-saving manufacturing, basic properties in the current trend towards very high photonic integration density.

The evanescent field provided by different coupling techniques, e.g. via prisms, waveguides or tapered optical fibers is used to excite WGMs.

In the following sections, the WGM formalism is illustrated. Some characteristics of micro-resonators, such as losses, are discussed.

1.2. Planar and spherical structures

Whispering gallery modes are supported by circular geometries: spheres, disks, rings and toroids. In this work, the attention is focused on three types of micro-resonators: micro-disks, microspheres and microbubbles. Generally, planar structures like micro-disk are preferred in order to obtain high circuit integration, stability and cost-saving manufacturing. Indeed, these structures can be microfabricated onto wafer using conventional deposition and etching techniques. On one hand microspheres are less integrable but on the other hand they have some interesting properties: they are the simplest three-dimensional resonator (it is possible to fabricate silica microsphere just by melting the tip of a single-mode fiber), it is possible to create bubbles within water in order to obtain sensor or laser source, it is very easy to apply functional coating on a sphere.

It is important to remark that microspheres have very-high quality factors higher than 10^7 [3, 5] while micro-disk have quality factor in the range of 10^4-10^5 [4].

1.3. Analytical model of a microsphere

The electromagnetic analysis of a microsphere follows by finding the solutions of the Helmholtz equations:

$$\nabla^2 \overline{E} = -k^2 n_s^2 \overline{E} \qquad (1.1)$$
$$\nabla^2 \overline{H} = -k^2 n_s^2 \overline{H}$$

where $k = \omega\sqrt{\mu_0 \varepsilon_0}$ is the wave vector in vacuum, $n_s = \sqrt{\mu_r \varepsilon_r}$ is the uniform refractive index in the microsphere and $\overline{E}$, $\overline{H}$ are the electric and magnetic fields of the guided WGMs.

Because of the spherical symmetry of the structure, it is convenient to use spherical coordinate system as reported in Figure 1.1. The WGM propagation is along azimuthal direction ϕ.

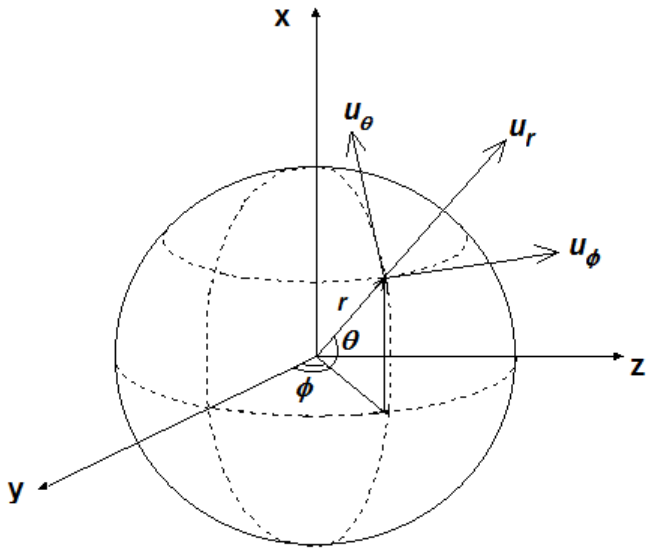

Fig. 1.1 Spherical coordinate system.

Applying separable solutions, two different cases can be identified:

- *Transverse electric mode* (**TE**): the electric field $\overline{E}$ is transverse to the propagation direction, and then the vector components are: $\vec{E} = E_\theta \hat{\theta}$, with $E_\phi \hat{\phi} = 0$ and $E_r \hat{r} = 0$;
- *Transverse magnetic mode* (**TM**): the magnetic field $\overline{H}$ is transverse to the propagation direction, and then the vector components are: $\vec{H} = H_\theta \hat{\theta}$, with $H_\phi \hat{\phi} = 0$ and $H_r \hat{r} = 0$.

From equation 1.1 follows the scalar Helmholtz equation:

$$\nabla^2 \Psi = -k^2 n_s^2 \Psi \tag{1.2}$$

where $\Psi = N_c E_\theta$ for the transverse electric (TE) modes, $\Psi = N_c H_\theta$ for the transverse magnetic (TM) modes. N_c is a normalization constant. It is related to the intensity flow through a plane transverse to the propagation direction ϕ. It is calculated by setting the volume integral of Ψ^2 over all the space, divided by the microsphere circumference, equal to unit [6].

Applying the separation of variable in spherical coordinates gives:

$$\Psi = \psi_r(r)\psi_\theta(\theta)\psi_\phi(\phi) \tag{1.3}$$

where $\Psi \in C^2$, $r \in [0,+\infty]$, $\theta \in \left[-\frac{\pi}{2}, \frac{\pi}{2}\right]$ and $\phi \in [0,2\pi]$.

Writing equation 1.2 in spherical coordinate and using separation of variable reported in 1.3 gives [7] equation 1.4:

$$\psi_\theta \psi_\phi \left(\frac{d^2 \psi_r}{dr^2} + \frac{2}{r} \frac{d\psi_r}{dr} \right) + \frac{\psi_r \psi_\phi}{r^2 \cos\theta} \frac{d}{d\theta} \left(\cos\theta \frac{d\psi_\theta}{d\theta} \right) \tag{1.4}$$

$$+ \frac{\psi_\theta \psi_r}{r^2 \cos^2\theta} \frac{d\psi_\phi^{\,2}}{d\phi^2} + k^2 n_s^2 \psi_r \psi_\theta \psi_\phi = 0$$

Equation 1.4 gives the subsequent equations system:

$$\frac{d^2\psi_r}{dr^2}+\frac{2}{r}\frac{d\psi_r}{dr}+\left(k^2n_s^2-\frac{C_1}{r^2}\right)\psi_r=0 \tag{1.5a}$$

$$\frac{1}{\psi_\theta\cos\theta}\frac{d}{d\theta}\left(\cos\theta\frac{d\psi_\theta}{d\theta}\right)-\frac{C_2}{\cos^2\theta}=-C_1 \tag{1.5b}$$

$$\frac{1}{\psi_\phi}\frac{d\psi_\phi{}^2}{d\phi^2}=C_2 \tag{1.5c}$$

where C_1 and C_2 are constants. Solving equations 1.5 leads to impose $C_2=-m^2$, $m\in\mathbf{z}$ and it is called azimuthal parameter; $C_1=l(l+1)$, l being a positive integer and it is called polar parameter.

The components of Ψ follow by solving equations 1.5 [8]:

$$\begin{aligned}
\psi_\phi(\phi)&=\exp[\pm jm\phi]\\
\psi_\theta(\theta)&=\exp\left[-\frac{|m|}{2}\theta^2\right]H_N\left(\sqrt{|m|}\theta\right) \qquad |m|>>1>>\theta\\
\psi_r(r)&=\begin{cases} j_l(kn_sr) & r\le R_s\\ \dfrac{j_l(kn_sR_s)}{k_l(kn_0R_s)}k_l(kn_0r) & r>R_s\end{cases}
\end{aligned} \tag{1.6}$$

R_s is the microsphere radius. The azimuthal dependence $\Psi_\phi(\phi)$ is expressed via a complex exponential function with argument depending on the mode number *m*. The approximation $\theta<<1$ for the polar angle has been considered because the predominant WGMs are those coupled via the fiber/waveguide close to the equatorial plane; the polar dependence $\Psi_\theta(\theta)$ is expressed by the Hermite polynomials H_N of order $N = l - m$. The radial solution $\Psi_r(r)$ is expressed by the spherical Bessel functions depending on the mode orders *l*. In particular j_l is the spherical Bessel

function of the first kind of the order l and k_l is the modified spherical Bessel function of the second kind of the order l.

Each $WGM_{l,m,n}^{sphere}$ is identified by three integers: l, m, n; $l-m+1$ is the number of field maxima in the polar direction $\hat{\theta}$; n is the number of field maxima along the radial direction. For any value of l, m can be: $|m| < l$. Modes with the same l and n and arbitrary m have the same resonant wavelength. The WGM with $m = l$ is called fundamental mode, i.e. the mode with the largest propagation constant in the direction of propagation: $\beta_m = m/R_s$. The propagation constant parallel to the microsphere surface is: $\beta_l = \sqrt{l(l+1)}/R_s$.

Using equations 1.6 and Maxwell's equations it is possible to obtain field components for TE and TM modes:

TE modes:

$$r \le R_s$$

$$\begin{cases} E_\theta = N_c J_l(kn_s r) e^{\pm jm\phi} e^{-\frac{|m|}{2}\theta^2} H_N\left(\theta\sqrt{|m|}\right) \\ H_\phi = \dfrac{j}{\omega\mu_0} N_c kn_s J_l'(kn_s r) e^{\pm jm\phi} e^{-\frac{|m|}{2}\theta^2} H_N\left(\theta\sqrt{|m|}\right) \\ H_r = \pm\dfrac{j}{\omega\mu_0}\cdot\dfrac{m}{r\cos\theta} N_c J_l(kn_s r) e^{\pm jm\phi} e^{-\frac{|m|}{2}\theta^2} H_N\left(\theta\sqrt{|m|}\right) \end{cases} \tag{1.7}$$

$$r > R_s$$

$$\begin{cases} E_\theta = N_c J_l(kn_s R_0) e^{\pm jm\phi} e^{-\frac{|m|}{2}\theta^2} H_N\left(\theta\sqrt{|m|}\right) \dfrac{j_l(kn_s R_s)}{k_l(kn_0 R_s)} k_l(kn_0 r) \\ H_\phi = \dfrac{j}{\omega\mu_0} N_c J_l(kn_s R_0) e^{\pm jm\phi} e^{-\frac{|m|}{2}\theta^2} H_N\left(\theta\sqrt{|m|}\right) kn_0 \dfrac{j_l(kn_s R_s)}{k_l(kn_0 R_s)} k_l'(kn_0 r) \\ H_r = \pm\dfrac{j}{\omega\mu_0}\cdot\dfrac{m}{r\cos\theta} N_c J_l(kn_s R_0) e^{\pm jm\phi} e^{-\frac{|m|}{2}\theta^2} H_N\left(\theta\sqrt{|m|}\right) \dfrac{j_l(kn_s R_s)}{k_l(kn_0 R_s)} k_l(kn_0 r) \end{cases} \tag{1.8}$$

TM modes:

$$r \le R_s$$

$$\begin{cases} H_\theta = N_c J_l(kn_s r) e^{\pm jm\phi} e^{-\frac{|m|}{2}\theta^2} H_N\left(\theta\sqrt{|m|}\right) \\ E_\phi = -\dfrac{j}{\omega\varepsilon_0 {n_s}^2} N_c kn_s J_l'(kn_s r) e^{\pm jm\phi} e^{-\frac{|m|}{2}\theta^2} H_N\left(\theta\sqrt{|m|}\right) \\ E_r = \mp\dfrac{j}{\omega\varepsilon_0 {n_s}^2} \cdot \dfrac{m}{r\cos\theta} N_c J_l(kn_s r) e^{\pm jm\phi} e^{-\frac{|m|}{2}\theta^2} H_N\left(\theta\sqrt{|m|}\right) \end{cases} \tag{1.9}$$

$$r > R_s$$

$$\begin{cases} H_\theta = N_c J_l(kn_s R_0) e^{\pm jm\phi} e^{-\frac{|m|}{2}\theta^2} H_N\left(\theta\sqrt{|m|}\right) \dfrac{j_l(kn_s R_s)}{k_l(kn_0 R_s)} k_l(kn_0 r) \\ E_\phi = -\dfrac{j}{\omega\varepsilon_0 {n_s}^2} N_c J_l(kn_s R_0) e^{\pm jm\phi} e^{-\frac{|m|}{2}\theta^2} H_N\left(\theta\sqrt{|m|}\right) kn_0 \dfrac{j_l(kn_s R_s)}{k_l(kn_0 R_s)} k_l'(kn_0 r) \\ E_r = \mp\dfrac{j}{\omega\varepsilon_0 {n_s}^2} \cdot \dfrac{m}{r\cos\theta} N_c J_l(kn_s R_0) e^{\pm jm\phi} e^{-\frac{|m|}{2}\theta^2} H_N\left(\theta\sqrt{|m|}\right) \dfrac{j_l(kn_s R_s)}{k_l(kn_0 R_s)} k_l(kn_0 r) \end{cases} \tag{1.10}$$

The boundary conditions applied to the tangential components of the electric and magnetic fields at the sphere/background interface are set in order to obtain the characteristic equation:

$$\begin{aligned} &\xi_s j_l(kn_s R_s)\left[-\frac{l}{kR_s} k_l(kn_0 R_s) + n_0 k_{l+1}(kn_0 R_s)\right] + \\ &+ k_l(kn_0 R_s)\left[\frac{l}{kR_s} j_l(kn_s R_s) - n_s j_{l+1}(kn_s Ro)_s\right] = 0 \end{aligned} \tag{1.11}$$

where:

$$\xi_s = \begin{cases} 1, & \text{TE modes} \\ \dfrac{n_s^2}{n_0^2} & \text{TM modes} \end{cases}$$

The solution of the characteristic equation leads to the calculation of the resonance wavelengths and their corresponding modal field distributions.

1.4. Cylindrical resonator

Figure 1.2 illustrates a circular waveguide. Under the hypothesis of wave propagation in z direction, the TE mode can be obtained using vector potential $\boldsymbol{F}$ [15] and imposing:

$$\boldsymbol{F} = \hat{z}F_z(\rho,\phi,z) \tag{1.12}$$

The vector wave equation is [15]:

$$\nabla^2 F_z(\rho,\phi,z) + \beta^2 F_z(\rho,\phi,z) = 0 \tag{1.13}$$

In cylindrical coordinates equation 1.13 gives:

$$\frac{\partial^2 F_z}{\partial \rho^2} + \frac{1}{\rho}\frac{\partial F_z}{\partial \rho} + \frac{1}{\rho^2}\frac{\partial^2 F_z}{\partial \phi^2} + \frac{\partial^2 F_z}{\partial z^2} + \beta^2 F_z = 0 \tag{1.14}$$

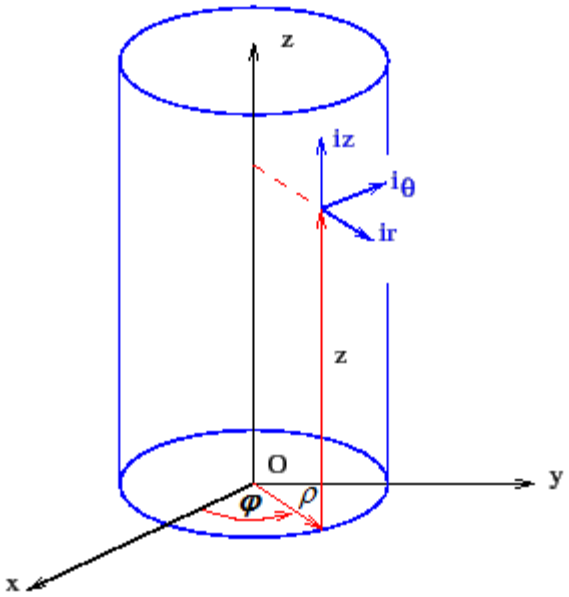

Fig. 1.2 Circular waveguide and cylindrical coordinate system.

The solution of equation 1.14 is expressed as following:

$$F_z(\rho,\phi,z) = \left[A_1 J_m(\beta_\rho \rho) + B_1 Y_m(\beta_\rho \rho)\right]\left[A_2 \cos(m\phi) + B_2 \sin(m\phi)\right] \times \left[A_3 \cos(\beta_z z) + B_3 \sin(\beta_z z)\right] \quad (1.15)$$

Where β_ρ is the propagation constant along radial direction ρ, β_z the propagation constant along longitudinal direction z and β the wave number. The dispersion equation is expressed in equation 1.16:

$$\beta_\rho^2 + \beta_z^2 = \beta^2 \quad (1.16)$$

In circular waveguides the boundary conditions are:

i) The fields must be finite everywhere. It follows that $B_1 = 0$;
ii) The fields must repeat every 2π radians along ϕ. It follows that $m = 0,1,2,3,\ldots$.

Applying the boundary conditions, equation 1.15 gives:

$$F_z(\rho,\phi,z) = A_1 J_m(\beta_\rho \rho)\left[A_2 \cos(m\phi) + B_2 \sin(m\phi)\right]\left[A_3 \cos(\beta_z z) + B_3 \sin(\beta_z z)\right] \quad (1.17)$$

1.4.1. Dielectric micro-disk

A cylindrical dielectric micro-resonator can be obtained considering two cross-sectional surface along z direction. Figure 1.3 illustrate the geometry of a dielectric micro-disk.

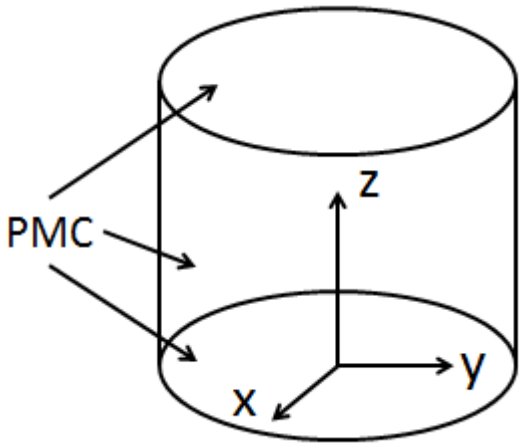

Fig. 1.3 Dielectric micro-disk.

A first-order approximation of this structure supposes a very high dielectric constant, 30 or greater [15]. Under this assumption, the interface between dielectric and air is like an open circuit and then there are internal total reflections. In this case, the dielectric – air interface can be approximate by a hypothetical perfect magnetic conductor (PMC).

An additional boundary condition for this kind of micro-disk is:

$$H_\phi\left(\rho = a, 0 \le \phi \le 2\pi, 0 \le z \le h\right) = 0 \tag{1.18}$$

Component H_ϕ of magnetic field can be expressed as [15]:

$$H_\phi = -i\frac{1}{\omega\mu_r\varepsilon_r}\frac{1}{\rho}\frac{\partial^2 F_z}{\partial\phi\partial z} =$$
$$= -iA_1\frac{m\beta_z}{\omega\mu_r\varepsilon_r}\frac{1}{\rho}J_m\left(\beta_\rho\rho\right)\left[-A_2\sin\left(m\phi\right)+B_2\cos\left(m\phi\right)\right]\cdot \tag{1.19}$$
$$\left[-A_3\sin\left(\beta_z z\right)+B_3\cos\left(\beta_z z\right)\right]$$

Applying the boundary condition expressed in equation 1.18 leads to the resonant frequency of the WGM:

$$f_{r,mnp} = \frac{1}{2\pi\sqrt{\mu_r \varepsilon_r}} \sqrt{\left(\frac{\chi_{mn}}{a}\right)^2 + \left(\frac{p\pi}{h}\right)^2} \tag{1.20}$$

χ_{mn} is the *n-th* zero of first kind Bessel function of *m* order.

Each $WGM_{m,n,p}^{disk}$ is identified by three integers:

- *m* is the azimuthal parameter: it represents the number of maximums in azimuthal direction ϕ;
- *p* is the longitudinal parameter: it represents the number of maximums in longitudinal direction *z*;
- *n* is the radial parameter: it represents the number of maximums in radial direction *r*.

1.5. Whispering gallery mode Approximation

An alternative approach in order to calculate the electromagnetic field in a micro-disk is the so-called whispering gallery mode approximation [9]. This method can be used in a preliminary and coarse design of the micro-disk. A refined design can be performed via a finite element method solver (FEM).

At first, the micro-disk is considered as 1D, slab waveguide, in order to calculate the effective refractive index n_{eff}. The structure is constituted by three layers: air, micro-disk and substrate. Air and substrate layers are considered semi-infinite. The micro-disk thickness is $h_{\mu disk}$. The micro-disk core has a refractive index higher than the other layers, so the total internal reflection occurs at each interface.

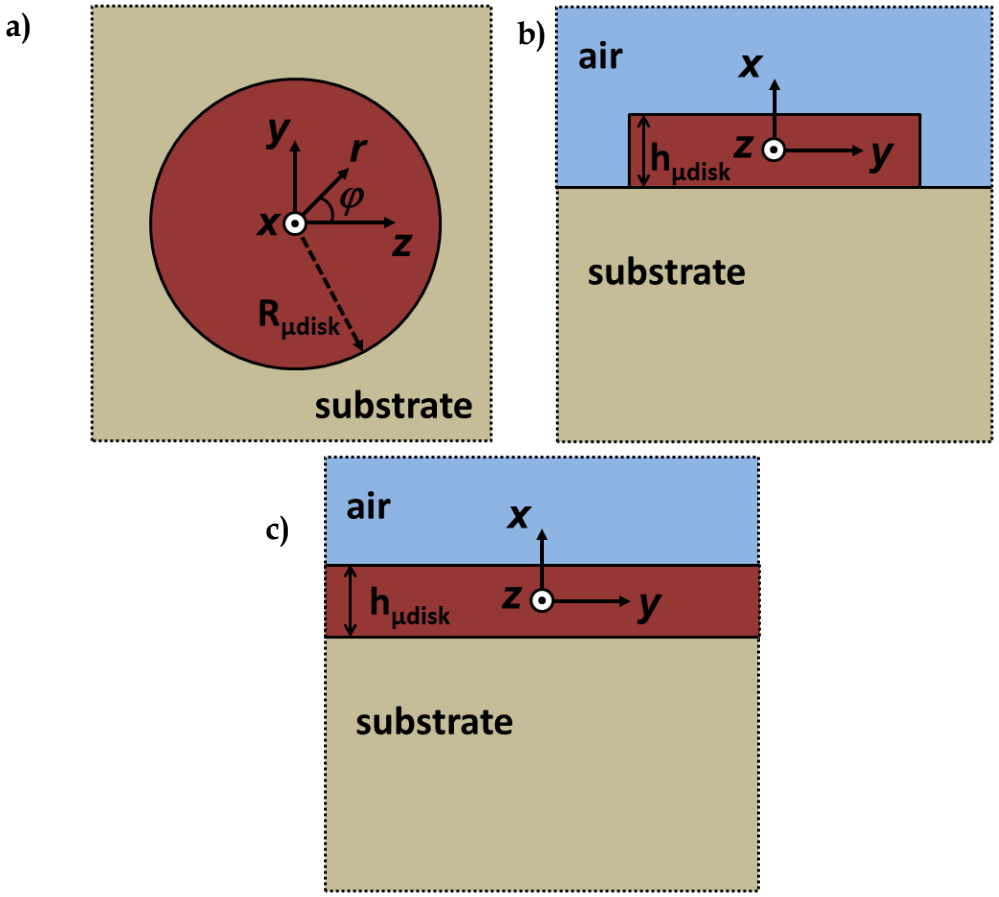

Fig. 1.4. a) Upper view and b) cross sectional view of a micro-disk. C)1D slab waveguide equivalent to the micro-disk.

Using the Cartesian coordinates reported in Figure 1.4, light propagates along z with an exponential variation $e^{-\gamma z}$. The waveguide is invariant along y. The electromagnetic analysis follows by finding the solutions of the Helmholtz equations in Cartesian coordinates:

$$\begin{aligned} \nabla^2 \overline{E} &= -k^2 \overline{E} \\ \nabla^2 \overline{H} &= -k^2 \overline{H} \end{aligned} \tag{1.21}$$

where $k = \omega\sqrt{\mu_0 \varepsilon_0}$ is the wave vector in vacuum and $\overline{E}$, $\overline{H}$ are the electric and magnetic fields of the guided modes. By considering the

transverse electric (TE) modes, the electric field components along x and z become negligible compared to y component. The Helmholtz equation can be simplified as follows:

$$\frac{\partial^2 E_{y,i}(x)}{\partial x^2} = \left(k_i{}^2 - \gamma^2\right) E_{y,i}(x) \tag{1.22}$$

where $E_{y,i}$ is the y component of the electric field $\overline{E}$, $k_i = \omega\sqrt{\mu_i \varepsilon_i}$ is the wave vector in the layer i, μ_i and ε_i the vacuum permeability and the permittivity in the layer i, $\gamma = kn_{eff}$ is the propagation constant along z, n_{eff} is the effective refractive index. By imposing the boundary conditions, the characteristic equation is obtained [10]:

$$\tan(\nu h) = \frac{\nu(\eta + \chi)}{\nu^2 - \eta\chi} \tag{1.23}$$

where:

$$\nu = \sqrt{n_{\mu disk}^2 k^2 - \gamma^2}$$

$$\eta = \sqrt{\gamma^2 - n_{subs}^2 k^2} \tag{1.24}$$

$$\chi = \sqrt{\gamma^2 - n_{air}^2 k^2}$$

$n_{\mu disk}$, n_{subs} and n_{air} are the refractive indexes of micro-disk, substrate and air respectively. Equation 1.23 cannot be solved analytically but using numerical methods in order to obtain the effective refractive index n_{eff} of the structure. Each solution is labeled with the parameter p. The parameter p represents the number of field maxima in the transversal direction x. This method applied to slab waveguide is generally known as EIM (effective index method) in x direction.

The effective refractive index n_{eff} is employed in the subsequent 2D analysis over the equatorial plane y - z involving the cylindrical Bessel functions equation [10]. The separation of the cylindrical variables r, φ (see Figure 1.4a) in Helmholtz equation allows to obtain the radial component of the electric field outside the micro-disk ($r > R_{\mu disk}$), as reported in equation 1.25 [10]:

$$E_r(r,\varphi) = NJ_m\left(\frac{2\pi}{\lambda_r} n_{eff} r\right) \cdot \exp\left(\frac{2\pi}{\lambda_r}\sqrt{n_{eff}^2 - n_{air}^2 (r-a)}\right) e^{jm\varphi} \tag{1.25}$$

where N is a constant obtained by imposing the boundary conditions, J_m is the Bessel function of the first kind of the order m, λ_r is the resonant wavelength and $R_{\mu disk}$ is the micro-disk radius. m is the azimuthal parameter and represents the number of electromagnetic field maxima in the azimuthal direction.

The boundary condition $E_r(r,\varphi) = 0$ for $r > R_{\mu disk}$ lead to equation 1.26:

$$E_r(r,\varphi) = 0 \Rightarrow J_m\left(\frac{2\pi}{\lambda_r} n_{eff} R_{\mu disk}\right) = 0 \tag{1.26}$$

By solving equation 1.26, the micro-disk radius $R_{\mu disk}$ and the azimuthal parameter m are calculated for each resonant wavelength λ_r. As mentioned in the previous section, each $WGM_{m,n,p}^{disk}$ in the micro-disk is characterized by the three parameter m, n and p. The radial parameter n is the number of field maxima along the radial direction.

This approach is simplified but allows to predict with good accuracy the resonant WGMs supported by the micro-disk. In order to perform a refined design, a valuable method is the use of a finite element method solver (FEM). It is useful especially in case of resonators with non-traditional geometry, such as micro-disk with edge inclination.

1.6. Losses in WGM micro-resonator

One of the most important advantage of cylindrical micro-resonators is the high value of the quality factor. In particular, microspheres have very-high quality factors better than 10^7 respect micro-disk whose quality factor is into the range of 10^4-10^5 because of the major optical losses due to the material and the technological process [3]. Furthermore, it was demonstrated chalcogenide-on-silicon mid-IR micro-resonators with intrinsic quality factor of $2x10^5$ at 5.2 μm [4].

A useful technique in order to fabricate micro-disk is using a standard photolithography process [3]. Surface-tension mold (StM) and localized-laser heating (LLH) techniques have been used to fabricate glass super spheres and true spheres, respectively [5].

The overall loss depends on different losses phenomena, but the most important are three:

i) losses due to the bulk *absorption* (described by quality factor Q_{abs});

ii) losses due to the *scattering radiation* (Q_{ss});

iii) losses due to the *tunneling* of light from micro-resonator (Q_{rad}).

The intrinsic quality factor Q can be calculated as report in equation 1.27 [14]:

$$\frac{1}{Q} = \frac{1}{Q_{abs}} + \frac{1}{Q_{ss}} + \frac{1}{Q_{rad}} \tag{1.27}$$

Q_{abs} is the quality factor due to the light absorption in the micro-disk and can be expressed as following [9]:

$$Q_{abs} = 2\pi n_{eff} / (\zeta \lambda_r) \tag{1.28}$$

where n_{eff} is the effective refractive index of the micro-resonator, ζ is a spatially averaged absorption coefficient and λ_r is the resonant wavelength.

Q_{ss} is the quality factor due to the surface scattering losses. In case of a micro-disk, scattering losses are due mostly to the irregularities on the micro-disk sidewalls, therefore the roughness on top and bottom surface can be neglected. Figure 1.5 illustrates upper view of a micro-disk having roughness on sidewalls.

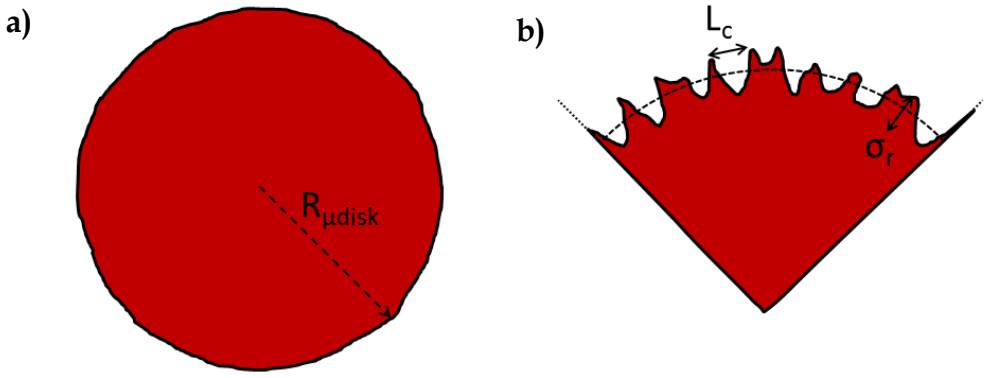

Fig. 1.5 a) Upper view of a micro-disk with roughness. b) Enlarged image of the micro-disk. L_c is the correlation length and σ_r is standard deviation of the roughness amplitude. Adapted from [14].

For a micro-disk, the quality factor due to the scattering radiation can be expressed as [14]:

$$Q_{ss} = \frac{3\lambda_r^3}{8\pi^{7/2} n_{air}\left(n_{\mu disk}^2 - n_{airk}^2\right)\vartheta} \frac{V_{\mu disk}}{V_{ss}} \tag{1.29}$$

where

$$\vartheta = \frac{n_{eff}^2\left(n_{\mu disk}^2 - n_{air}^2\right)}{n_{\mu disk}^2\left(n_{eff}^2 - n_{air}^2\right)}$$
$$V_{ss} = \sqrt{R_{\mu disk} L_c}\, h_{\mu disk} \sigma_r \tag{1.30}$$

ϑ is defined dielectric contrast constant, n_{eff} is the effective refractive index of the equivalent 2D waveguide of the micro-disk, $V_{\mu disk}$ is the volume of the micro-disk, V_{ss} is the effective volume of a typical scatterer, L_c and σ_r are the correlation length and standard deviation of the roughness amplitude, respectively.

Q_{rad} is the quality factor due to the stored internal energy. It is related to the tunneling of light along the curvature of the micro-resonators. It can be calculated as following [15]:

$$Q_{rad} = \omega \frac{2W_e}{P_{rad}} = \omega \frac{2W_m}{P_{rad}} \tag{1.31}$$

where W_e and W_m are electric and magnetic energy in the micro-disk, respectively; P_{rad} is the radiated power.

For a microspherical resonator, P_{rad} can be obtained by volume current method [6]. Actually, this method is used in order to calculate the far field from the near field in antenna problems. Indeed, it is possible to relate the far field with the oscillating sources. In microspherical resonator, the volume current density distribution can be expressed as [6]:

$$\vec{J}(r,\theta,\phi) = \varepsilon_0 \omega \left(n_s^2 - n_0^2\right) \vec{E}(r,\theta,\phi) \tag{1.32}$$

Where ε_0 is the vacuum permittivity and ω is the WGM frequency. The vectorial potential $\vec{A}$ is given in equation 1.33 [6]:

$$\vec{A} = \mu_0 \int_{V'} G\left(\vec{r},\vec{r}\,'\right) J dV' \tag{1.33}$$

where $G(\vec{r},\vec{r}')$ in the scalar Greens function and μ_0 the vacuum permeability. The Poynting vector in radial direction is:

$$S_r = \frac{k n_0 \omega}{2\mu_0} |A_\theta|^2 \tag{1.34}$$

where A_θ is the component of A along θ direction. The radiated power is given by the integral of Poynting vector over a spherical surface of radius *r* divided by the circumference:

$$P_{rad} = \frac{\iint S_r r^2 \cos\theta d\theta d\phi}{2\pi R_s} \tag{1.35}$$

For a microsphere, considering that the tunneling radiation is centered close to the equatorial plane ($\theta \approx 0$) and that the guided power is normalized, the Q_{rad} can be expressed as in equation 1.36 [6]:

$$Q_{rad} = \frac{l^2 n_s}{k^3 c \varepsilon_0 N_c^2 n_0^2 R_s^5 Z_0}$$

$$\cdot \left[n_0 \left(\frac{\pi}{\gamma_1} \right)^{1/4} j_l(kn_s R_s) j_{l+1}(kn_0 R_s) - n_s \left(\frac{\pi}{\gamma_2} \right)^{1/4} j_{l-1}(kn_s R_s) j_l(kn_0 R_s) \right]^{-2} \tag{1.36}$$

where:

$$\gamma_1 = l - \frac{1}{2} - kn_0 R_s \frac{j_l(kn_0 R_s)}{j_{l-1}(kn_0 R_s)} + \frac{(kn_0 R_s)^2}{l}$$
$$\gamma_2 = l + \frac{1}{2} - kn_0 R_s \frac{j_{l+2}(kn_0 R_s)}{j_l(kn_0 R_s)} + \frac{(kn_0 R_s)^2}{l} \tag{1.37}$$

Finally, the intrinsic lifetime related to the total power loss is expressed in equation 1.38:

$$\tau_0 = Q/\omega \tag{1.38}$$

Chapter 2

Rare-earth doped system

2.1. Introduction

Rare-earth elements are usually used as active emission centers in passive crystalline and amorphous materials. For the Near-Infrared there are a lot of devices that allow efficient lasing in silica glass using erbium and neodymium. Silica glass becomes opaque beyond 2 μm instead rare-earth ions exhibits useful transitions between 3 and 10 μm. Therefore, in order to obtain lasing in mid-Infrared wavelength range, other materials that are transparent at these wavelengths and have low phonon energy are required. Optimal results are obtained with chalcogenide glasses that have a wide transparent window in mid-Infrared. They combine a high rare-earth solubility with low phonon energy and transparency in mid-Infrared. Moreover, chalcogenide glasses have other properties that promote lasing action such as high refractive index for high absorption and emission cross section, good mechanical strength and chemically durability in water and atmosphere [16, 93-96]. A wide literature exists about rare-earths doped chalcogenide glasses. Lasing chalcogenide glasses doped with neodymium and thulium are reported below 3 μm [18, 97-99], dysprosium luminesce is used in a chalcogenide sensor of CO_2 [18, 69, 100], erbium doped micro-resonator lasing at 3.6 μm is developed [19], luminescence in praseodymium doped selenide-based chalcogenide glass has been obtained [20].

In the following sections, the micro-resonator-based laser systems are illustrated. The coupled mode theory is introduced. Finally, the model of erbium and praseodymium-doped glasses is described.

2.2. Micro-resonator-based laser system

A micro-resonator-based laser system consists of a micro-resonator coupled to two fibers/waveguides, one for the signal at wavelength λ_s and one for the pump at wavelength λ_p. The evanescent field of fiber/waveguide excites the WGMs in the micro-resonators. Therefore, the waveguides introduce and collect the light from the micro-resonator. The micro-resonator is doped with a rare-earth element. The interactions of both pump and signal beams with the rare-earth doped glass allow the signal optical amplification. Figure 2.1 shows a typical scheme of a micro-disk coupled to two waveguides.

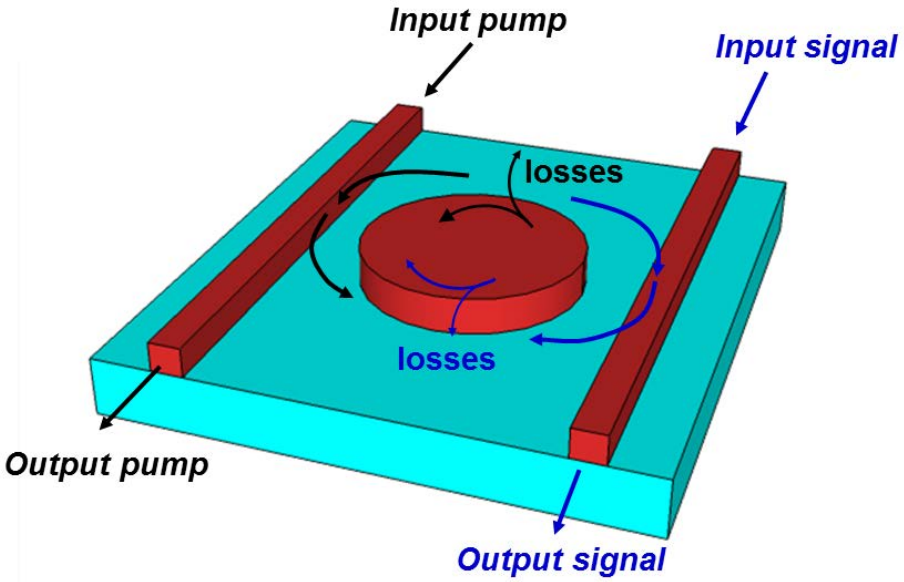

Fig. 2.1 Rare-earth doped micro-disk coupled to two ridge-waveguides.

2.3. Coupling mode theory

The coupling of the optical power between the micro-resonator and a fiber /waveguide is modeled by using the coupled mode theory [11-13]. The coupled-mode equations are obtained by considering: weak coupling, small internal resonator losses, small perturbation of optical fiber and resonator modes, slowly varying amplitude approximation, single mode fiber /waveguide coupled to a WGM of the cavity, adiabatic tapered fiber/waveguide, coupling region much smaller than the micro-resonator diameter.

Figure 2.2 illustrates a sketch of the coupling system. As example, a rare-earth doped micro-disk coupled to two ridge waveguide is used. As described in chapter 1, each WGM is characterized by three modal number. In case of microsphere structure, the modal number are: *l*,*m*,*n*, in case of micro-disk they are *m*,*n*,*p*.

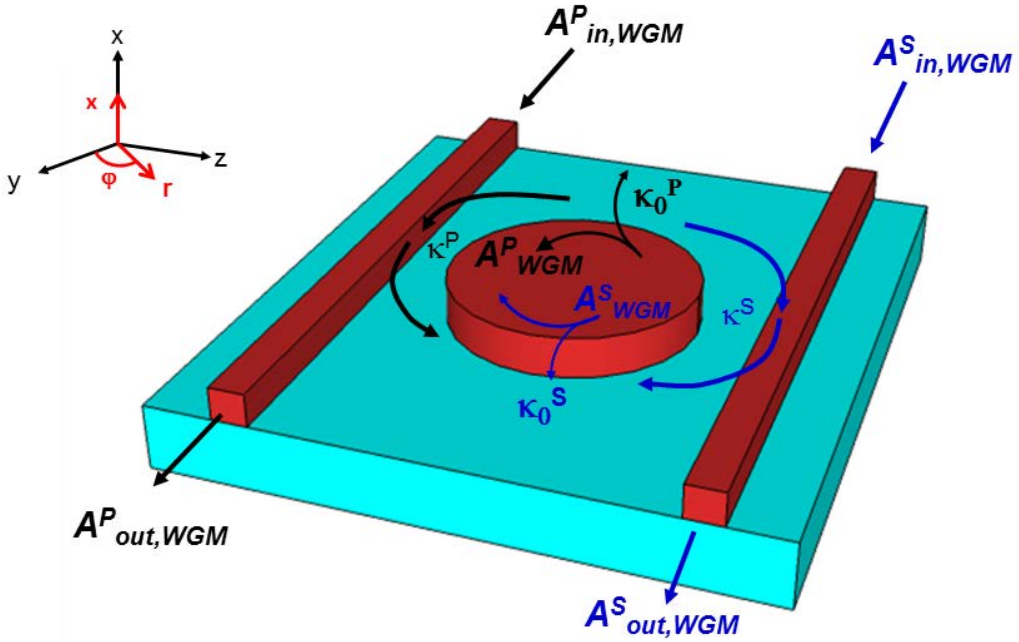

Fig. 2.2 Layout sketch of the chalcogenide micro-disk coupled to two ridge waveguide.

The rate equations describing the time evolutions of the amplitude of electromagnetic field in the micro-resonator are written as function of:

i) the contribution to the pump and signal rates of each WGM propagating into the microsphere;

ii) N_i , the concentration of ions in *i*-th level of the rare-earth element.

The time domain evolution of the amplitude *A* for the pump *P* and the signal *S* of the internal cavity electromagnetic field can be obtained by solving the following differential equations [12] [21-26]:

$$\frac{dA_{WGM}^{P}}{dt} = \left(-\frac{2}{\tau_{ext}} - \frac{1}{\tau_0} - g_{WGM}^{P} + i\Delta\omega \right) A_{WGM}^{P} - i\sqrt{\frac{2}{\tau_{ext}\tau}} A_{in,WGM}^{P}$$

$$\frac{dA_{WGM}^{S}}{dt} = \left(-\frac{2}{\tau_{ext}} - \frac{1}{\tau_0} - g_{WGM}^{S} + i\Delta\omega \right) A_{WGM}^{S} + \frac{c}{2n_{eff}} \sum_{q} N_i \, \sigma_{ji}(\omega_{WGM}) \Omega_{WGM}^{S} A_0 - i\sqrt{\frac{2}{\tau_{ext}\tau}} A_{in.WGM}^{S} \tag{2.1}$$

g_{WGM}^{y}, with y = *P*, *S*, is the optical gain due to the rare-earth/light interaction related to a certain WGM and it is expressed in equation 2.2:

$$g_{WGM}^{y} = \frac{c}{2n_{eff}} \left[N_i \, \sigma_{ji}(\omega_{WGM}) \Omega_{WGM}^{y} - N_i \, \sigma_{ij}(\omega_{WGM}) \Omega_{WGM}^{y} \right] \quad \text{with } y = P, S. \tag{2.2}$$

$A_{in,WGM}^{y}$ and $A_{out,WGM}^{y}$ are the amplitudes of mode electric field at the input and at the output fiber/waveguide section and coupled with the

WGM mode of the micro-resonator; A^{y}_{WGM} is the slowly varying amplitude scaling the normalized electric field E^{y}_{WGM} on the cross-sectional plane; N_i is the ion population concentration of *i*-th energy level; $\tau = 2\pi\rho_0 n_{eff}/c$ is the circulation time inside the micro-resonator; ρ_0 is the micro-resonator radius, n_{eff} is the WGM effective refractive index, *c* the speed of light in vacuum; ω_{WGM} is the WGMs resonant frequency; $\Delta\omega = \omega_{in} - \omega_{WGM}$ is the frequency detuning of the input signal from the WGM resonance frequency; $\tau_0 = 1/\kappa_0^2 = Q/\omega_{WGM}$ is the intrinsic lifetime, Q is the intrinsic quality factor (see section 1.6) and κ_0 is the intrinsic cavity decay rate; τ_{ext} is the coupling lifetime; $\sigma_{ij}(\omega_{WGM})$ is the rare-earth cross-section at frequency ω_{WGM} from level *i* to level *j*.

Ω^{y}_{WGM} is the overlap factor of each WGM with the rare-earth profile inside the doped region A_d and it is expressed in equation 2.3:

$$\Omega^{y}_{WGM} = \iint_{A_d} \left| E^{y}_{WGM} \right|^2 ds \qquad \text{with } y = P, S. \tag{2.3}$$

where E^{y}_{WGM} is the normalized electric field on the cross-sectional plane.

τ_{ext} is the coupling lifetime which denotes the coupling strength between the micro-resonator and the waveguide. It is expressed in 2.4:

$$\tau_{ext} = \frac{2\tau}{\kappa^2} \tag{2.4}$$

where κ is the so-called cavity decay rate or coupling coefficient and it is derived by the overlap integral in the all-space volume *V* between the electromagnetic field of the fiber/waveguide guided mode and the micro-resonator WGM [6]:

$$\kappa = k^2 \frac{n_{\mu reson}^2 - n_{air}^2}{2\gamma_{fw}} \int_V \overline{E}_{fw} \cdot \overline{E}_{\mu reson}^* \tag{2.5}$$

$k = \omega_{WGM} \sqrt{\mu_0 \varepsilon_0}$ is the wave vector in vacuum; $n_{\mu reson}$ and n_{air} are the refractive index of micro-resonator and air, respectively; $\overline{E}_{fw}$ and $\overline{E}_{\mu reson}$ are the electric field in the fiber/waveguide and in the micro-resonator, respectively; γ_{fw} is the propagation constant of the fiber/waveguide along *z* direction. Normalization power is applied to $\overline{E}_{fw}$ and $\overline{E}_{\mu reson}$, i.e. the power flow through a cross section is equal to 1W:

$$\begin{aligned} \iint_{cross-section} \left|\overline{E}_{fw}\right|^2 ds = 1 \\ \iint_{cross-section} \left|\overline{E}_{\mu rison}\right|^2 ds = 1 \end{aligned} \tag{2.6}$$

WGMs with higher spatial overlap with the fiber/waveguide have their power bounded near the equatorial plane, therefore they have the radial modal number *n*=1 and a little excursion along polar direction (*m*=*l* in case of microsphere, p=1 in case of micro-disk).

The electromagnetic field in the micro-resonator and in the fiber/waveguide used in equation 2.5 and the propagation constants can be obtained using a FEM solver or the analytical procedure explained in chapter 1.

The gain g of the amplifier is [13]:

$$g = \left| \frac{A^{y}_{out,WGM}}{A^{y}_{in,WGM}} \right|^2 = \left| \sqrt{1 - \frac{\tau}{\tau_{ext}}} + j\sqrt{\frac{\tau}{\tau_{ext}}} \frac{A^{y}_{WGM}}{A^{y}_{in,WGM}} \right|^2 \qquad (2.7)$$

with $y = P, S$.

2.4. Erbium-doped glass

The interaction of the WGMs with the rare-earth doped micro-resonator has been investigated by using the rate equation model. In erbium model (see Figure 3.3), the manifolds $^4F_{7/2}$, $^2H_{11/2}$ and $^4S_{3/2}$ constitute the level L_6 because $^2H_{11/2}$ and $^4S_{3/2}$ are thermally distributed and the transition $^4F_{7/2} \rightarrow {}^2H_{11/2}$ is very fast. Furthermore, the Er^{3+}-doped system is complex because the levels $^4I_{13/2}$, $^4I_{11/2}$ and $^4I_{9/2}$ have comparable ions lifetime and the lifetime of $^4F_{9/2}$ is not negligible. The electronic transitions and the energy transfers of the trivalent erbium ions in the chalcogenide glass have been taken into account, i.e. the ($^4I_{15/2} \rightarrow {}^4I_{11/2}$) pump transition at the wavelength 0.98μm, the ($^4I_{15/2} \rightarrow {}^4I_{9/2}$) pump transition at the wavelength 0.806μm, the ($^4I_{9/2} \rightarrow {}^4I_{11/2}$) stimulated emission transition at the wavelength 4.5μm, the ($^4I_{11/2} \rightarrow {}^4I_{13/2}$) stimulated emission transition at the wavelength 2.7μm, the ($^4I_{13/2} \rightarrow {}^4I_{15/2}$) stimulated emission transition at the wavelength 1.55μm, the spontaneous energy transfer mechanisms occurring in a pair of Er^{3+} ions, ($^4I_{13/2}$, $^4I_{13/2} \rightarrow {}^4I_{15/2}$, $^4I_{9/2}$), ($^4I_{11/2}$, $^4I_{11/2} \rightarrow {}^4I_{15/2}$,$^4S_{3/2}$), ($^4I_{15/2}$, $^4I_{9/2} \rightarrow {}^4I_{13/2}$), ($^4I_{9/2}$, $^4I_{9/2} \rightarrow {}^4S_{3/2}$,$^4I_{13/2}$), ($^4I_{15/2}$, $^4S_{3/2} \rightarrow {}^4I_{13/2}$, $^4I_{9/2}$), ($^4I_{13/2}$, $^4I_{9/2} \rightarrow {}^4I_{15/2}$, $^4S_{3/2}$).

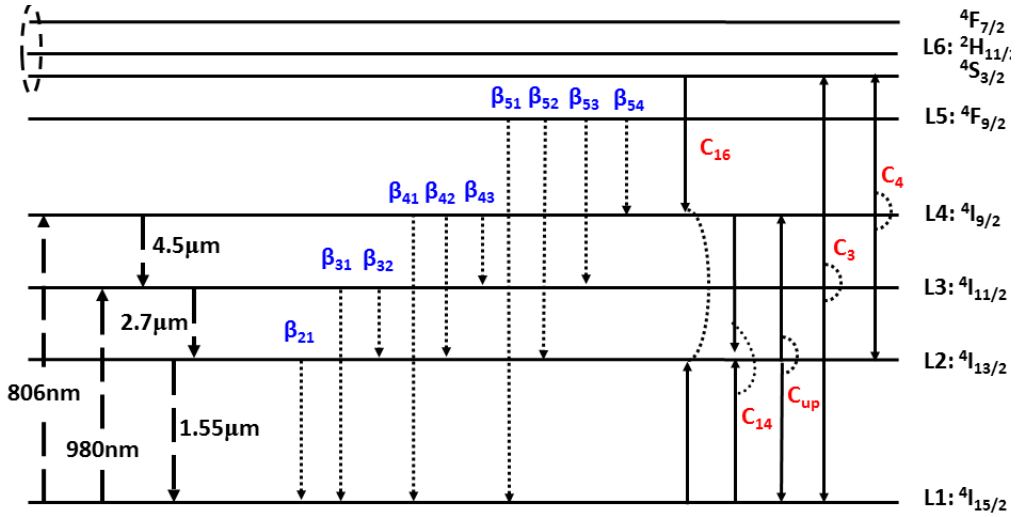

Fig. 2.3 Erbium energy level diagram.

The most important phenomena of rare-earth/light interaction are taken into account in the subsequent rate equations:

$$
\begin{cases}
\dfrac{dN_1}{dt} = N_2\left(W_{21} + C_{22}N_2 + C_{42}N_4 + A_{21} + \Gamma_{21}\right) + N_3\left(R_{31} + C_{33}N_3 + A_{31} + C_{35}N_3\right) + N_4\left(C_{14}N_1 + A_{41}\right) + \\
\quad + N_5A_{51} + N_6A_{61} + N_7A_{71} - N_1\left(R_{13} + W_{12} + C_{15}N_5 + C_{51}N_5 + C_{16}N_6 + C_{41}N_4 + C_{14}N_4\right) \\
\dfrac{dN_2}{dt} = N_5\left(R_{52} + A_{52} + C_{15}N_1\right) + N_6A_{62} + N_7A_{72} + N_4\left(W_{42} + A_{42} + C_{41}N_1 + C_{44}N_4\right) + N_3\left(A_{32} + \Gamma_{32}\right) + \\
\quad + N_1\left(W_{12} + C_{51}N_5 + C_{41}N_4 + C_{16}N_6\right) - N_2\left(W_{21} + R_{25} + W_{24} + C_{42}N_4 + 2C_{22}N_2 + A_{21} + \Gamma_{21}\right) \\
\dfrac{dN_3}{dt} = N_7\left(A_{73} + R_{73}\right) + N_6\left(C_{16}N_1 + A_{63}\right) + N_5A_{53} + N_4\left(\Gamma_{43} + A_{43}\right) + N_1R_{13} - \\
\quad - N_3\left(R_{31} + R_{37} + 2C_{33}N_3 + 2C_{35}N_3 + A_{31} + A_{32} + \Gamma_{32}\right) \\
\dfrac{dN_4}{dt} = N_5\left(A_{54} + C_{51}N_1 + \Gamma_{54}\right) + N_6A_{64} + N_7A_{74} + N_2\left(W_{24} + C_{22}N_2\right) + N_1\left(C_{15}N_5 + C_{14}N_4\right) - \\
\quad - N_4\left(W_{42} + C_{14}N_1 + A_{41} + A_{42} + A_{43} + \Gamma_{43} + C_{41}N_1 + 2C_{44}N_4 + C_{42}N_2\right) \\
\dfrac{dN_5}{dt} = N_7A_{75} + N_6\left(A_{65} + \Gamma_{65}\right) + N_4\left(C_{44}N_4 + C_{42}N_2\right) + N_3\left(C_{35}N_3\right) + N_2R_{25} - \\
\quad - N_5\left(R_{52} + A_{51} + A_{52} + A_{53} + A_{54} + \Gamma_{54} + C_{51}N_1 + C_{15}N_1\right) \\
\dfrac{dN_6}{dt} = N_7\left(A_{76} + \Gamma_{76}\right) - N_6\left(C_{16}N_1 + A_{61} + A_{62} + A_{63} + A_{64} + A_{65} + \Gamma_{65}\right) \\
N_{tot} = N_1 + N_2 + N_3 + N_4 + N_5 + N_6 + N_7
\end{cases}
\tag{2.8}
$$

The spontaneous emission rate between level *i* and *j* is expressed in 2.9:

$$A_{ij} = \frac{\beta_{ij}}{\tau_i} \tag{2.9}$$

where β_{ij} is the branching ratio between level *i* and *j*, τ_i the ions lifetime of level *i*.

C_{ij} represent the spontaneous energy transfer mechanisms.

W_{ij} is the signal transition rate and R_{ij} is the pump transition rate. They represent the contribution to the signal and pump rate of each WGM propagating into the micro-resonator and are expressed as following [12]:

$$W_{ij}^{WGM} = \frac{\sigma_{ij}(\omega_{WGM})}{h\omega_{WGM} A_d} \iint_{A_d} I_{WGM}^{S} ds \qquad R_{ij}^{WGM} = \frac{\sigma_{ij}(\omega_{WGM})}{h\omega_{WGM} A_d} \iint_{A_d} I_{WGM}^{P} ds \tag{2.10}$$

where σ_{ij} is the emission cross section at the frequency ω_{WGM} if $i > j$, the absorption cross section at the frequency ω_{WGM} if $i < j$; h is the Planck constant; A_d is the doped region; I_{WGM}^{y}, with $y = P, S$, is the intensity profile at signal *S* and pump *P* frequency.

It is apparent that $\iint_{A_d} I_{WGM}^{y} ds \Big/ A_d$ represents the average value of the intensity profile. The intensity profile can be expressed in terms of electric field [22]:

$$I_{WGM}^{y} = \frac{1}{2} \varepsilon_0 c n_{eff} \left| A_{WGM}^{y} \right|^2 \left| E_{WGM}^{y} \right|^2 \tag{2.11}$$

with $y = P, S$.

where A^{y}_{WGM} is the slowly varying amplitude of equation 2.1 and E^{y}_{WGM} is the normalized electric field on the cross-sectional plane.

Using eq. 2.11 in 2.10 gives:

$$W_{ij}^{WGM} = \frac{\sigma_{ij}(\omega_{WGM})}{2h\omega_{WGM}A_d}\varepsilon_0 cn_{eff}\left|A^{S}_{WGM}\right|^2\Omega^{S}_{WGM}$$
$$R_{ij}^{WGM} = \frac{\sigma_{ij}(\omega_{WGM})}{2h\omega_{WGM}A_d}\varepsilon_0 cn_{eff}\left|A^{P}_{WGM}\right|^2\Omega^{P}_{WGM} \qquad (2.12)$$

$\Omega^{y}_{WGM} = \iint_{A_d}\left|E^{y}_{WGM}\right|^2 ds$, with $y = P, S$, is the overlap factor between each WGM and rare-earth profile as defined in equation 2.3.

Table 2.1 reports the spectroscopic parameter measured on erbium doped chalcogenide glass $Ga_5Ge_{20}Sb_{10}S_{65}$ [12-13, 27-28].

Table 2.1 Spectroscopic parameters of the Er^{3+}-doped chalcogenide glass [12-13, 27-28]

Energy level transitions	Wavelength [nm]	Lifetime [ms]	Branching ratio [%]
$^4I_{13/2} \rightarrow {}^4I_{15/2}$	1532	$\tau_2 = 1.83$	$\beta_{21} = 100.0$
$^4I_{11/2} \rightarrow {}^4I_{15/2}$	986	$\tau_3 = 1.37$	$\beta_{31} = 86.28$
$^4I_{11/2} \rightarrow {}^4I_{13/2}$	2771		$\beta_{32} = 13.72$
$^4I_{9/2} \rightarrow {}^4I_{15/2}$	810	$\tau_4 = 1.08$	$\beta_{41} = 80.38$
$^4I_{9/2} \rightarrow {}^4I_{13/2}$	1719		$\beta_{42} = 18.82$
$^4I_{9/2} \rightarrow {}^4I_{11/2}$	4529		$\beta_{43} = 0.80$
$^4F_{9/2} \rightarrow {}^4I_{15/2}$	663	$\tau_5 = 0.13$	$\beta_{51} = 91.99$
$^4F_{9/2} \rightarrow {}^4I_{13/2}$	1168		$\beta_{52} = 4.32$
$^4F_{9/2} \rightarrow {}^4I_{11/2}$	2019		$\beta_{53} = 3.34$
$^4F_{9/2} \rightarrow {}^4I_{9/2}$	3623		$\beta_{54} = 0.35$

Cross-relaxation and up-conversion coefficients	Value
$C_3\left[\mathrm{m}^3/\mathrm{s}\right]$	$2\cdot10^{-23}$
$C_{up}\left[\mathrm{m}^3/\mathrm{s}\right]$	$3\cdot10^{-23}$
$C_{14}\left[\mathrm{m}^3/\mathrm{s}\right]$	$5\cdot10^{-24}$

Figures 2.4 and 2.5 report the absorption and emission cross sections for erbium-doped $Ga_5Ge_{20}Sb_{10}S_{65}$ glass.

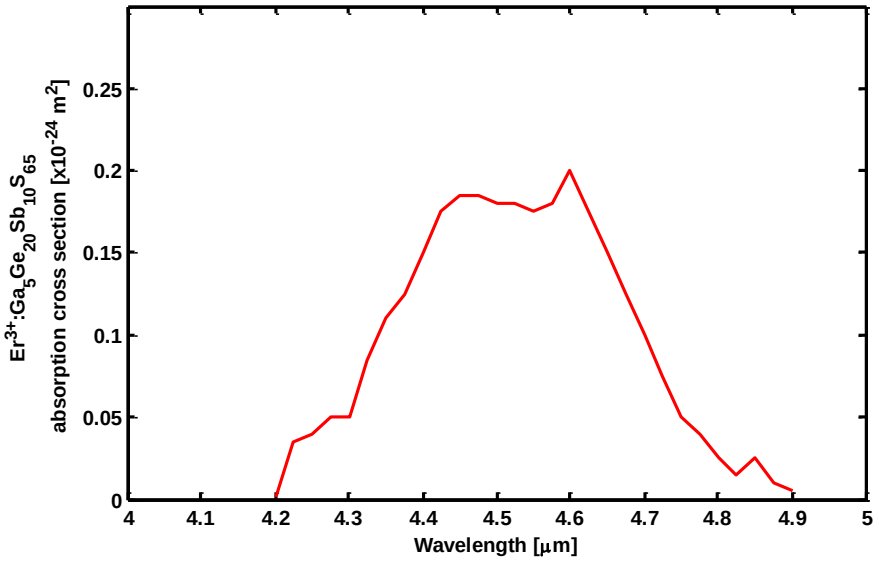

Fig. 2.4 Absorption cross section for Er^{3+}-doped $Ga_5Ge_{20}Sb_{10}S_{65}$ glass.

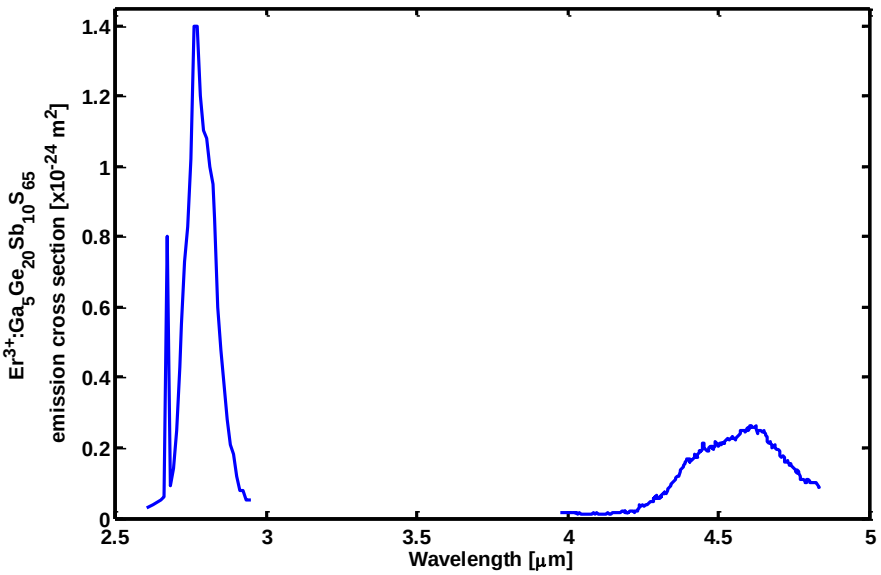

Fig. 2.5 Emission cross section for Er^{3+}-doped $Ga_5Ge_{20}Sb_{10}S_{65}$ glass.

2.5. Praseodymium-doped glass

The four-level model of praseodymium is reported in Figure 2.6. The most important phenomena of rare-earth/light interaction are taken into account in the rate equations 2.13.

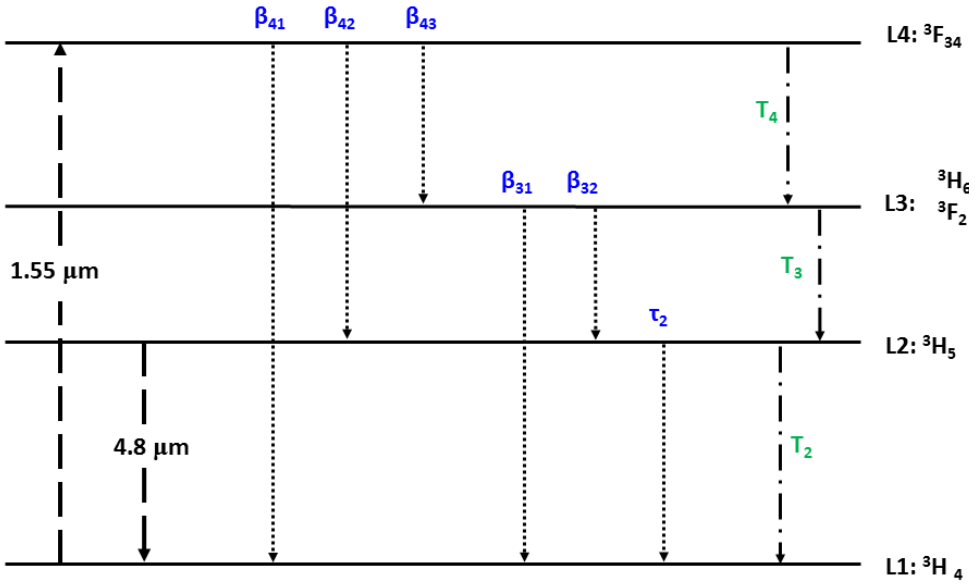

Fig. 2.6 Praseodymium energy level diagram.

$$
\begin{aligned}
&\mathrm{N}_1+\mathrm{N}_2+\mathrm{N}_3+\mathrm{N}_4=N_{tot}\\
&\frac{\mathrm{dN}_4}{dt}=R_{14}\mathrm{N}_1-\mathrm{N}_4\left(\frac{1}{T_4}+A_{43}+A_{42}+A_{41}\right)=0\\
&\frac{\mathrm{dN}_3}{dt}=\mathrm{N}_4\left(\frac{1}{T_4}+A_{43}\right)-\mathrm{N}_3\left(\frac{1}{T_3}+A_{32}+A_{31}\right)=0\\
&\frac{\mathrm{dN}_2}{dt}=W_{12}\mathrm{N}_1+\mathrm{N}_3\left(\frac{1}{T_3}+A_{32}\right)+\mathrm{N}_4A_{42}-\mathrm{N}_2\left(\frac{1}{T_2}+\frac{1}{\tau_2}+W_{21}\right)=0\\
&\frac{\mathrm{dN}_1}{dt}=-\left(R_{14}+W_{12}\right)\mathrm{N}_1+\mathrm{N}_4A_{41}+\mathrm{N}_2A_{31}+\mathrm{N}_2\left(\frac{1}{T_2}+\frac{1}{\tau_2}+W_{21}\right)=0
\end{aligned}
\tag{2.13}
$$

$N_i, i = 1,2,\ldots 4$, is the ion concentration of *i*-th level; τ_i and T_i are the ion lifetimes for pure-radiative and non-radiative transition from level *i*, respectively.

Ion-ion interaction can be neglected using low dopant concentration. Pump emission is negligible.

Non-radiative lifetime takes into account phenomena such as: multi-phonon transition, quenching and cross-relaxation. It can be obtained by ion lifetime and fluorescence lifetime as expressed in equation 2.14:

$$T_i = \tau_{f,i} \frac{\tau_i}{\tau_i - \tau_{f,i}} \tag{2.14}$$

Where τ_i is ion lifetime for pure-radiative transition from level *i* and $\tau_{f,i}$ is fluorescence lifetime.

Table 2.2 reports the spectroscopic parameter measured on praseodymium doped chalcogenide glass $Ga_5Ge_{20}Sb_{10}Se_{65}$ with a Pr3+ concentration of 500 ppm.

Table 2.2 Spectroscopic parameters of the Pr^{3+}-doped chalcogenide glass. Pr^{3+} concentration is 500 ppm.

Energy level transitions	Wavelength [nm]	Branching ratio β [%]	Pure-radiative lifetime τ_i [ms]	Non-radiative lifetime T_i [ms]
$^3H_5 \rightarrow {}^3H_4$	4604	β_{21} = 100.0	τ_2 = 11.36	T_2 = 16.70
$^3H_6 \rightarrow {}^3H_5$	4351	β_{32} = 43.0	τ_3 = 4.66	T_3 = 6.09
$^3H_6 \rightarrow {}^3H_4$	2237	β_{31} = 57.0		
$^3F_{34} \rightarrow {}^3H_6$	5769	β_{43} = 2.0		
$^3F_{34} \rightarrow {}^3H_5$	2481	β_{42} = 18.0	τ_4 = 0.21	T_4 = 1.26
$^3F_{34} \rightarrow {}^3H_4$	1612	β_{41} = 80.0		

Figures 2.7 and 2.8 report the absorption and emission cross sections for praseodymium-doped $Ga_5Ge_{20}Sb_{10}S_{65}$ glass.

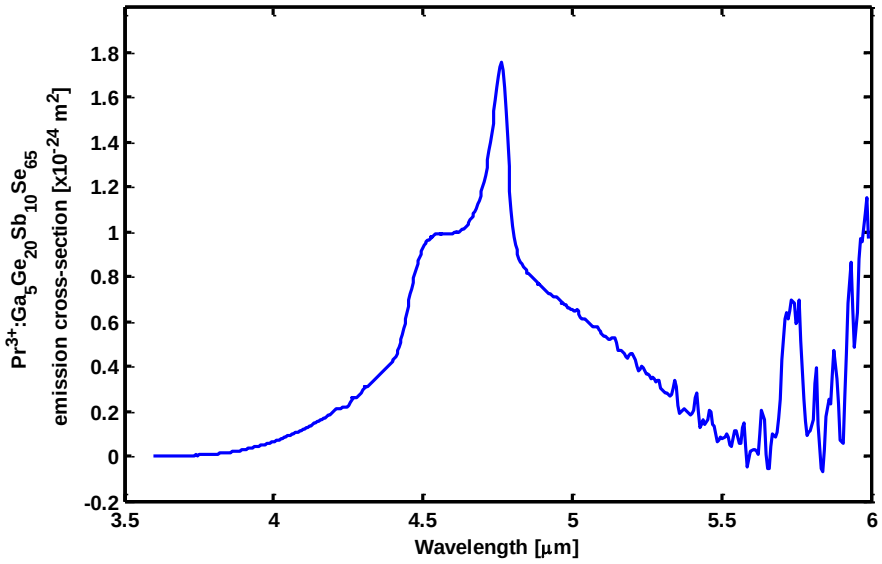

Fig. 2.7 Emission cross section for Pr^{3+}-doped $Ga_5Ge_{20}Sb_{10}Se_{65}$ glass.

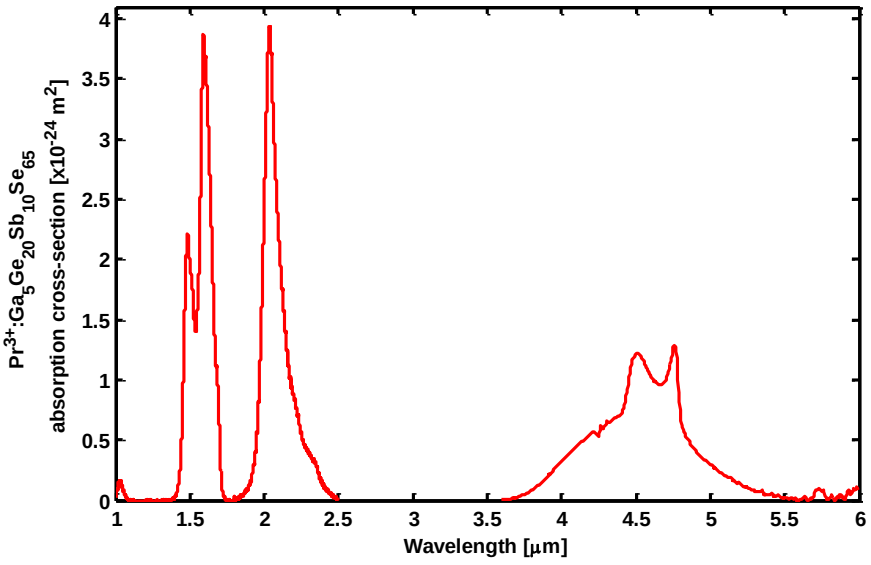

Fig. 2.8 Absorption cross section for Pr^{3+}-doped $Ga_5Ge_{20}Sb_{10}Se_{65}$ glass.

Chapter 3

Design of rare-earth doped microsphere amplifier for bio-sensing[1]

3.1. Introduction

In this chapter an innovative design approach is presented. A Mid-Infrared amplifier constituted by a tapered chalcogenide fiber coupled to an Er^{3+}-doped chalcogenide microsphere is designed via a particle swarm optimization (PSO) algorithm. More precisely the PSO procedure is integrated with a dedicated 3D numerical model based on the coupled mode theory and solving the rate equations. The rate equations include the main transitions among the erbium energy levels, the amplified spontaneous emission and the most important secondary transitions pertaining to the ion–ion interactions. The PSO allows the optimal choice of the structure parameters: microsphere and fiber radius, fiber angle taper, fiber microsphere gap in order to maximize the amplifier gain. The geometrical parameters can be optimized to efficiently inject into the microsphere both the pump and the signal beams and to improve their spatial overlapping with the rare-earth doped region. The employment of PSO technique shows different attractive features especially when many

[1] Work presented in this chapter has appeared in [29]: G. Palma, P. Bia, L. Mescia, T. Yano, V. Nazabal, J. Taguchi, A. Moréac, and F. Prudenzano "Design of fiber coupled Er3+: chalcogenide microsphere amplifier via particle swarm optimization algorithm," *Optical Engineering*, vol. 53, no. 7, pp. 071805-071805-8, 2013.

parameters have to be optimized. The numerical results demonstrate that the PSO-based optimization procedure allows the design of a microsphere amplifying system more efficient than similar devices designed by using a deterministic optimization method.

3.2. Particle Swarm Optimization (PSO) algorithm

Deterministic optimization methods are typically used in order to design and optimize rare-earth doped glass amplifiers. The optimal amplifier geometrical parameters, the rare earth concentration, the waveguide transversal section and all the other design parameters are identified one at time. The up-conversion and cross relaxation phenomena induce nonlinearities in rare-earth doped glass amplifier model. As result, the optimization problem in rare-earth doped microsphere amplifier is difficult to be performed especially because of the number of geometrical parameters have to be finely optimized. Moreover, deterministic algorithms can exhibit stagnation problems in local maxima/minima during the search of the objective functions (e.g. gain, bandwidth, output power, signal to noise ratio). The stochastic nature of the PSO algorithm allows a high efficiency in optimization of a large number of parameters for its ability to avoid local maxima/minima and operate in discontinues solution domains.

The particle swarm optimization (PSO) algorithm is a global search numerical method, inspired by the social behavior exhibited by a variety of animals during their search for food, e.g. bees, fishes, birds [32-36]. In PSO algorithm, a population of N_b tentative solutions or particles corresponds to the swarm of bees. They fly to search food, i.e high density

of flowers. Each particle is characterized by a position constituting a trial/tentative solution. For a D-dimensional search space, this tentative solution is identified by a D-dimensional vector $\boldsymbol{p}_j$, i.e. a set of tentative values of the independent variables. The tentative solution goodness is evaluated by means of a suitable fitness function *F* [21-22]. The tentative solutions are updated in the multidimensional solution space with the aim of optimizing the fitness function (to maximize/minimize).

The bee positions (solutions) are updated by applying the operator $\mathbf{v}_j$, called velocity, which is dynamically adjusted according to the historical behaviours of the particle in order to maximize/minimize the fitness function *F*. At first, each bee (particle) has a random position and a random velocity then its trajectory is modified by keeping track of its location in the solution space and by taking into account both the previous locations giving the best fitness value experimented by the single particle (personal best position, $\boldsymbol{p}^{PB}$) and highest fitness location discovered by the entire swarm (global best position, $\boldsymbol{p}^{GB}$). Therefore the movement of each particle depends on three factors:

i) the cognitive factor, related to the personal best position $\boldsymbol{p}^{PB}$;

ii) the social factor, related to the global best position $\boldsymbol{p}^{GB}$;

iii) the inertial factor, i.e. a suitable resistance to the change of the particle direction.

Each of these factors is weighted by an ad hoc parameter: the cognitive parameter c_1, the social parameter c_2, the inertia weight I_w. Each particle trajectory is updated till a convergence criterion is reached. In this

way, the entire swarm moves towards positions characterized by maximized/minimized values of the fitness function. A flow chart of the PSO algorithm is illustrated in Figure 3.1.

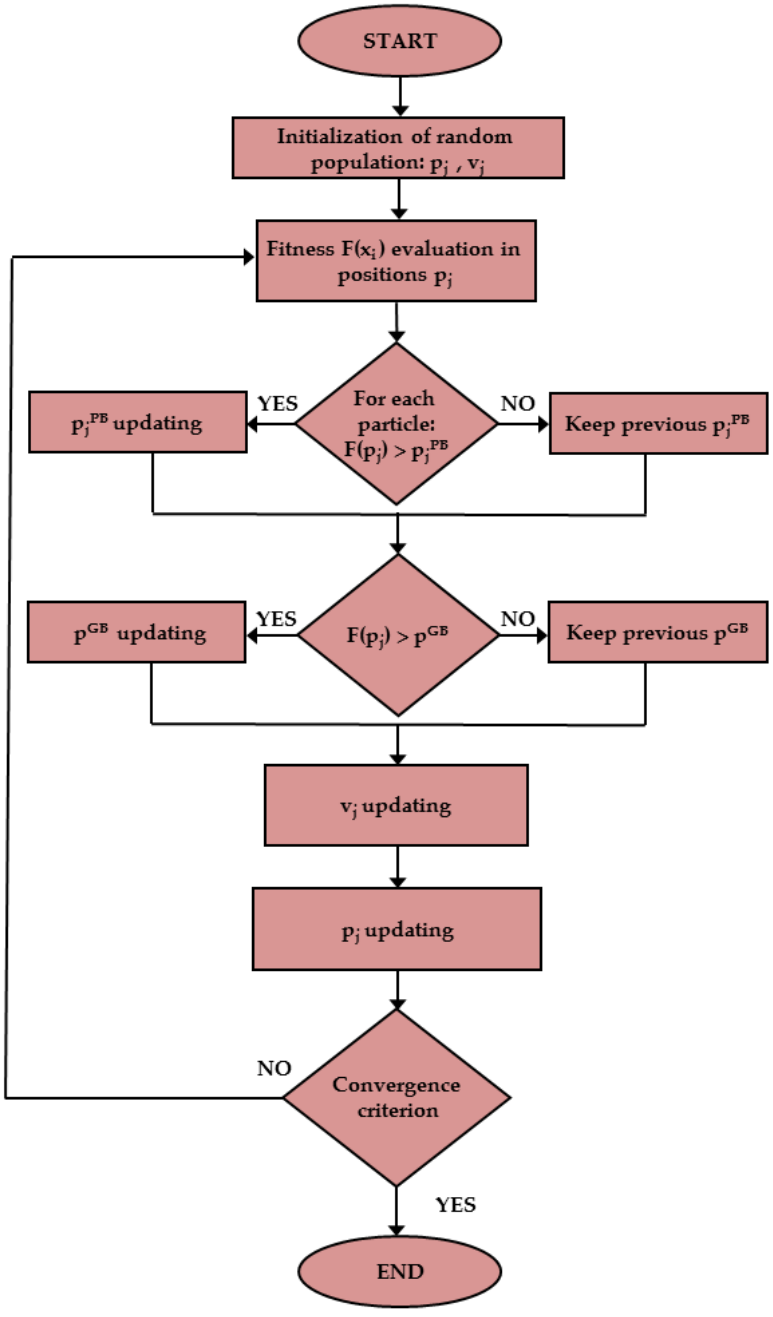

Fig. 3.1 Flow chart of the PSO algorithm.

More precisely, the position $\boldsymbol{p}_j$ and the velocity $\mathbf{v}_j$ vectors of the particles are updated at the n+1 iteration by means of the following set of equations [30-31]:

$$\begin{aligned} \mathbf{v}_j(n+1) &= I_w \times \mathbf{v}_j(n) + c_1 \times r_1 \times \left[\boldsymbol{p}_j^{PB}(n) - \boldsymbol{p}_j(n)\right] + c_2 \times r_2 \times \left[\mathbf{p}^{GB}(n) - \mathbf{p}_j(n)\right] \\ \boldsymbol{p}_j(n+1) &= \boldsymbol{p}_j(n) + \boldsymbol{v}_j(n+1) \end{aligned} \qquad (3.1)$$

$$\text{with } j = 1,2,\ldots,N_b .$$

$\boldsymbol{p}_j^{PB}(n)$ is the previous local best position of the *i-th* particle, $\mathbf{p}^{GB}(n)$ is the previous global best position among all the particles in the population, c_1 and c_2 are the cognitive and social parameter, respectively, r_1 and r_2 are positive numbers randomly generated between 0 and 1 to inject a stochastic behavior in the searching procedure. I_w is the inertia weight.

In this work, the cognitive parameter is c_1 = 1.494, the social parameter is c_2 = 1.494 [101]. The converge criterion used in this thesis is the achievement of a fixed number of PSO iterations I_{PSO}. I_w is a vector with I_{PSO} elements linearly spaced from 0.4 to 0.9.

3.3. Rare-earth doped chalcogenide microspheres

Optical micro-resonators are key elements in modern photonics for fabrication of a great variety of devices applied in both linear and nonlinear optics. Generally, the mode resonance is obtained by utilizing two or more mirrors or gratings. Multiple recirculation of light in optical micro-resonators enables laser oscillation and increases the effective path length, providing a great potential in spectroscopic and interferometric measurements. However, conventional Fabry–Perot (FP) resonators can exhibit some drawbacks such as high cost, low compactness, and mechanical instability [37].

An alternative to the linear micro-resonators is constituted by dielectric spherical micro-resonators, such as dielectric microspheres. These devices allow light confinement in circular orbits by means of repeated total internal reflections occurring at the spherical boundary between the dielectric surface and the surrounding medium. Their surprising properties are related to the resonance of the well-known whispering-gallery-modes (WGMs), exhibiting high quality factors Q ($10^5 \div 10^9$) and small mode volumes, as described in chapter 1. Whispering gallery modes can be excited in different ways. In fused silica, microspheres have been excited using evanescent field provided by a prism [38], polished optical fiber coupler [39-40] and tapered optical fiber [41].

WGM resonances in dielectric microspheres have been investigated and experimented for many applications, e.g. the polarization transmission, biosensing, nonlinear optics, coupled-resonator-induced

transparency, quantum electrodynamics (QED), quantum information processing [42-44]. Moreover, they enable novel functionalities for planar light-wave circuits, such as wavelength selectivity, resonant filtering [45], energy storage and dispersion control.

Micro-cavity amplifiers or lasers can be obtained by doping microspheres with rare-earth ions. Rare-earth doped microspheres based on silica, phosphate, tellurite and ZBLAN glass host materials have been fabricated, obtaining low threshold lasing and very narrow emission linewidth [44][46-49]. As example, WGMs were excited in Nd^{3+}-doped fluoride glass microsphere by using a Ti:Al_2O_3 laser tuned to 800 nm [50]. The laser pump thresholds were found to be 5 and 60 mW for the 1051 nm and 1334 nm wavelength emissions, respectively.

Important improvements can be achieved using chalcogenide glasses. These glasses exhibit peculiar optical properties such as high refractive index, extremely high nonlinearity, photosensitivity, low phonon energy. WGMs in chalcogenide microspheres have exceptionally low modal volume. In addition, due to the high refractive index, high absorption and emission cross sections are measured in this kind of glasses [51]. However, the low phonon energy induces large radiative decay rates, high quantum efficiency and allows radiative transitions that are quenched by the multiphonon decay in silica glasses. Moreover, the high rare-earth solubility facilitates the fabrication of efficient lasers and amplifiers.

The feasibility of chalcogenide microsphere has been demonstrated in a variety of works [51-54]. As example, in [52] the fabrication of chalcogenide microspheres heated by contact with a temperature

controlled ceramic surface has been demonstrated; WGM resonances, excited by using tapered silica glass fiber have been observed and a Q factor greater than 10^5 was measured close to the wavelength λ=1.55 μm. In [45] packaged chalcogenide As_2S_3 microspheres, using a low refractive index UV-curable polymer have been fabricated; high-Q modes have been excited at wavelengths close to 1.55 μm, in a 110 μm diameter chalcogenide microsphere via evanescent coupling from a 2 μm diameter tapered silica fiber.

The need to suitably package chalcogenide microsphere coupled to tapered silica fiber on feasible planar geometry, has led to fabricate preliminary microsphere prototypes of chalcogenide glass with the composition of $Ga_5Ge_{20}Sb_{10}S_{65}$ doped with erbium. Partly truncated spheres, called "supersphere", working as a whispering gallery mode (WGM) resonator around its equatorial plane, have been lately fabricated via "surface-tension mold (StM) technique" [55].

During the past decades, a large literature has reported experiments on rare-earth doped microspheres but only few papers have addressed simulation models for lasing in microspheres [56-57]. In these conventional numerical procedures, the solution of both the rate and power propagation equations is performed by optimizing, one by one, each design parameter. However, the nonlinearity of the equations makes algorithms based on these approaches computationally expensive. Global and stochastic optimization methods, such as particle swarm optimization (PSO), are efficient tools to investigate this kind of problems. As example, PSO have been employed for the optimization and characterization of rare-earth doped photonic crystal fiber amplifiers [32-33].

3.4. Synthesis of chalcogenide microspheres

Surface-tension Mold (StM) technique has been used to the fabrication of the aforesaid erbium doped chalcogenide glass microsphere giving good experimental results [55]. The bulk glass sample was prepared by conventional melting and quenching method in a silica glass ampoule [28]. The fabricated glass was crashed into powder of less than 200 μm. The crashed glass powders were classified using sieves in the range of 20-40 μm and 40-80 μm, washed by iso-propanol under ultrasonic wave and finally, dried in air for a day. These powders were put on a polished glassy carbon substrate and heated at 515°C for 5 min on the electric furnace settled in glove box filled with dry argon gas or in furnace with a flux of argon and H_2S gas. Figure 3.2 a) and b) report a SEM image and an optical microscope image of a chalcogenide microsphere by StM technique, respectively. It is apparent that the microsphere has a superspherical shape. Indeed the contact angle of 2S2G glass is α_c>90 deg, as a glassy carbon is a favorable substrate to induce low wettability of the molten chalcogenide glass. High Q factor can be realized in a truly spherical particle made of the extremely transparent material without scattering inclusion and contaminant on and/or inside the sphere. Therefore, during the preparation of super-spherical optical resonator of $Ga_5Ge_{20}Sb_{10}S_{65}$ glass by StM technique, it needs to pay attention to the factors of shape (curvature of sphere) and the surface scattering. The percentage of the prepared super-spheres with high sphericity and/or circularity at the equatorial plane was about 10% and their deviation to circularity was less than 3% (see Figure 3.3). These values are good enough to use them for optical resonator.

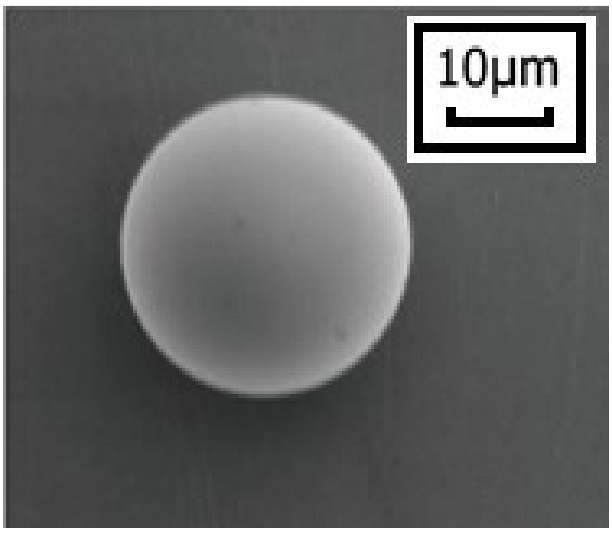

Fig. 3.2a SEM image of Er^{3+}:$Ga_5Ge_{20}Sb_{10}S_{65}$ micrometer microsphere coated with Au/Pd conductive layer at the surface for SEM imaging.

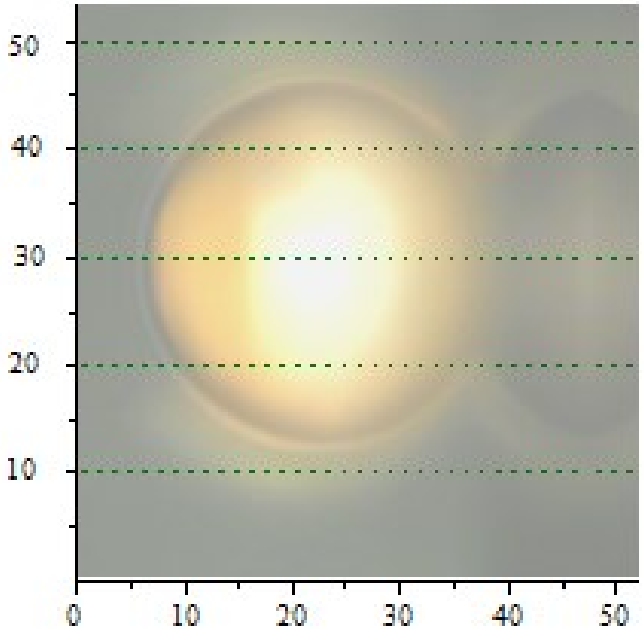

Fig. 3.2b Optical microscope images of Er^{3+}:$Ga_5Ge_{20}Sb_{10}S_{65}$ micrometer microsphere coated with Au/Pd conductive layer at the surface for SEM imaging.

The transition temperature of $Ga_5Ge_{20}Sb_{10}S_{65}$ glass is sensitive to the atomic ratio of sulfur to the metals. Lower sulfur content increases the glass transition temperature and could decrease the thermal stability of glass against crystallization. The precipitation of crystal is energetically easy on the heterogeneous interface like glass surface. A Raman spectroscopy on the sulphide glass super-sphere confirms this hypothesis. Once α-GeS_2 crystallites appear on the surface of the molten glass droplet, it corrupts the balance of the surface tension in the particle and gives distorted super-sphere. In order to make good spherical surface and improve its Q factor, the surface crystallization have to be suppressed well. Therefore, the strict control of sulfur content of the $Ga_5Ge_{20}Sb_{10}S_{65}$ glass is requisite for the preparation of optical resonator made of glass by StM technique.

The results were significantly improved when a mixture of H_2S/Ar gas has been employed during the StM heat treatment and it is an essential way for reducing the crystal surface formation. Thanks to the optimized StM process enabling super-spherical microsphere fabrication in the diameter range of 5-50 μm, whispering gallery modes were observed for these microspheres concerning their luminescence around 650 nm using the Raman spectrophotometer (figure 3.3). Furthermore, a luminescence centered at about 2775 nm corresponding to the $^4I_{11/2} \rightarrow {}^4I_{13/2}$ transition was also experimentally observed from Er^{3+}:$Ga_5Ge_{20}Sb_{10}S_{65}$ glass pumped at 980nm (figure 3.4).

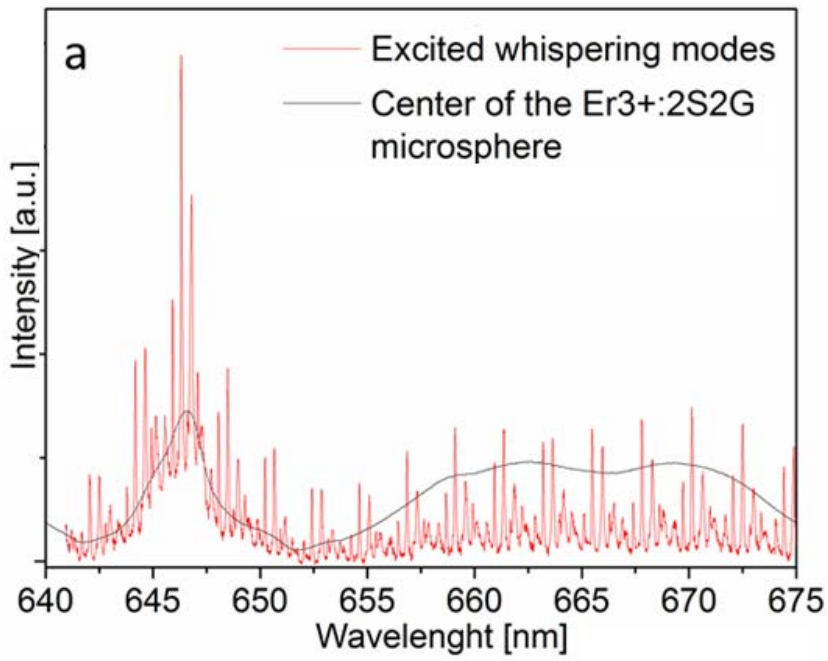

Fig. 3.3 Raman and fluorescense spectra for 633nm excitation in the centre and border of an equatorial plane of the Er^{3+}:$Ga_5Ge_{20}Sb_{10}S_{65}$ microsphere.

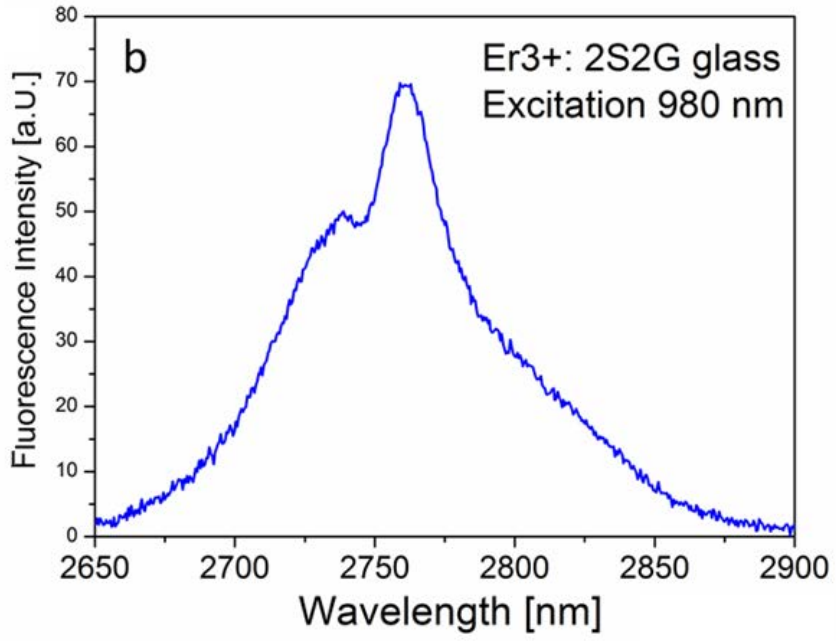

Fig. 3.4 Fluorescence spectrum of Er^{3+}:$Ga_5Ge_{20}Sb_{10}S_{65}$ glass excited at 980nm.

3.5. Design of Er^{3+}:$Ga_5Ge_{20}Sb_{10}S_{65}$ microsphere amplifier

An amplifying system operating close to 2.7 μm and based on Er^{3+}-doped chalcogenide microsphere coupled to a tapered fiber is optimized via a PSO approach. In the amplifying system, the tapered optical fiber is placed close to the equator of the Er^{3+}-doped chalcogenide microsphere. The taper fiber is used to excite the microsphere at both the signal and pump wavelengths. Figure 3.5 illustrates a sketch of the amplifying system.

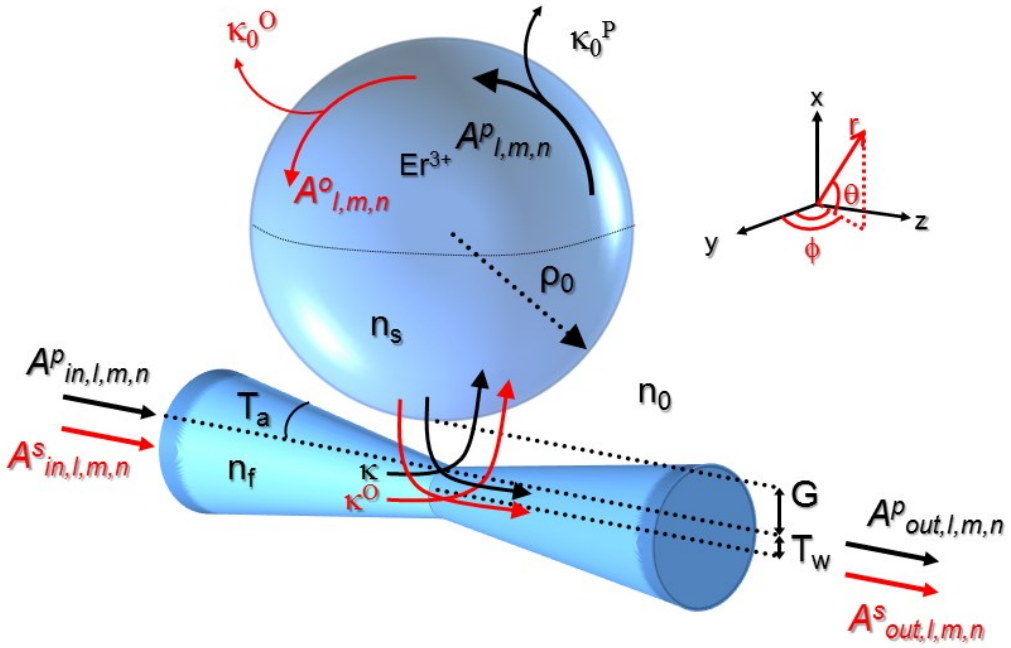

Fig. 3.5 Layout sketch of the chalcogenide fiber taper coupled to the Er^{3+}doped chalcogenide microsphere. The taper fiber is used to excite the microsphere at both signal and pump wavelengths.

The accurate 3D mathematical model for Er^{3+}-doped chalcogenide microspheres described in the chapters 1 and 2 is employed for calculating the fitness function of the PSO procedure. The core of the developed numerical code is based on the coupled mode theory and the rate equations model. In particular, it includes the modal distribution of the optical waves in both tapered fiber and microsphere, and takes into account the most relevant active phenomena in Er^{3+}-doped chalcogenide glasses such as the radiative and non-radiative rates, at both pump and signal wavelengths, the stimulated emission of the signal, the amplified spontaneous emission noise (ASE), the lifetime and branching ratios of the considered energy levels, the ion-ion energy transfers and the excited state absorption (ESA). The design is realistically performed, on the basis of the optical and spectroscopic parameters measured on chalcogenide glass [12-13, 27] and by considering the coupling of the microsphere with the tapered fiber.

In the PSO modeling the pump wavelength is close to λ_p=980 nm and the signal wavelength is close to λ_s=2700 nm. The size of the fiber taper has to be designed to ensure the fundamental mode propagation and a suitable evanescent field in fiber-microsphere gap. In order to carry out a realistic optimization and therefore an actual evaluation of the device feasibility, the simulations have been performed by taking into account the refractive index wavelength dispersion by means of the Cauchy equation [27] and the measured spectroscopic parameter summarized in Table 2.2 and for convenience reported in Table 3.1.

Table 3.1 Spectroscopic parameters of the Er^{3+}-doped chalcogenide glass [12-13, 27-28].

Cauchy Equation		$n(\lambda) = 2.2181 + \frac{0.0551}{\lambda^2} - \frac{0.0003}{\lambda^4}$	
Energy level transitions	Wavelength [nm]	Lifetime [ms]	Branching ratio [%]
$^4I_{13/2} \rightarrow {}^4I_{15/2}$	1532	$\tau_2 = 1.83$	$\beta_{21} = 100.0$
$^4I_{11/2} \rightarrow {}^4I_{15/2}$	986	$\tau_3 = 1.37$	$\beta_{31} = 86.28$
$^4I_{11/2} \rightarrow {}^4I_{13/2}$	2771	$\tau_3 = 1.37$	$\beta_{32} = 13.72$
$^4I_{9/2} \rightarrow {}^4I_{15/2}$	810	$\tau_4 = 1.08$	$\beta_{41} = 80.38$
$^4I_{9/2} \rightarrow {}^4I_{13/2}$	1719	$\tau_4 = 1.08$	$\beta_{42} = 18.82$
$^4I_{9/2} \rightarrow {}^4I_{11/2}$	4529	$\tau_4 = 1.08$	$\beta_{43} = 0.80$
$^4F_{9/2} \rightarrow {}^4I_{15/2}$	663	$\tau_5 = 0.13$	$\beta_{51} = 91.99$
$^4F_{9/2} \rightarrow {}^4I_{13/2}$	1168	$\tau_5 = 0.13$	$\beta_{52} = 4.32$
$^4F_{9/2} \rightarrow {}^4I_{11/2}$	2019	$\tau_5 = 0.13$	$\beta_{53} = 3.34$
$^4F_{9/2} \rightarrow {}^4I_{9/2}$	3623	$\tau_5 = 0.13$	$\beta_{54} = 0.35$
Cross-relaxation and up-conversion coefficients		Value	
$C_3\left[\mathrm{m}^3/\mathrm{s}\right]$		$2 \cdot 10^{-23}$	
$C_{up}\left[\mathrm{m}^3/\mathrm{s}\right]$		$3 \cdot 10^{-23}$	
$C_{14}\left[\mathrm{m}^3/\mathrm{s}\right]$		$5 \cdot 10^{-24}$	

The absorption and emission cross sections affect the competition among a number of different resonant WGMs. Figures 2.4 and 2.5 (see chapter 2) illustrate the absorption and emission cross sections for erbium-doped $Ga_5Ge_{20}Sb_{10}S_{65}$ glass. As example, the absorption cross section at the pump wavelength λ=986 nm is close to 1.32×10^{-24} m^2 while the emission cross section at the signal wavelength is λ= 2770 nm is close to 1.4×10^{-24} m^2. Different emission and absorption cross section values are considered for the different WGM resonance frequencies.

The thickness of the erbium-doped region (near the microsphere surface) and the erbium concentration are h_{Er} = 3 μm and C_{Er} = 0.5 w%, respectively. The input pump power is P_p = 100 mW and the input signal power P_s = −50 dBm.

The approach based on swarm intelligence is employed in the design in order to obtain values of geometrical parameters maximizing the optical gain g. In particular, the PSO is applied to optimize microsphere radius ρ_0, taper waist radius T_W, taper angle T_a, taper-microsphere gap G. Therefore, the algorithm described in section 3.2 is written by defining a swarm composed by N_b = 32 particles. The position vector of the j-th particle is $\boldsymbol{p}_j = \left[\rho_o^j, T_W^j, T_a^j, G^j\right]$ with $j = 1,2,\ldots,N_b$. The fitness function is:

$$F(\boldsymbol{p}_j) = 10\log g(\boldsymbol{p}_j) \tag{3.2}$$

$g(\boldsymbol{p}_j)$ is the gain of the amplifier for particle $\boldsymbol{p}_j$ as defined in equation 2.7, chapter 2.

The PSO parameters are tuned heuristically by evaluating the solution space characteristic. On the basis of previous working experiences, the limits of the considered variables are roughly fixed such that the maximum gain is expected to lie in suitable ranges. Furthermore, the limits are fixed by considering these technological needs:

i) a suitable microsphere radius ρ_0 in order to have resonance at both the pump and signal wavelengths;
ii) the waist radius larger than the inferior limit T_W = 0.5μm, since chalcogenide glass exhibits a number of drawbacks in the construction of taper having smaller waist;
iii) the waist radius smaller than the superior limit T_W = 0.8 μm in order to have single-mode propagation;
iv) feasible taper angle T_a and feasible taper–microsphere gap G.

The parameters used in PSO algorithm and the solution space limits are summarized in Table 3.2.

Table 3.2 Parameters and solution space limits used in PSO algorithm.

Variable	Value
Social parameter c_1	1.494
Cognitive parameter c_2	1.494
Inertia weight I_w	linearly spaced vector from 0.9 to 0.4
Iteration limit I_{PSO}	32
Number of particles N_b	32
Domain ranges for ρ_0 [μm]	10 ÷ 50
Domain ranges for T_W [nm]	500 ÷ 800
Domain ranges for T_a [rad]	0.001 ÷ 0.04
Domain ranges for G [nm]	500 ÷ 1000

The PSO simulations have been performed by considering many WGMs in the wavelength band from 2740 nm to 2820 nm. By varying the parameter n from 1 to 3, 18 different resonant WGMs were simulated. The parameters l,m,n, the WGM resonance wavelengths, the output powers and the optical gains are reported in Table 3.3.

The PSO has allowed the identification of the maximum gain g (global best) for the $WGM_{217,217,1.}$ The optimal parameters obtained with PSO approach are:

- microsphere radius ρ_0 = 45 μm;
- taper waist radius T_W = 517 nm;
- taper angle T_a =0.03 rad;
- taper-microsphere gap G = 512 nm.

By simulations, slight variations (tens of nanometres) of taper waist radius and taper-microsphere gap induce low gain changes (about 1dB).

Table 3.3 PSO optimized amplifier. Parameters $l = m$ and n of WGMs, resonance wavelength, output power and optical gain.

l=m values	n values	WGM resonance wavelength [nm]	P_{out} [dBm]	Optical gain g [dB]
213	1	2813	-37.3	12.7
214	1	2802	-35.1	14.9
215	1	2788	-33.6	16.4
216	1	2777	-27.1	22.9
217	1	2763	-16.3	33.7
218	1	2751	-33.5	16.5
205	2	2808	-46.8	3.2
206	2	2796	-46.5	3.5
207	2	2783	-46.1	3.9
208	2	2770	-45.2	4.8
209	2	2758	-45.4	4.6
210	2	2746	-46.7	3.3
198	3	2810	-49.0	0.9
199	3	2797	-48.9	1.1
200	3	2784	-48.9	1.1
201	3	2772	-48.7	1.3
202	3	2759	-48.7	1.3
203	3	2747	-48.9	1.0

In the simulation, for each WGM the proper resonant frequency is taken into account in order to evaluate all the spectroscopic and physical parameters, such as refractive index, emission cross section and absorption cross section, affecting the competition with the other WGMs. The modes with n=1,2,3 and m=l have been considered in the simulation. WGMs with different values of l and m, have not been considered because exhibited low overlapping factor Ω^{y}_{WGM}, with y = P,S (see equation 2.3 in chapter 2).

Table 3.4 reports the characteristics of the PSO optimized amplifier. In particular, a high intrinsic signal lifetime τ_0 is calculated resulting in low losses.

Table 3.5 reports the comparison among the parameter values calculated by the proposed PSO algorithm and those obtained with the deterministic algorithm DA in [12].

Table 3.4 Characteristics of the PSO optimized amplifier

Variable	Value
Signal WGMs mode	n=1, l=m=217
Signal wavelength λ_s (nm)	2763
Signal refractive index of microsphere n_s and taper n_f	2.2253
Pump WGMs mode	n=1, l=m=641
Pump wavelength λ_p (nm)	979.9
Intrinsic signal lifetime τ_0 (μs)	0.1357
Coupling signal lifetime τ_{ext} (ns)	0.2248
Optical gain g (dB)	33.7

Table 3.5 Comparison between DA and PSO: gain g, microsphere radius ρ_0, taper waist radius W_T, taper angle T_a and taper-microsphere gap G.

Variable	DA value	PSO value
DA maximum gain/ Fitness Global best [dB]	6.9	33.7
Microsphere radius ρ_0 [μm]	25	45
Taper waist radius T_W [nm]	700	517
Taper angle T_a [rad]	0.03	0.02
Taper-microsphere gap G [nm]	560	512

Figure 3.6 illustrates the distribution of the normalized field $|E_\theta|$ in case of the maximum gain $WGM_{217,217,1}$ and coupled taper fiber mode on the longitudinal plane. The electric field is power normalized as described in chapter 1. In the picture it is apparent that the radial mode of $WGM_{217,217,1}$ is $n = 1$, in fact there is only one maximum in radial direction. For the sake of clarity, the azimuthal dependence expressed via a complex exponential function: $\exp(-im\phi)$ is not showed because of the high value of parameter $m = 217$.

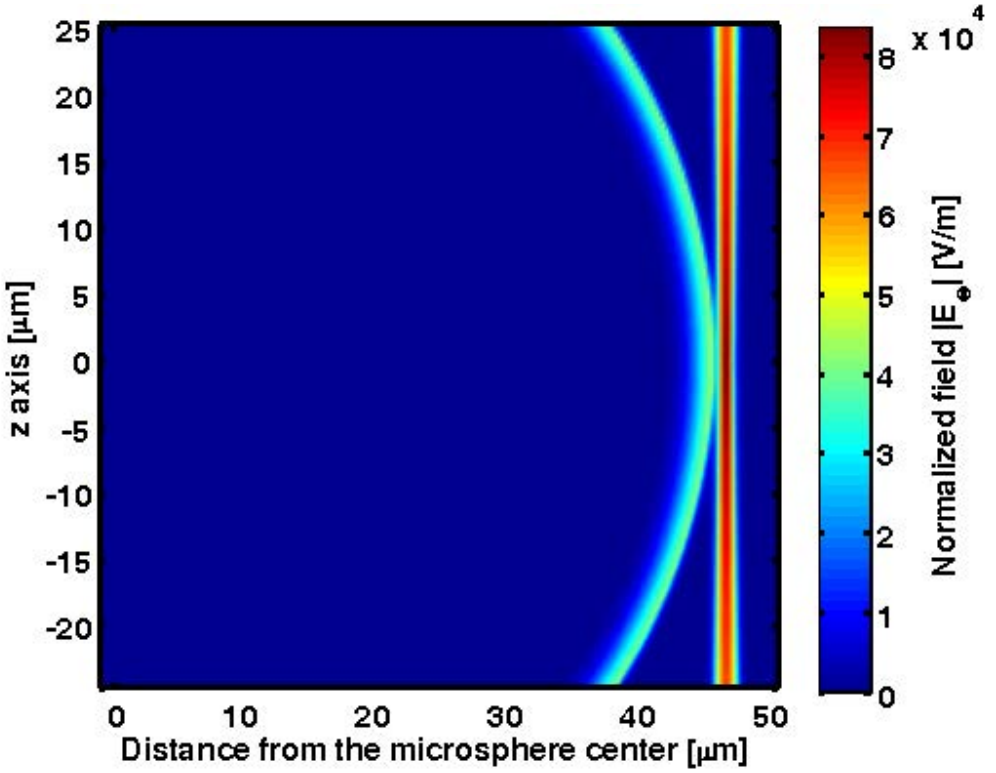

Fig. 3.6 Distribution of the normalized field $|E_\theta|$ of $WGM_{217,217,1}$ and coupled taper fiber mode on the longitudinal plane. The structure is the PSO optimized: microsphere radius ρ_0 = 45 µm, taper waist radius T_W = 517 nm, taper angle T_a =0.03 rad, taper-microsphere gap G = 512 nm.

The results reported in Tables 3.3-3.5 show that the proposed PSO approach finds solutions more efficiently than the deterministic one [12]. Indeed the use of a deterministic method requires a suitable discretization for ρ_o, T_W, T_a, G and thus the investigation of an extremely high number of different cases with very large time consumption. The discrepancy in the calculated maximum gain observed between the deterministic (DA), g = 6.9 dB, and the particle swam optimization algorithm (PSO), g = 33.7 dB, is due to the higher efficiency of global optimization procedure allowing a better design to parity of calculation time consumption. In fact, PSO optimizes simultaneously a high number of parameters through an automated global solution search. On the contrary, in DA, to avoid extremely large time consumption, a parameters at time is varied, by fixing all the others that are supposed optimized (local search). A global search could be performed with a DA but a very high number of simulation cases are required. The DA simulation number is related to the calculation accuracy (parameter quantization/discretization) and to the number of parameters to be optimized. When the designer chooses the most promising DA simulation cases some particular configurations can be neglected, therefore losing the best configuration. Therefore, in this case, PSO has allowed the identification of a specific amplifier configuration not included in the deterministic investigation illustrated in [12].

The performance of the PSO approach can be easily understood by the example of Figure 3.7. It illustrates all the particles elaborated by a PSO execution in: a) microsphere radius ρ_o and taper waist radius T_w research space; and b) taper angle T_a and taper-microsphere gap G research space. As reported in Table 3.2, the iteration limit I_{PSO} = 32 and the number of particles N_b = 32, so the total number of computed particles is $32 \times 32 = 1024$. The colour represents the optical gain g corresponding to each particle. It is worthwhile to note that many particles are located in a small region around the maximum gain value (global best).

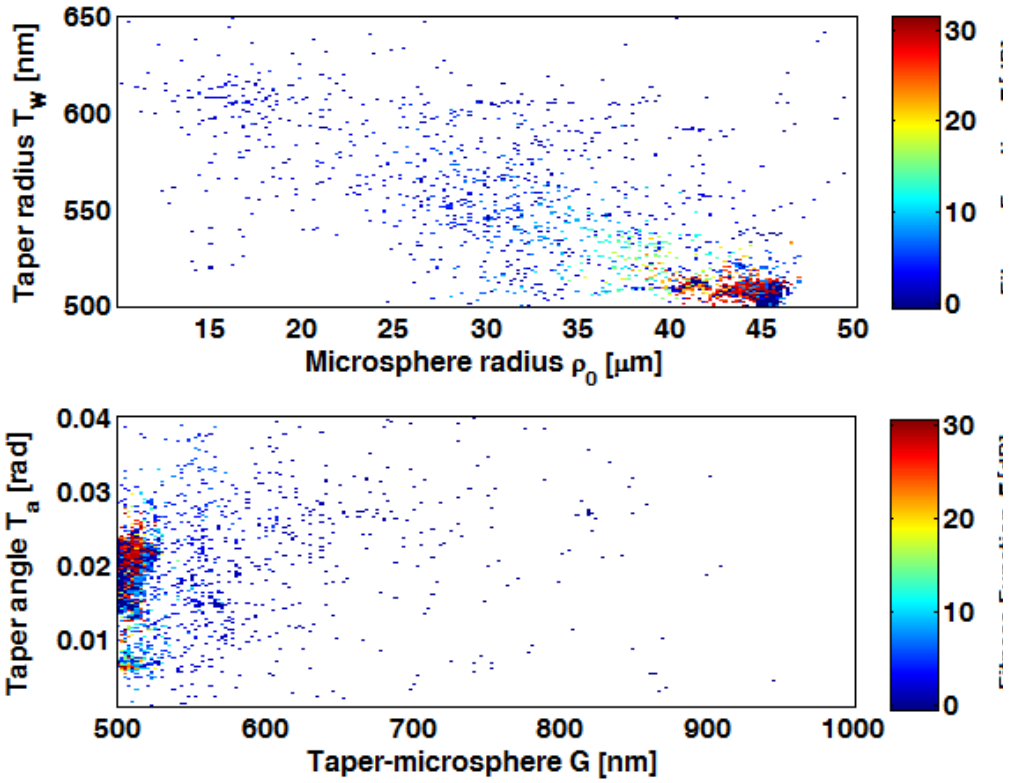

Fig. 3.7 PSO optimized solutions: a) microsphere radius *Ro* and fiber taper radius *a*; b) gap *G* and taper angle δ

A high number of PSO runs have been performed. In almost all cases, about 18 iterations have been required for convergence, obtaining a global best close to 33.7 dB. Figure 3.8, illustrates the fitness function $F(\boldsymbol{p}_j)$corresponding to the global best (i.e. gain g in dB, calculated for the global best position $\boldsymbol{p}^{GB}$ of the swarm) versus iteration number during a single PSO run. A gain very close to the maximum one is reached after only 18 iterations. This confirms that the algorithm enables to find solutions quickly.

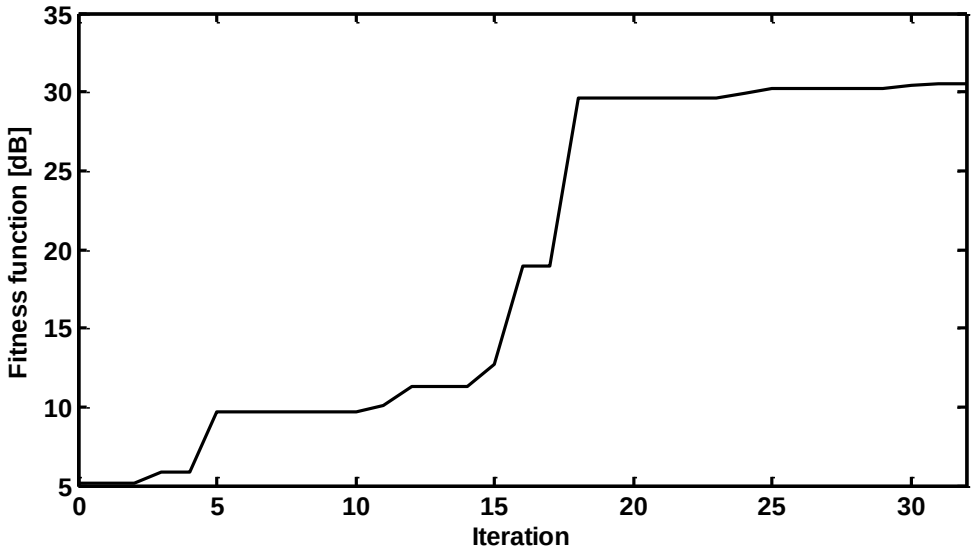

Fig. 3.8 Fitness function corresponding to global best position $\boldsymbol{p}^{GB}$ versus iterations.

3.6. Summary

In conclusion an accurate design of Er^{3+}-doped chalcogenide microsphere amplifier evanescently coupled with a tapered optical fiber has been performed. The amplifying system has been optimized via a PSO procedure for operation close to 2700 nm. The PSO has provided surprising performance in terms of convergence and efficiency, allowing a global optimization of the microsphere amplifier. As results, an improvement of the simulated gain of the microsphere amplifier from g = 6.9 dB, found with the deterministic approach (DA) [12] for a very similar device, to g = 33.7 dB, found with PSO, has been obtained. The numerical results underline that, due to the high number of the design parameters to be optimized, a deterministic solution searching strategy does not allow an efficient design in this kind of problems. The PSO approach has given good results allowing a global optimization of the microsphere amplifier by varying simultaneously a number of design parameters.

The simulation results indicate that the proposed Er^{3+}-doped chalcogenide microsphere amplifier, evanescently coupled with a tapered optical fiber, seems very promising and could find interesting applications. Although good $Ga_5Ge_{20}Sb_{10}S_{65}$ have been fabricated and characterized, the amplifier construction is related to the not trivial problem of drawing suitable $Ga_5Ge_{20}Sb_{10}S_{65}$ fiber taper with very small radius. Therefore, further technological efforts will be dedicated in future to this aim. For instance, an integrated optical system can be used to overcome the fragility of fiber taper for such dimension [58].

Chapter 4

Modeling of microspheres for spectroscopic characterization[2]

4.1. Introduction

In the previous chapter, a global solution search procedure based on particle swarm optimization (PSO) approach has been integrated with a refined model of a Mid-Infrared amplifier constituted by a tapered chalcogenide fiber coupled to an erbium doped chalcogenide microsphere. The aim was to optimize the amplifier maximizing the optical gain. In this chapter, the same model is conveniently integrated with the PSO approach in order to obtain an algorithm useful to evaluate the spectroscopic parameters of rare-earth doped glass microspheres. This method allows the recovering of the rare-earth parameters by means of the optical gain measurement and could substitute the high-cost instrumentations used for spectroscopic measurements. The error in evaluation of the erbium lifetime τ_{41} is lower than 3.5 %. It is lower than 0.5 % for the other lifetimes and ion-ion interaction parameters. These excellent results are obtained since WGM electromagnetic field interacts with rare-earth for long effective distances.

[2] Work presented in this chapter has appeared in [59]: G. Palma, C. Falconi, V. Nazabal, T. Yano, T. Kishi, T. Kumagai, M. Ferrari, and F. Prudenzano, "Modeling of Whispering Gallery Modes for Rare Earth Spectroscopic Characterization," *IEEE Photonics Technology Letters*, vol. 27, no. 17, 1861–1863, 2015.

4.2. Microsphere for characterization using PSO

Over the last few decades, microsphere resonators have attracted large interest as promising elements for the construction of a variety of active and passive photonic devices. The resonant modes, i.e. the whispering gallery modes (WGMs), have been efficiently employed in many applications, including sensing and low pump threshold lasing. The use of innovative materials, e.g. chalcogenide glasses, can extend the microsphere potential to medium infrared wavelength range [51-53].

In the previous chapter a Mid-infrared optical amplifier, consisting of a tapered chalcogenide $Ga_5Ge_{20}Sb_{10}S_{65}$ fiber coupled to an Er^{3+}doped microsphere made of the same glass, was optimized by means of a particle swarm optimization (PSO) approach [29].

In this chapter, microspherical WGM modes are not used for lasing or for sensing bio/chemical molecules lying in the environment around the microsphere. They are proposed, for the first time to the best of our knowledge, for the evaluation of rare-earth electronic and optical properties. This objective is reached through:

i) the accurate electromagnetic modelling of WGMs resonating in the rare-earth doped microsphere [1, 12-13];
ii) the utilization of a proper inversion algorithm, based on PSO procedure [29-34].

The PSO procedure solves the above-mentioned nonlinear problem with a global and stochastic solution search. The feasibility of the proposed method is theoretically investigated and proved via a self-

consistent approach. The interest and novelty of this method lies in the capability to recover unknown rare-earth parameters by employing rare-earth doped glass samples with extremely small sizes, in fact the microsphere typical diameters ranging from tens to hundreds of micrometers. More precisely, the spectroscopic parameters can be indirectly evaluated via the optical gain measurement of the fiber taper coupled to microsphere amplifier. The fiber taper / microsphere set-up with the proposed PSO approach could substitute the high-cost instrumentations used for spectroscopic measurements. As an example, an erbium doped chalcogenide glass microsphere is considered. However, the method is general. Different glasses and dopants could be similarly investigated.

Moreover, a high number of microspheres, made of suitable rare-earth doped glass, could be employed as punctual sensors for a number of different measurands. As example, this system can be used to obtain a radiation dose map, given that RIA (radiation-induced absorption) and other spectroscopic parameters depend on the dose rate of the ionizing emissions, which are present in space, nuclear power plants, radio medicine and radio pharmacy plants [36]. Therefore, the previously mentioned microsphere amplifiers could constitute an alternative to radiation distributed-fiber-sensors.

4.3. Rare-earth spectroscopic characterization

An amplifier constituted by a fiber taper coupled to an erbium doped glass microsphere is designed following the procedure described in the previous chapter. The ad-hoc developed model [12-13, 29] allows the calculation of:

i) the resonance frequencies, the electromagnetic field profiles and propagation constants of WGMs;
ii) the coupling of the optical power between the tapered fiber and the microsphere WGMs;
iii) the interaction of WGMs with microsphere erbium ions via the rate equations of the ion level populations;
iv) the time evolution of WGM powers inside the microsphere.

The transitions among the erbium energy levels, the amplified spontaneous emission and secondary transitions pertaining to the ion–ion interactions are included in the model. The simulations are performed by taking into account the wavelength dispersion of refractive index, the ion level lifetimes, the branching ratios, the absorption cross section measured on fabricated Er^{3+}: $Ga_5Ge_{20}Sb_{10}S_{65}$ bulk glass sample, the derived emission cross-section [12-13, 27-28]. Table 2.1 (see chapter 2) reports the spectroscopic parameter measured on erbium doped chalcogenide glass $Ga_5Ge_{20}Sb_{10}S_{65}$.

The time domain equation of the amplitude of the internal cavity electromagnetic field at the pump P and the signal S wavelength can be obtained by solving the differential equation 2.8 taking into account all

the above-mentioned physical interactions. The optical gain g for the amplifier is expressed in equation 2.7 and here reported:

$$g = \left| \frac{A^{y}_{out,WGM}}{A^{y}_{in,WGM}} \right|^2 = \left| \sqrt{1 - \frac{\tau}{\tau_{ext}}} + j \sqrt{\frac{\tau}{\tau_{ext}}} \frac{A^{y}_{WGM}}{A^{y}_{in,WGM}} \right|^2 \qquad (4.1)$$

with $y = P, S$.

where $A^{y}_{in,WGM}$ and $A^{y}_{out,WGM}$ are the amplitudes of the mode electric field at the input and at the output fiber section and coupled to the microsphere WGM$_{l,m,n}$; $\tau = 2\pi R_S n_{eff} / c$ is the circulation time inside the microsphere, n_{eff} WGM effective refractive index, c speed of light in vacuum; $\tau_{ext} = m\pi / \left(\omega_{WGM} \kappa^2 \right)$ coupling lifetime, κ coupling coefficient and ω_{WGM} resonance frequency of the WGM.

As well described in chapter 3, PSO emulates the social behaviour exhibited by a variety of animals during their search for food, e.g. bees, fishes, birds [29-34]. In the PSO algorithm, a population of N_b tentative solutions or particles corresponds to the swarm. The tentative solution is the position vector $\boldsymbol{p}_j$ of the *j-th* particle in the search space. At each iteration, the fitness function is evaluated for all the N_b tentative solutions. The particle trajectory depends on:

i) the location in the solution space where the best fitness value is experimented by itself, called personal best x_j^{PB};

ii) the best location found by the entire swarm, called global best x^{GB}.

The PSO boundary conditions here utilized are the so-called "invisible walls", i.e. the particles can move without limits, but, if they

escape from the solution space, the fitness is not evaluated. In this way, the boundary conditions do not interfere with natural swarm movement and computation time is reduced.

The PSO fitness function is here defined as expressed in 4.2:

$$F(\boldsymbol{p_i}) = \sum_{k=1}^{K} \left(g_k - g_k^j\right)^2 \qquad (4.2)$$

$$\text{with } j = 1,2,\ldots N_b \text{ , } k = 1,2,\ldots K$$

where g_k^j is the optical gain corresponding to the *j*-th particle, it is evaluated by using equation 4.1, i.e. the amplifier model gain, with the *k*-th pump power. g_k are the known simulated gains. They are measured in actual case. N_b is the number of particles. The convergence of the iterative optimization algorithm is reached by minimizing the fitness function *F*. The solution corresponds to the global best position $\boldsymbol{p}^{GB}$ in which the fitness absolute minimum is calculated. Figure 4.1 reports the flow chart for this PSO problem.

R_{PSO} is the number of position WM_{GBP}, the different PSO executions launched. The PSO weighted mean global best calculated for the set of the R_{PSO} executions, is defined as in equation 4.3:

$$WM_{GBP} = \frac{\sum_{r=1}^{R_{PSO}} \left(\boldsymbol{p}_r^{GB} \times \frac{1}{F\left(\boldsymbol{p}_r^{GB}\right)} \right)}{\sum_{r=1}^{R_{PSO}} \frac{1}{F\left(\boldsymbol{p}_r^{GB}\right)}} \qquad (4.3)$$

$$\text{with } r = 1,2,\ldots R_{PSO}$$

where $F\left(\boldsymbol{p}_r^{GB}\right)$is the global best fitness of the *r*-th executed PSO, i.e. the fitness calculated in the global best position $\boldsymbol{p}_r^{GB}$, with $l = 1, 2, \ldots, R_{PSO}$. The reciprocal of the global best fitness is chosen as weight because a smaller fitness value corresponds to a better PSO performance.

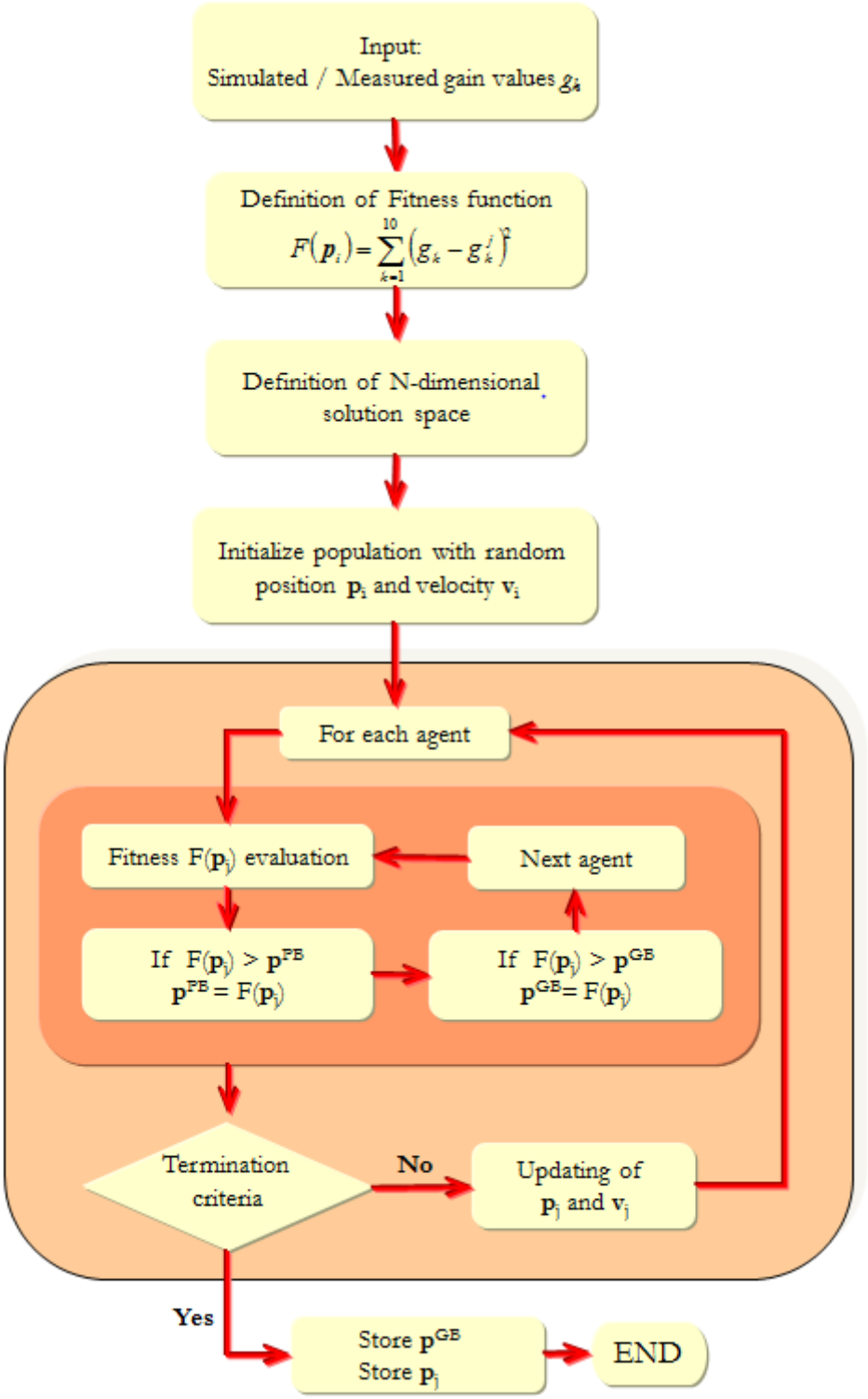

Fig. 4.1 Flow chart of the PSO algorithm used in rare-earth characterization problem.

In order to investigate the goodness of the proposed method, the percentage error between the PSO recovered parameters and the nominal/target parameters used in the model for the calculation of g_k is evaluated. The percentage error, for each parameter, is calculated in equation 4.4:

$$E_{\%} = \frac{\left| WM_{GBP} - V_{nom} \right|}{V_{nom}} \cdot 100 \qquad (4.4)$$

where V_{nom} is the nominal/target value of the considered parameter. This percentage error, if low enough with respect to the physical meaning of the parameter, constitutes a theoretical validation of the proposed approach.

4.3.1. Design of the erbium-doped amplifier for sensing

The erbium-doped amplifier has been designed and refined with the aim to maximize the amplifier optical gain. The PSO approach has been employed for the design of this kind of amplifier as described in the previous chapter and in [29]. The microsphere radius ρ_0, taper waist radius T_W, taper angle T_a and taper-microsphere gap G are optimized. The variation ranges were chosen by considering these technological needs:

i) a suitable microsphere radius in order to have resonance at both the pump and signal wavelengths;

ii) the waist radius larger than the inferior limit T_W = 0.5μm, since chalcogenide glass exhibits a number of drawbacks in the construction of taper having smaller waist;

iii) the waist radius smaller than the superior limit T_W = 1μm in order to have single-mode propagation;

iv) feasible taper angle and feasible taper–microsphere gap.

On the basis of preliminary simulations and of previous design experiences, the limits of the parameter ranges (solution space limits), are roughly fixed so that their optimized values and the corresponding maximum gain can be found within the fixed solution domain. Thickness of the erbium-doped region (close to the microsphere surface) is h_{Er} = 3 μm, erbium concentration is C_{Er} = 0.5 w%. The input pump power is P_p = 0.1 W and the input signal power P_s = −50 dBm.

The cognitive parameter is c_1 = 1.494, the social parameter is c_2 = 1.494, the maximum number of iteration is I_{PSO} = 32 the inertia weight I_w is a vector with I_{PSO} elements linearly spaced from 0.4 to 0.9. The number of the particles of the swarm is N_b = 32.

The physical parameters, the solution domain limits and the PSO optimized values are summarized in Table 4.1. The designed amplifier has the following parameters:

- Microsphere radius ρ_o = 25 μm;
- Taper waist radius T_W = 981 nm;
- Taper angle T_a = 0.03 rad;
- Taper – microsphere gap G = 518 nm.

Table 4.1 Fixed physical parameter and settings of PSO

Fixed physical parameters	
Parameter	Value
Input Signal Power P_s [dBm]	- 50
Input Pump Power P_p [W]	0.1
Thickness of erbium-doped region h_{Er} [μm]	3
Erbium concentration C_{Er} [w%]	0.5

Settings of PSO		
Parameter	Solution domain limits	PSO optimized value
Microsphere radius ρo [μm]	10 - 30	25
Taper waist radius T_w [nm]	500 – 1000	981
Taper angle T_a [rad]	0.001 – 0.04	0.03
Taper–microsphere gap G [nm]	500 – 1000	518

By varying the parameter n from 1 to 3 and by imposing $l = m$, ten different resonant WGMs are simulated in the wavelength range from 2740–2820 nm. WGMs with $l \neq m$ have been neglected because they exhibit low overlapping factor $\Omega^{s}_{l,m,n}$ (see equation 2.3 in chapter 2). WGM competition, i.e. their amplification or attenuation, strongly depend on the absorption and emission cross sections at their peculiar resonant wavelength. For each WGM, all the spectroscopic and physical parameters (refractive index, emission cross section, absorption cross section etc.) are evaluated at the proper resonance frequency. In Table 4.2 the main characteristics of these resonating modes are reported. The resonance wavelength λ_r, the modal parameters l, m and n, the optical gain g and the intrinsic quality factor Q for each WGM mode are listed. Figure 4.2 illustrates the optical gain g for the different WGMs.

Table 4.2 PSO optimized amplifier. Parameters $l = m$ and n of WGMs, resonance wavelength, output power and optical gain.

$l=m$ values	n values	WGM resonance wavelength λ_r [nm]	P_{out} [dBm]	Optical gain g [dB]	Quality factor Q [$\cdot 10^7$]
116	1	2805	-42.7	7.3	9.06
117	1	2782	-40.8	9.2	9.11
118	1	2759	-37.5	12.5	9.15
109	2	2808	-45.7	4.3	8.75
110	2	2784	-44.5	5.5	8.80
111	2	2761	-42.5	7.5	8.84
103	3	2817	-47.3	2.7	8.48
104	3	2793	-46.7	3.3	8.52
105	3	2769	-45.2	4.8	8.57
106	3	2747	-46.7	3.3	8.62

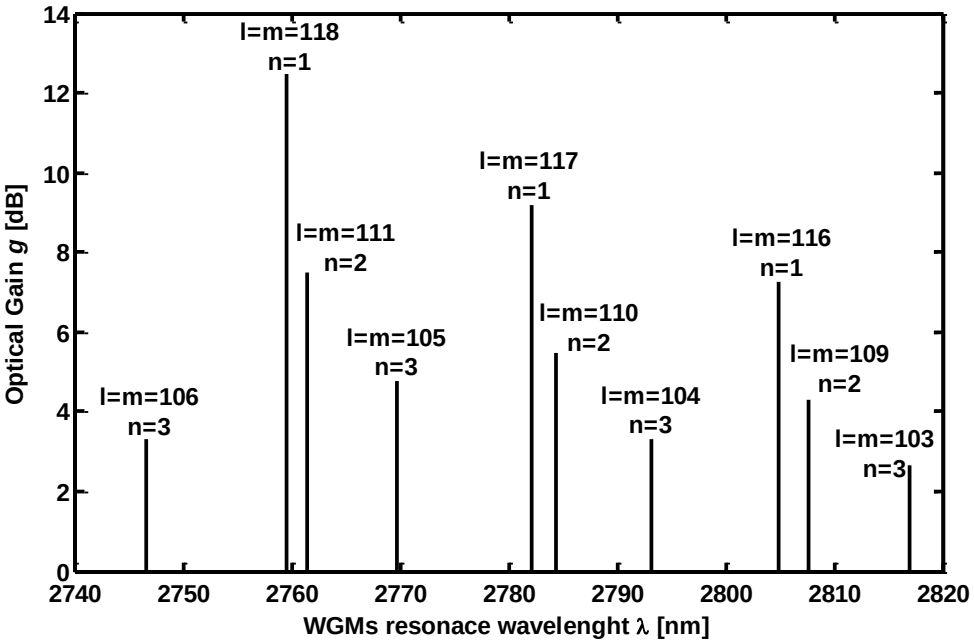

Fig. 4.2 Simulated optical gain g of the WGMs versus wavelength.

The WGM maximizing the amplifier gain has modal order n = 1; l = m = 118 at the signal wavelength close to λ_s = 2760 nm. By further calculations, the most suitable WGM at the pump wavelength, close to λ_p= 980 nm, has modal order n = 1; l = m = 352. In Table 4.3 the main characteristics of the optimized amplifier, the signal and pump wavelengths, the intrinsic signal lifetime and the coupling signal lifetime are reported.

Table 4.3 Characteristics of the DPSO optimized amplifier

Variable	Value
Signal WGM mode	*n = 1 ; l = m = 118*
Signal wavelength λ_s [nm]	*2800*
Refractive index of microsphere n_s and taper n_f at signal wavelength	*2.2253*
Pump WGM mode	*n = 1 ; l = m = 352*
Pump wavelength λ_p [nm]	*980*
Refractive index of microsphere n_s and taper n_f at pump wavelength	*2.2751*
Intrinsic signal lifetime τ_0 [μs]	*0.134*
Coupling signal lifetime τ_{ext} [ns]	*0.0869*

4.3.2. Rare-earth characterization via PSO algorithm

The microsphere amplifier obtained in the previous section is simulated for the input signal power P_s = −50 dBm and for K = 10 different pump powers in order to calculate ten corresponding g_k gain values, k=1,2,…10. The calculated gains g_k (in actual cases they could be substituted by measured ones) are reported in Table 4.4. The calculated gain g_k, circles, versus the input pump power P_p are reported in Figure 4.3, the full curve linearly interpolates the simulated points. The fiber input

pump powers listed in Table 4.4 are arbitrarily chosen. Lower pump powers can be used to avoid thermal effects.

Table 4.4 Chalcogenide microsphere amplifier. Simulated optical gain g_k.

Input pump power P_p [mW]	g_k [dB]
20	0.70
40	1.31
60	1.94
80	2.71
100	11.72
120	11.74
140	11.76
160	11.77
180	11.80
200	11.90

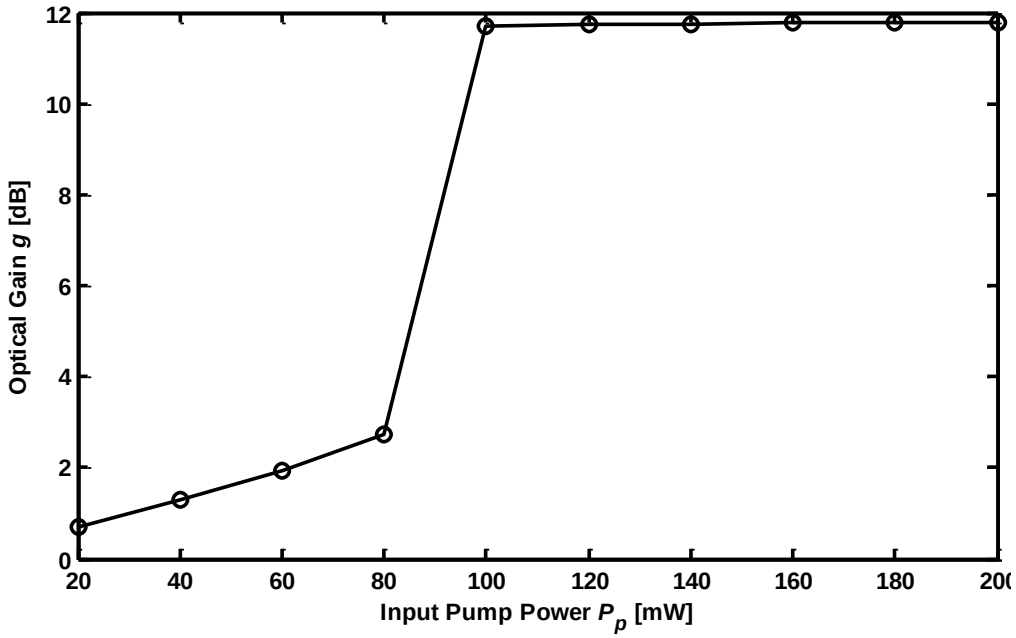

Fig. 4.3 Calculated optical gain g_k (circles) versus the input pump powers P_p. Input signal power is S_P=-50 dBm. The full curve linearly interpolates the simulated points.

The calculated gains g_k are employed in equation 4.2 as input data in the PSO code, suitably integrated with the model of the fiber taper coupled to an erbium doped glass microsphere. More precisely, the PSO approach is applied in order to recover the parameters of the rare-earth glass. Figure 4.4 illustrate the erbium energy levels with the transition considered in the numerical model.

Firstly, the PSO is applied to recover the up-conversion and cross-relaxation coefficients C_{up}, C_3, C_{14}, of the erbium ions doping the chalcogenide microsphere [60], by supposing all the other model parameters as known ones. The maximum number of PSO iterations I_{PSO} and the number of particles N_b are $I_{PSO} = N_b = 24$. The number of complete PSO runs is $R_{PSO} = 20$. The PSO target values are the parameter values used in the direct simulation for the calculation of the ten reference/target gains g_k reported in Table 4.4. The solution search ranges for the ion-ion interaction parameters C_3, C_{up}, C_{14} are $1{\cdot}10^{-23}$ – $3{\cdot}10^{-23}$, $2{\cdot}10^{-23}$ – $4{\cdot}10^{-23}$, $4{\cdot}10^{-24}$ – $6{\cdot}10^{-24}$ m^3/s, respectively.

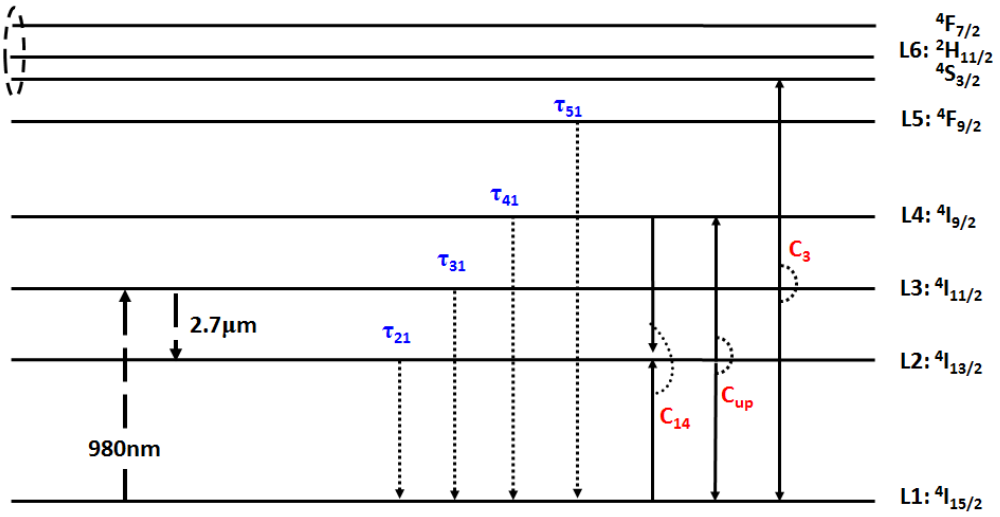

Fig. 4.4 Erbium energy levels. Pump wavelength is λ_P = 980nm, signal wavelength is λ_S = 2.7µm.

Table 4.5 reports the target values, the corresponding recovered values WM_{GBP}, the PSO percent error $E_{\%}$ [%] and the PSO standard deviations SD.

The WM_{GBP} recovered values of C_3, C_{up} and C_{14} are in excellent agreement with the target values, indeed the largest percent error $E_{\%}$ = 0.18% is pertaining to C_{14}. It is worthwhile to note that the experimental determination of these coefficients is quite difficult.

The PSO approach has allowed the recovering of the unknown parameters with a calculation time of about 6 hours per PSO run (N=24, I=24) by employing a CPU i7-4770.

The PSO has been also used to recover the values of ion lifetimes τ_{21}, τ_{31} and τ_{41}, for the transitions $^4I_{13/2} \rightarrow {}^4I_{15/2}$, $^4I_{11/2} \rightarrow {}^4I_{15/2}$, $^4I_{9/2} \rightarrow {}^4I_{15/2}$, respectively. The solution search ranges for the ion lifetimes τ_{21}, τ_{31} and τ_{41}, are in all the three cases 0.1 – 3 *ms*. The number of complete PSO executions is R_{PSO} = 20. Table 4.6 reports the target values, the corresponding recovered values WM_{GBP}, the PSO percent error $E_{\%}$ [%] and the PSO standard deviations SD.

Table 4.5 Results of characterization of up-conversion and cross-relaxation coefficients

Variable	Target Value	PSO Weighted Mean WM_{GBP}	Percent Error $E_{\%}$ [%]	PSO Standard Deviation SD
C_3 [m^3/s]	$2 \cdot 10^{-23}$	$2.00 \cdot 10^{-23}$	0	$5.44 \cdot 10^{-28}$
C_{up} [m^3/s]	$3 \cdot 10^{-23}$	$3.00 \cdot 10^{-23}$	0	$3.22 \cdot 10^{-27}$
C_{14} [m^3/s]	$5 \cdot 10^{-24}$	$4.99 \cdot 10^{-24}$	0.18	$2.37 \cdot 10^{-26}$

Good results are obtained also for τ_{21}, τ_{31} and τ_{41}, the largest percent error $E_{\%}$= 3.37 % is found for τ_{41}. We underline that, in actual cases, lifetimes are typically evaluated by fluorescence decay (Judd-Ofelt calculation) and are affected by larger errors (5%–10%).

The PSO approach has allowed the recovering of the unknown parameters with a calculation time of about 6 hours per PSO execution (N=24, I=24) by employing a CPU i7-4770.

Figure 4.5 reports the function $-\log(F(\boldsymbol{p}_i))$ plotted versus C_3–C_{up} pairs. The positions of the 24 particles at the end of the best PSO execution are illustrated by the marks. The color represents the intensity of the function $-\log(F(\boldsymbol{p}_i))$. The global best position for the executed PSO is that maximizing $-\log(F(\boldsymbol{p}_i))$, the peak corresponds to the absolute minimum of *F*. The PSO algorithm convergence is apparent: all the particles are very close to the peak.

Table 4.6 Results of characterization of ions lifetimes

Variable	Target Value	PSO Weighted Mean WM_{GBP}	Percent Error $E_{\%}$ [%]	PSO Standard Deviation *SD*
τ_{21} [ms]	1.83	1.822	0.45	$2.66 \cdot 10^{-5}$
τ_{31} [ms]	1.37	1.369	0.04	$2.49 \cdot 10^{-6}$
τ_{41} [ms]	1.08	1.116	3.37	$6.86 \cdot 10^{-5}$

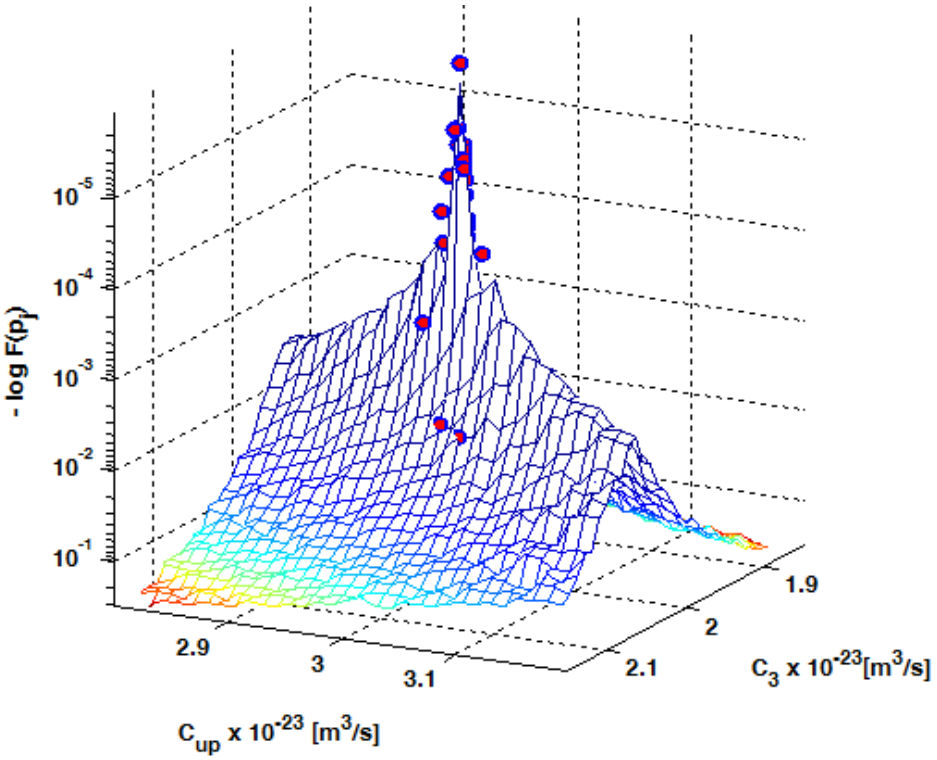

Fig. 4.5 Function – log (F (x_i)) versus C_3–C_{up} pairs and position of the 24 particles (marks) at the end of a PSO execution.

4.4. PSO convergence

As example of PSO convergence, Figures 4.6, 4.7 and 4.8 report the particles behavior for the best PSO launch (i.e. exhibiting the lowest final fitness) in the case of C_3, C_{up} and C_{14} characterization. In this PSO problem, fitness function F, defined in equation 4.2, must be minimized, then the best fitness F^B and the worst fitness F^W are respectively the lowest and the highest fitness experimented by all the swarm for each iteration. The average best fitness in a single iteration of a PSO launch versus the number of particle N_b is defined in equation 4.5:

$$F^{AV}(\boldsymbol{p}_i) = \sum_{j=1}^{N_b} \frac{F(\boldsymbol{p}_j{}^{GB})}{N_b} \tag{4.5}$$

Figure 4.6 illustrates in logarithmic scale i) the worst fitness F^W ii) the average fitness F^{AV} and iii) the best fitness F^B versus the iteration number, where I_{PSO} = 24 is the number of computed iterations for the single PSO run. The three curves show that the entire swarm exhibits a decreasing fitness by increasing the iterations, i.e. the particles are converging towards the target.

Figure 4.7 shows the swarm movement in C_3 search space with respect to the target $C_3 = 2 \times 10^{-23} m^3/s$. Considering the set of particles positions in the research space for each iteration, Figure 4.7 shows the upper (Up-B, circular mark) and lower (Low-B, cross mark) bound of the aforesaid set, the best position (full curve) and target value (dot curve) versus the PSO iteration number. It is apparent that the distance between upper and lower bound decreases by increasing the iteration number, i.e. the particles are converging towards the target.

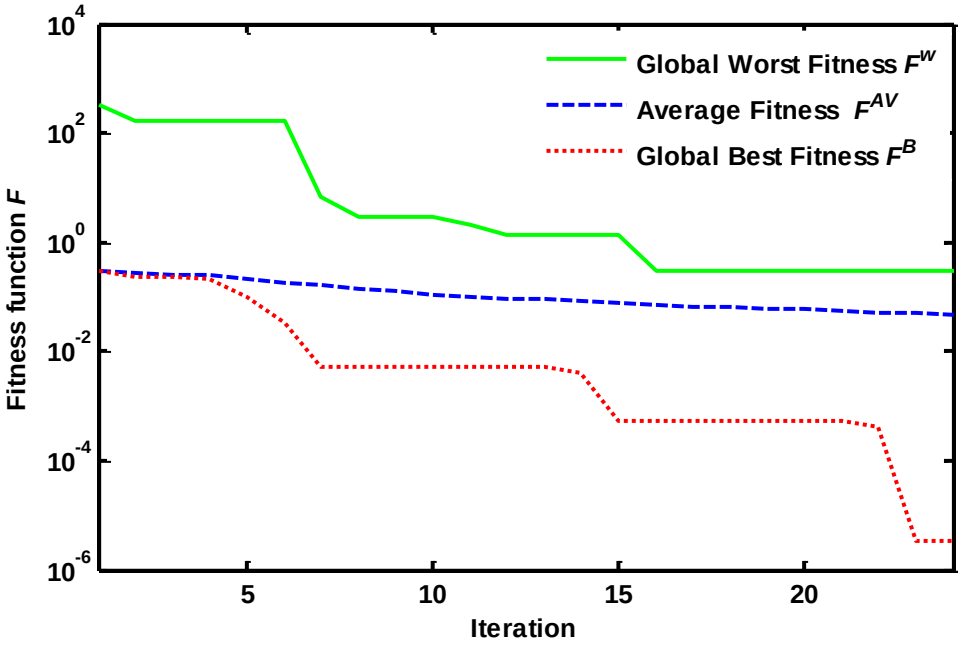

Fig. 4.6 Global worst fitness F^W (full line), average fitness F^{AV} (dash line) and gloval best fitness F^B (dot line) versus the PSO iteration for the best PSO launch (i.e.

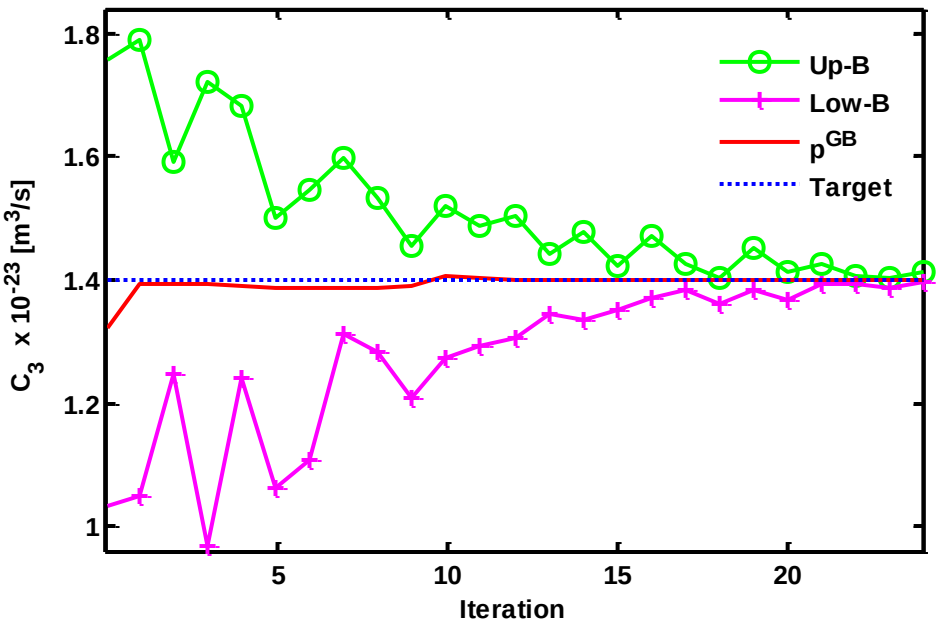

Fig. 4.7 Upper bound Up-B (circular mark), lower bound Low-B (cross mark), the best position p^{GB} (full curve) and target value (dot curve) of C_3 versus the PSO iteration for the best PSO launch (i.e. exhibiting the lowest final fitness) in C_3,C_{up},C_{14} characterization.

Figure 4.8 illustrates the positions of all the particles for the best PSO launch (i.e. exhibiting the lowest final fitness) in PSO initialization, iteration number 8, 16 and 24 (the last one). The black dots represent the particles, the red star represents the target. It is apparent the converging behaviour of the particles.

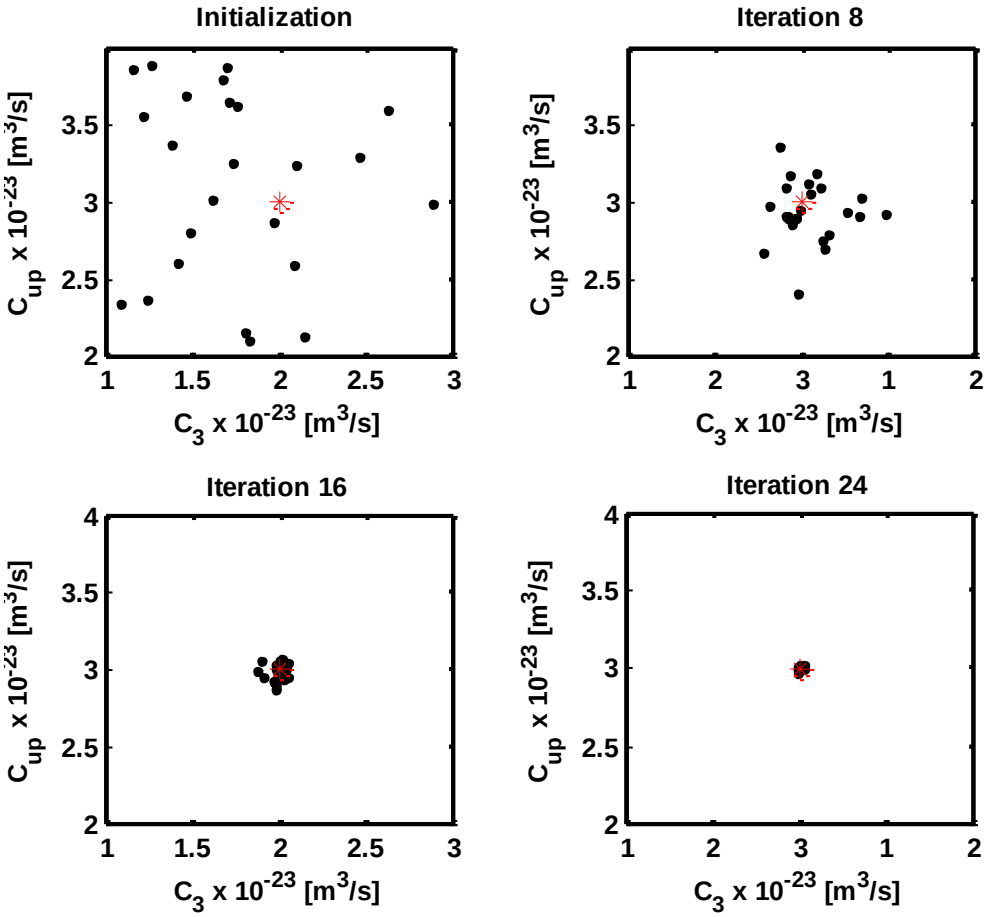

Fig. 4.8 Positions of all the particles for the best PSO launch (i.e. exhibiting the lowest final fitness) in PSO initialization, iteration number 8, 16 and 24 (the last one).

Figure 4.9 illustrates the positions in a very narrow range in the C_3 - C_{up} search space of the N_b = 24 particles in the last iteration (I_{PSO} = 24), i.e. when the convergence of all the particles is the highest. The black dots represent the particles, the red star represents the target. The contour plot represents the logarithm of fitness function F. It is apparent that the convergence is very high.

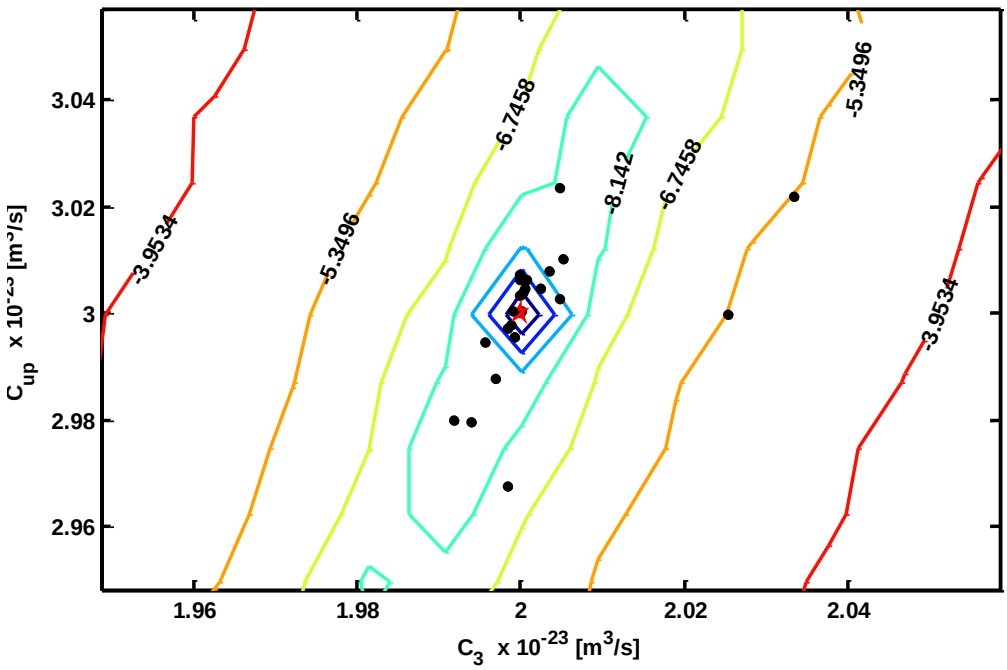

Fig. 4.9 Position in C_3-C_{up} search space of the N_b = 24 particles in the last PSO iteration iteration for the best PSO launch (i.e. exhibiting the lowest final fitness). The black dots represent the particles, the red star the target. The contour plot represents the logarithm of fitness function F.

4.5. Characterization sensibility to the input parameter

The goodness of the characterization depends on measured input parameter that are affected by an uncertainty. It is interesting to investigate the effect that uncertainty of the various input parameters has on the characterization results. An error is introduced on the input parameters with respect to the nominal value and the characterization procedure is repeated (R_{PSO} = 20 PSO launches) in order to obtain the deviation of the output. In particular, we evaluated how the uncertainty in the ion-level lifetimes and branching ratio measurements from [28] influences the recovering of ion-ion interaction parameters. The solutions search spaces for C_3, C_{up} and C_{14} are respectively: $1{\cdot}10^{-23}$ - $3{\cdot}10^{-23}$, $2{\cdot}10^{-23}$ - $4{\cdot}10^{-23}$, $4{\cdot}10^{-24}$ - $6{\cdot}10^{-24}$ m^3/s. Table 4.7 reports for any modified input values: the amount of introduced error, the recovered values weighted mean WM_{GBP} with percent error $E_{\%}$ and the PSO standard deviation SD.

In the worst case, i.e. if τ_2 value is increased from its nominal value τ_2 = 1.83 ms to τ_2 = 2.013 ms (error of 10%), there is an error of about $E_{\%}$ = 17.73% on C_{up} parameter recovered via PSO with respect to the target value. The uncertainty on τ_3 and τ_4 causes error much slighter on PSO recovering. The uncertainty of 20% on β_{32} (and then β_{31} uncertainty of 3.4%) in the worst case causes an error of about $E_{\%}$ = 33.3% on C_{up} parameter. It is important consider that i) large error of the input parameter are supposed in these cases to test the method, ii) the ion ion interaction parameter C_{up} is not easily measurable, thus the PSO allows in any case an interesting characterization.

Table 4.7 Characterization sensibility to the input error

Variable		*Target*	*Search ranges*	
C_3		$2 \cdot 10^{-23}$ m³/s	$1 \cdot 10^{-23}$ - $3 \cdot 10^{-23}$ m³/s	
C_{up}		$3 \cdot 10^{-23}$ m³/s	$2 \cdot 10^{-23}$ - $4 \cdot 10^{-23}$ m³/s	
C_{14}		$5 \cdot 10^{-24}$ m³/s	$4 \cdot 10^{-24}$ - $6 \cdot 10^{-24}$ m³/s	
Error / Nominal value N_v		C_3	C_{up}	C_{14}
Modified variable : τ_2				
Error = 10% N_v=1.83ms	WM_{GBP} [m³/s]	$2.00 \cdot 10^{-23}$	$3.53 \cdot 10^{-23}$	$4.90 \cdot 10^{-24}$
	$E_{\%}$ [%]	- 0.15	17.73	- 2.07
	SD	$1.84 \cdot 10^{-26}$	$6.13 \cdot 10^{-26}$	$5.33 \cdot 10^{-25}$
Modified variable : τ_3				
Error = 10% N_v=1.37ms	WM_{GBP} [m³/s]	$2.24 \cdot 10^{-23}$	$3.12 \cdot 10^{-23}$	$5.49 \cdot 10^{-24}$
	$E_{\%}$ [%]	11.83	4.01	9.85
	SD	$2.15 \cdot 10^{-26}$	$7.31 \cdot 10^{-26}$	$4.65 \cdot 10^{-25}$
Modified variable : τ_4				
Error = 10% N_v=1.08ms	WM_{GBP} [m³/s]	$2.01 \cdot 10^{-23}$	$3.14 \cdot 10^{-23}$	$4.99 \cdot 10^{-24}$
	$E_{\%}$ [%]	0.27	4.78	-0.27
	SD	$1.88 \cdot 10^{-26}$	$6.58 \cdot 10^{-26}$	$4.07 \cdot 10^{-25}$
Modified variables : β_{31} / β_{32}				
β_{32} : *Error = 20%* N_v=14% β_{31} : *Error = 3.4%* N_v=86%	PSO_{WM} [m³/s]	$1.84 \cdot 10^{-23}$	$4 \cdot 10^{-23}$	$5.32 \cdot 10^{-24}$
	$E_{\%}$ [%]	-7.84	33.31	6.44
	SD	$2.70 \cdot 10^{-26}$	$5.90 \cdot 10^{-27}$	$4.77 \cdot 10^{-25}$

4.6. Summary

For the first time WGM resonances are proposed for a complete characterization of rare-earth doped glasses via PSO approach. As an example, C_3, C_{up}, C_{14}, τ_{21}, τ_{31}, and τ_{41} are recovered. The largest percent error, less than 3.5%, refers to τ_{41}. Although the recovering of rare-earth parameters via PSO is successfully applied by employing standard fiber amplifiers [36], WGM resonance allows much higher precision and accuracy [33]. The fiber taper coupled to the microsphere amplifier could substitute high-cost instrumentations employed for spectroscopic measurements. The very high efficiency of the proposed method is originated from the resonant WGM properties, allowing the interaction of the electromagnetic field for long effective distances, due to the extremely high number of WGM circulations along orbits close to the microsphere surface.

A calibration of the measurement system could be necessary since taper waist and taper-microsphere gap cannot be known to the nanometer scale. Alternatively, the taper waist and taper-microsphere gap can be considered as unknown parameters to be recovered in addition to the rare-earth ones but longer calculation time is required [29]. In actual cases, the errors $E_{\%}$ and the standard deviations SD of PSO recovered values depend on the uncertainty of the parameters employed in the model. Next chapter will be focused to take into the account the effect of model parameter uncertainty on PSO recovered values.

Chapter 5

Enhanced optical sensing via microsphere WGM resonance[3]

5.1. Introduction

Sensing by means of resonant whispering gallery modes (WGMs) reported in previous chapter exhibits various drawbacks and critical points related to the microsphere and tapered optical fiber fabrication tolerance. The uncertainty on the fiber taper and microsphere geometry or the gap between the microsphere and the fiber taper can complicate or limit the actual use of these devices for sensing, requiring peculiar calibration of the WGM based sensing set-up. An alternative double-step approach is proposed in this chapter. In particular, the geometrical parameters of the set-up are recovered preliminarily and then the rare-earth parameters are recovered via simple transmittance /gain measurements. The method is based on the refined electromagnetic model of the device developed in the previous chapters suitably integrated with the particle swarm optimization (PSO) approach. The percent errors made on the up-conversion coefficients C_{up} and C_3 are extremely low, being 0.75%, 0.05%, respectively. The procedure is very robust. It can be applied

[3] Work presented in this chapter has appeared in [61]: G. Palma, M. C. Falconi, F. Starecki, V. Nazabal, T. Yano, T. Kishi, T. Kumagai, and F. Prudenzano, "Novel double step approach for optical sensing via microsphere WGM resonance," *Optics Express*, vol. 24, no. 23, pp. 26956 – 26971, (2016).

more in general, allowing the sensing of other physical parameters via simple transmittance measurements instead of wavelength shift ones.

5.2. Bio-detection via chalcogenide microspheres

As described in previous chapters, whispering gallery modes confined in dielectric microspheres can be employed for high performance sensing. Two approaches have been developed for bio-detection via microspheres:

i) Absorption-based approach, requiring evanescent electromagnetic field coupling to selected WGMs;

ii) Fluorescence-based technique [62-66].

These applications promise novel sensing systems for label-free chemical/biological monitoring. Using these approaches, the physical parameters of the medium/background surrounding the microsphere can be efficiently monitored. As example, in [67] a packaged structure for the microsphere-taper coupling system is proposed. As reported in figure 5.1, it is constructed by encapsulating the coupling region with a suitable polymer. The spot-packaged structure, integrated with a standard fiber, is an example of feasible structure that could be engineered.

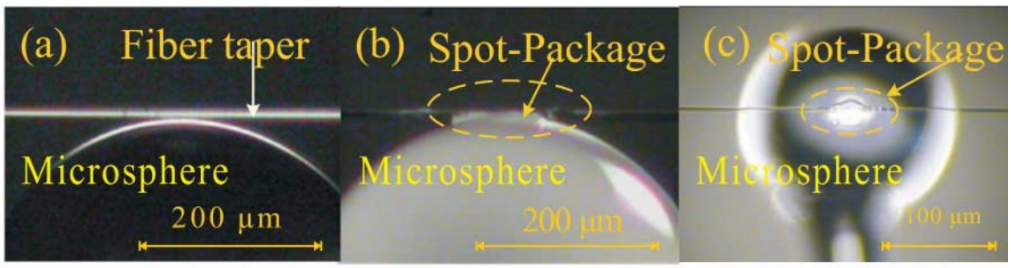

Fig. 5.1 Representations of a taper coupled microsphere (a) before and (b) after the spot-package process. (c) Side view of the packaged structure [67].

Microspheres of silica, tellurite, phosphate and ZBLAN glasses, doped with rare-earths, have been fabricated, providing low threshold lasing and comb-like emission with extremely narrow linewidth [46-50, 68-69]. The employment of novel materials, e.g. chalcogenide glasses, could allow novel applications in the medium infrared wavelength range, such as active and passive sensing [51-53].

In chapter 3, the particle swarm optimization (PSO) approach is proposed in order to optimize a Mid-Infrared amplifier constituted by an Er^{3+}-doped microsphere coupled to a tapered fiber [29]. In chapter 4, the PSO procedure is proposed, in principle, to recover the unknown spectroscopic parameters of the microsphere glass, i.e. for characterization [59].

In this chapter, the PSO procedure employed for characterization is indicated with the acronym CPSO (Characterization PSO problem). CPSO approach could be employed, more in general, for sensing chemical compounds/mixture or biomolecules lying in the environment around the microsphere or within a microbubble. As described in chapter 4, CPSO procedure exhibits some drawbacks and critical points related to the fabrication of microsphere and tapered optical fiber. In particular, the uncertainty on the taper and microsphere geometry or gap between the microsphere and the fiber taper could dramatically complicate the CPSO performance and then the actual employment.

Therefore, the device fabrication tolerance has to be taken into account. In this chapter, a number of practical aspects are accurately investigated. As example of application, an erbium doped chalcogenide glass microsphere coupled to a fiber taper has been considered for

spectroscopic measurements. The system feasibility is theoretically demonstrated via a self-consistent approach. In particular, we propose for the first time to use the CPSO twice (double-step CPSO) in order to perform reliable measurements. At first, CPSO is used for an accurate evaluation of the geometrical parameters of the set-up constituted by the fiber taper coupled to a microsphere. Then, CPSO is used for the recovery (evaluation) of the spectroscopic parameters of the microsphere made of rare-earth doped glass. The double-step CPSO allows extremely accurate and precise recovering of spectroscopic parameters.

The high efficiency of the double-step CPSO is due to the interaction of the WGM resonant modes with the medium, for very long effective lengths, combined with the PSO global search method that is applied for the geometry parameter identification before the physical characterization. The strength of the proposed double-step CPSO procedure lies in the use of simple output signal measurements as basis data for accurate and low cost recovery of both the set-up geometrical parameters and the unknown rare-earth parameters. This novel approach is very promising and can be generalized to other rare-earths or to different sensing set-ups (including microbubbles) for detection of various types of analytes. It is feasible also with reference to label-free chemical detection.

5.3. Double step approach for optical sensing

As described in chapter 3, the PSO procedure is a global search numerical method [29-35]. The tentative solutions are represented by the positions $\boldsymbol{p}_j$ of the N_b particles of the swarm with velocities $\mathbf{v}_j$ in a search space, the so-called solution domain, updated by the algorithm in order to optimize an objective function, the fitness. The movement of each particle depends on three factors:

i) the cognitive factor, related to the personal best position $\boldsymbol{p}^{PB}$, i.e. the location in the solution space corresponding to the best value of objective function experimented by the considered particle;

ii) the social factor, related to the global best position $\boldsymbol{p}^{GB}$, i.e. the location in the solution space corresponding to the best value of objective function experimented by the whole swarm;

iii) the inertial factor, i.e. a suitable resistance to the change of the particle direction.

Each of these factors is weighted by an ad hoc parameter: the cognitive parameter c_1, the social parameter c_2, the inertia weight I_w. The PSO procedure ends when a suitable convergence criterion is satisfied. The global best position $\boldsymbol{p}^{GB}$ is the optimized solution, i.e. the position where the fitness is optimized, i.e. maximized or minimized depending on the type of the problem.

Firstly, in double step approach a reference sensing system (RSS) constituted by a fiber taper coupled to an erbium-doped microsphere has

to be designed. As described in chapter 1, in this kind of amplifier, the evanescent field of the optical fiber propagation modes tunnels in the microsphere via the taper. Therefore, the excitation of WGMs is achieved. The interactions of both pump and signal beams with the rare-earth doped glass allow the signal optical amplification. The RSS is simulated using the model developed in previous chapters [1, 59]. More generally, the RSS could be an arbitrary sensing set-up for which the output characteristics can be directly measured. However, the CPSO procedure needs to have a numerical model of the RSS. Indeed the key element of CPSO algorithm is to recover the RSS parameters in order to obtain a sensing set-up model matching the measured output characteristics (data).

The CPSO procedure is divided in two subsequent steps:

G) *geometrical characterization*: the CPSO is used for an accurate evaluation of the RSS dimensions;

S) *spectroscopic characterization*: using the geometrical sizes obtained in the previous step G), the CPSO is used for an accurate evaluation of the spectroscopic parameters.

In the first step, G), the RSS is considered as a passive system, i.e. the interaction of light with rare-earth is neglected.

In this second step, S), the CPSO is applied for the characterization of the rare-earth doped glass, therefore the interaction of light with rare-earth is considered. The lifetimes, the up-conversion coefficients and the branching ratio can be recovered.

The CPSO fitness function Φ_C, evaluated in particle position $\boldsymbol{p}_j$, is defined in equation 5.1:

$$\Phi_C(\boldsymbol{p}_j) = \sum_{k=1}^{N_p} \left(RC_k - RC_{CPSO,k}^{j} \right)^2 \qquad (5.1)$$

with $j = 1,2,\ldots,N_b$, $k = 1,2,\ldots,N_p$.

The fitness function must be minimized. RC_k is the *k*-th measured RSS output characteristic. In particular:

- in geometrical characterization G), being RSS a passive system, RC_k is the output signal power $S_{p,k}^{out}$, as a function of the wavelength, obtained for the *k*-th input signal power $S_{p,k}$;
- in spectroscopic characterization S), being RSS an active system, RC_k is the optical gain g_k obtained for the *k*-th input pump power P_p.

It is worthwhile to remark that in actual sensing set-ups RC_k has to be directly measured via an optical detector. In this work, it is simulated by considering the RSS model with nominal geometrical and measured spectroscopic parameters.

$RC_{CPSO,k}^{j}$ is the output characteristic (output signal power in passive model or gain in active model) simulated for the *j*-th particle of the swarm, i.e. calculated in the *j*-th particle position within the solution space.

The CPSO algorithm and the set-up, comprising the tapered fiber coupled to the microsphere, constitute the proposed tool for characterization / biosensing.

R_{CPSO} is the number of the different CPSO executions. The weighted mean WM_{GBP} of the CPSO global best positions, evaluated by considering all the R_{CPSO} performed executions, is calculated by means of equation 5.2:

$$WM_{GBP} = \frac{\sum_{r=1}^{R_{CPSO}} \left(\boldsymbol{p}_r^{GB} \times \frac{1}{\Phi_c\left(\boldsymbol{p}_r^{GB}\right)} \right)}{\sum_{r=1}^{R_{CPSO}} \frac{1}{\Phi_c\left(\boldsymbol{p}_r^{GB}\right)}} \tag{5.2}$$

where $\Phi_c\left(\boldsymbol{p}_r^{GB}\right)$ is the global best fitness, i.e. the fitness calculated in the global best position $\boldsymbol{p}_r^{GB}$ for the r-th CPSO execution, with $r = 1, 2, \ldots, R_{CPSO}$. The reciprocal of the global best fitness is used as weight in mean calculation because a smaller fitness value corresponds to a better CPSO performance.

In order to investigate the goodness of the proposed method, the percentage error between the CPSO recovered parameters, $WM_{GBP,}$ and the V_{nom} nominal/target parameters used in the RSS model for the calculation of RC_k is evaluated. The percentage error, for each parameter, is calculated by equation 5.3:

$$E_{\%} = \frac{\left| WM_{GBP} - V_{nom} \right|}{V_{nom}} \cdot 100 \tag{5.3}$$

This percentage error, if low enough with respect to the physical meaning of the recovered parameter, validates the proposed approach.

5.4. Design of the set-up and simulated results

For the modeling of the amplifier constituted by the rare-earth doped microsphere coupled to the fiber taper, the theory presented in chapters 1 and 2 is implemented in a computer code allowing the calculation of the optical gain.

5.4.1. Design of the reference system RSS

The pump wavelength is close to λ_p = 980 nm and the signal wavelength is close to λ_s = 2770 nm. In order to carry out a realistic gain calculation, the simulations are performed by considering measured spectroscopic parameters of an Er^{3+}:$Ga_5Ge_{20}Sb_{10}S_{65}$ glass sample. The refractive index wavelength dispersion is modelled by means of the Cauchy equation, with measured spectroscopic parameters [12-13, 27-28] reported in Table 2.1 (chapter 2). The simulation is performed by varying the parameter n of $WGM_{l,m,n}$ from 1 to 3 and by imposing $l = m$ (fundamental mode). WGMs with $l \neq m$ are neglected because they exhibit low overlapping factor $\Omega^{s}_{l,m,n}$, see equation 2.3 in chapter 2. WGMs competition, i.e. their amplification or attenuation, strongly depends on the absorption and emission cross sections at their peculiar resonant wavelength. Therefore, the different emission and absorption cross section values are accurately taken into account for the modelling of the $WGM_{l,m,n}$ resonating at different wavelengths. Figure 2.4 and 2.5 report the absorption and emission cross section in Er^{3+}-doped $Ga_5Ge_{20}Sb_{10}S_{65}$ glass. The absorption cross section at the pump wavelength λ = 980 nm is close to 1.32×10^{-24} m^2, while the emission and absorption cross sections at the signal wavelength λ = 2770 nm are close to 1.4×10^{-24} m^2 and 1.23×10^{-24} m^2,

respectively. The thickness of the erbium-doped region (close to the microsphere surface) and the erbium concentration are h_{Er} = 3 μm and C_{Er} = 0.5 w%, respectively. The input pump power is P_p = 100 mW and the input signal power is S_p = −50dBm.

A reference sensing system RSS is designed with the aim of obtaining feasible geometrical parameters maximizing the amplifier optical gain *g*. As described in chapter 3, PSO procedure can be applied to the design of amplifier [29]. For the sake of clarity, in this chapter, the PSO procedure employed for the design of a taper-coupled microsphere amplifier is indicated with the acronym DPSO (Designing PSO problem). It is worthwhile underline that DPSO procedure is not fundamental for the characterization procedure and then the design of the amplifier could be performed via a conventional parametric investigation.

The microsphere radius ρ_0, taper waist radius T_W, taper angle T_a, taper-microsphere gap *G* are optimized via DPSO. On the basis of preliminary simulations and of previous design experiences, the limits of the parameter ranges (solution space limits), are roughly fixed so that their optimized values and the corresponding maximum gain can be found within the fixed solution domain. In particular, the variation ranges are chosen by considering these technological needs:

i) a suitable microsphere radius in order to have resonance at both the pump and signal wavelengths;
ii) the waist radius larger than the inferior limit W_T = 0.5μm, since chalcogenide glass exhibits a number of drawbacks in the construction of taper having smaller waist;

iii) the waist radius smaller than the superior limit W_T = 1μm in order to have single-mode propagation;

iv) feasible taper angle and feasible taper–microsphere gap.

In this DPSO problem, the fitness function, which must be maximized, is defined in equation 3.4 and here reported:

$$F(\boldsymbol{p}_j) = 10\log g(\boldsymbol{p}_j) \tag{5.4}$$

where $g(\boldsymbol{p}_j)$ is the optical gain of the amplifier for particle $\boldsymbol{p}_j$. The optical gain is defined in equation 2.7.

The DPSO suitable maximum iteration number and the number of particles are fixed to I_{PSO} = 150 and N_B = 40. The space dimension is D = 4 and the position vector is $\boldsymbol{p}_j = \left[\rho_o^j, T_W^j, T_a{}^j, G^j\right]$, with $j = 1,2,...N_b$. The solution domain limits and the DPSO optimized values are summarized in Table 5.1.

Table 5.1 Solution domain limits and DPSO optimized values.

Parameters	Solution domain limits	DPSO optimized value
Microsphere radius ρ_o [μm]	10 – 30	**24.8**
Taper waist radius T_W [μm]	0.5 – 1	**1.0**
Taper – microsphere gap G [μm]	0.5 – 4	**0.5**
Taper angle T_a [rad]	0 – 0.04	**0.04**

It is apparent that taper radius T_W, taper-microsphere gap G and taper angle T_a reach the limit of search space. Therefore, a larger solution domain could allow larger optical gain g. But extending the solution domain space breaks two important hypotheses in the model. Too much small gap G does not allow to respect the assumption of weak coupling between microsphere and fiber. Moreover, taper radius T_W larger than 1μm makes fiber multimodal.

The data in Table 2.1 and 5.1 are used in the computer code based on theory of the previous chapters in order to obtain the RC_k values to be used in equation 5.1. These values should be measured in actual sensing set-ups.

Ten different resonating WGMs are simulated in the RSS. In Table 5.2, the main characteristics of these resonating modes are reported. The resonance wavelength λ_r, the modal parameters l, m and n, the optical gain g and the intrinsic quality factor Q for each WGM mode are listed.

Table 5.2. WGM Characteristics of RSS at Signal Wavelength λ_r

WGM resonance wavelength λ_r [nm]	$l = m$ parameter	n parameter	Optical gain g [dB]	Quality factor Q [$\cdot 10^7$]
2806	115	1	4.02	9.06
2783	116	1	5.66	9.10
2760	117	1	8.34	9.14
2809	108	2	2.19	8.75
2785	109	2	3.17	8.79
2762	110	2	4.76	8.84
2819	102	3	2.84	8.47
2795	103	3	3.65	8.52
2771	104	3	4.97	8.56
2747	105	3	4.44	8.61

In particular, the signal WGM maximizing the amplifier gain g has modal order $n = 1$; $l = m = 117$ at the wavelength $\lambda_s \approx 2760$ nm; the WGM at the pump wavelength has modal order $n = 1$, $l = m = 349$ at the wavelength $\lambda_p \approx 981$ nm. In Table 5.3 the main characteristics of the DPSO optimized amplifier, the signal and pump wavelengths, the refractive index of the microsphere and the taper fiber at resonance wavelength, the intrinsic signal lifetime τ_0 and the coupling signal lifetime τ_{ext} are reported. The refractive index of the microsphere and the fiber at signal wavelength are n_s^s and n_f^s respectively, the refractive index of the microsphere and fiber at pump wavelength are n_s^p and n_f^p respectively.

Table 5.3 Characteristics of the DPSO optimized amplifier

	Variable	Value
S I G N A L	Signal WGM mode	*n = 1 ; l = m = 117*
	Resonant wavelength λ_s	*2760nm*
	Refractive index n_{ms}^s and n_f^s	*2.2253*
	Intrinsic signal lifetime τ_0	0.134μs
	Coupling signal lifetime τ_{ext}	*0.294ns*
P U M P	Pump WGM mode	*n = 1 ; l = m = 349*
	Resonant wavelength λ_p	*981nm*
	Refractive index n_{ms}^p and n_f^p	*2.2751*
	Intrinsic signal lifetime τ_0	*0.074*μs
	Coupling signal lifetime τ_{ext}	*10.81*μs

5.4.2. Suitable choice of pump powers

The amplifier made of the optimized fiber taper coupled to microsphere amplifier is simulated for the signal power S_P = −50dBm. The reference characteristics RC_k (such as gains g_k) for CPSO problem are obtained using different values of input pump powers P_p. In order to reduce the time consumption of the simulation, it is necessary to choose conveniently the N_p input pump powers. Preliminary studies have been carried out on reference device RSS and then two pump power configurations demonstrated to be very promising, i.e. they allow CPSO to converge with a very small percent error $E_{\%}$. In the both cases, the number of input pump powers is N_p = 7 but two different pump schemes are used:

i) *Linearly spaced pump powers*: the N_p input pump powers are linearly spaced in the range P_p = [20 ÷ 140]mW;

ii) *Best fitting pump powers*: the N_p pump powers are arbitrarily chosen in order to have a better curve fitting of the optical gain in function of the input pump power P_p.

Table 5.4 reports the input pump power P_p and the calculated gain g_k for the both pump schemes. Figure 5.2 illustrates the optical gain g versus the input pump powers P_p. The dash line linearly interpolates the calculated g_k for linearly spaced pump scheme, the dot line linearly interpolates the calculated g_k for best fitting pump scheme and the full line linearly interpolates the optical gain g_k calculated with a very small step ΔP_p =0.5mW in order to have a reference of the behavior of the optical gain. The optical gain is calculated with input signal power S_p = -50dBm and both geometrical and spectroscopic parameters have nominal values reported in Table 2.1 and 5.1.

Table 5.4 Optical gain g_k obtained with S_p = −50 dBm

Linearly spaced pump powers P_p		Best fitting pump powers P_p	
Pump Power P_p [mW]	g_k [dB]	Pump Power P_p [mW]	g_k [dB]
20	0.28	70	1.03
40	0.56	85	1.36
60	0.86	95	1.70
80	1.24	99	2.03
100	7.01	99.5	7.01
120	7.04	110	7.02
140	7.06	130	7.05

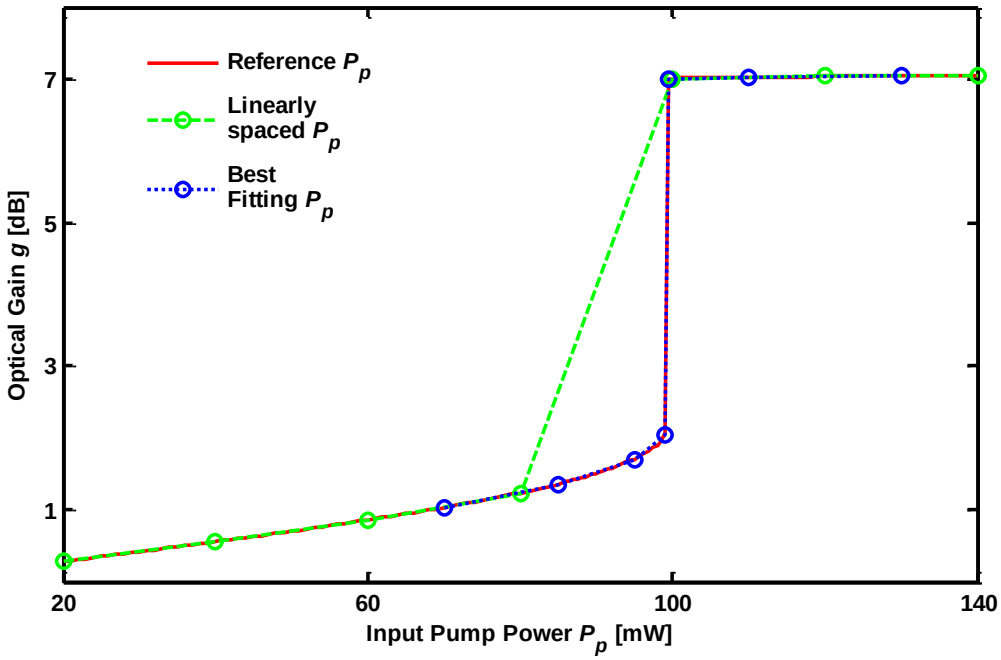

Fig. 5.2 DPSO optimized amplifier. Calculated optical gain g_k for linearly spaced pump powers (dashed line) and for best fitting pump powers (dot line). The full line is the reference optical gain obtained with a step ΔP_p=0.5mW. Input signal power is S_P=-50dBm.

The preliminary studies revealed that the percent errors $E_{\%}$ on the CPSO recovered values have the same order of magnitude with the two pump schemes. The computational time using the best fitting pump scheme is about two times more than that one using the linearly spaced pump scheme. A number of simulations reveal that a higher numbers of input pump powers allow negligible increasing of accuracy in recovering.

It is worthwhile to remark that the input pump powers listed in Table 5.4 are arbitrarily chosen. Lower pump powers can be used to avoid thermal effects. However they should be chosen around the cut-off pump power (for the device RSS it is about 99.25mW) to take into account that the depopulation rates non linearly depend on pump power.

For the previously mentioned reasons, in this work the linearly spaced pump powers reported in Table 5.4 are used.

5.4.3. Gain sensitivity to the fabrication tolerance

The sensitivity of the calculated optical gain g to the dimensions variation of the RSS is evaluated. The gain g is calculated as the ratio between the optical powers at the fiber ends, including the coupling/interaction with rare-earth microsphere, see equation 2.7.

Figure 5.3 reports the optical gain g as a function of the percent variation of the geometrical dimensions. For each curve, only the geometrical parameter specified in the legend is changed, while the others have the nominal values reported in Table 2.1 and 5.1. The red cross represents the RSS gain obtained by using nominal values for all the geometrical parameters. This reference optical gain is g = 7.06 dB, obtained with input pump power P_p=140 mW and input signal power S_p= -50 dBm.

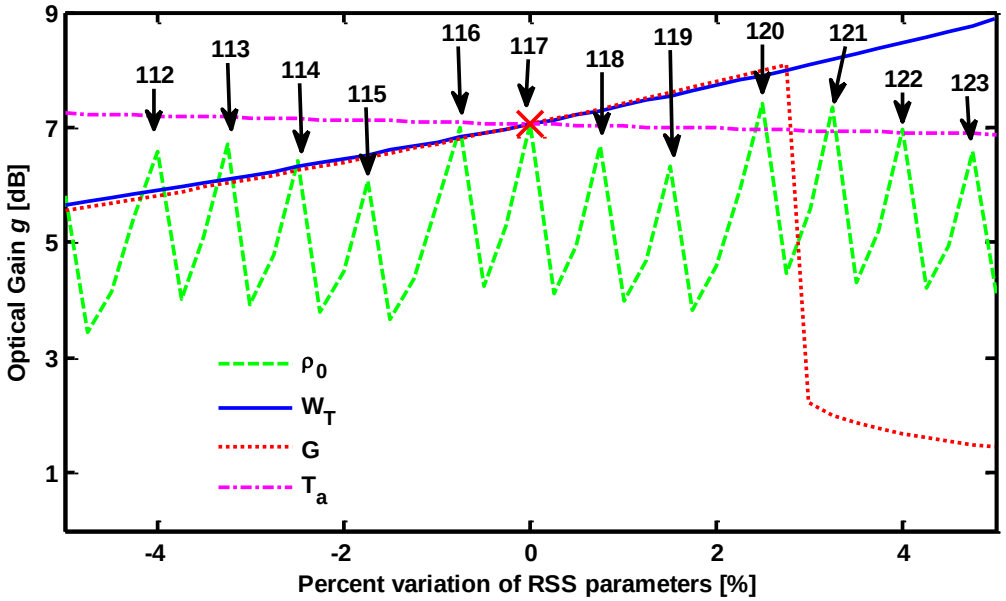

Fig. 5.3 Simulated optical gain g versus the RSS geometrical parameters. For each curve, only the parameter specified in the legend is varied, the other parameters have the nominal values of Tables 2.1 and 5.1. Input pump power P_P=140mW, input signal power is S_P=-50dBm.

In Figure 5.3, it is apparent that small percent variations of geometrical parameters strongly affect the calculated optical gain g. A variation of the microsphere radius ρ_0 (green dashed curve) causes the variation of the guided WGM. In Figure 5.3 for each resonating $WGM_{l,m,n}$ it is reported the value of parameter $m = l$ meanwhile the radial parameter is $n = 1$ for all the modes. Changes in the calculated gain g are caused by the variation of the waist radius T_W (blue full curve) or the gap G (red dotted curve) in the range [-5% ÷ 3%]. A decrease of the waist radius T_W causes an increase in the fiber evanescent field and therefore a strongest coupling between microsphere and fiber. A coupling increase can be also obtained by decreasing the gap G. If the gap G increases more than 3%, the optical gain drastically decreases because the coupling becomes too weak and the inversion of rare-earth ion population is not reached. The change of taper angle T_a (magenta dash-dotted curve) has a very slight effect on the calculated optical gain. In fact, a variation of taper angle ΔT_a = ±5%

causes a negligible change of the simulated optical gain, close to Δg = ±2.5%. In the actual case, the uncertainty on taper angle is of about ΔT_a = ±5%. Therefore, in this work the taper angle T_a is not considered in CPSO recovery. Fig. 5.3 demonstrates that the model can be sensitive to the variations of microsphere radius ρ_0, taper waist radius W_T and taper-microsphere gap G. This result is worthwhile since the fabrication tolerance is about 10% for all the aforesaid parameters.

Figure 5.4 reports the trend of optical gain g versus the linearly spaced input pump powers P_p (reported in Table 5.4) varying microsphere radius with steps of $\Delta\rho_0$ = 0.04μm (percent variation $\Delta\rho_{0\%}$=0.16% to nominal value). The input signal power S_P = -50dBm. It is interesting to note that, changing the geometrical dimensions, the trend of the optical gain versus input pump power P_p changes in two parts: i) the maximum optical gain; ii) the cut-off pump power.

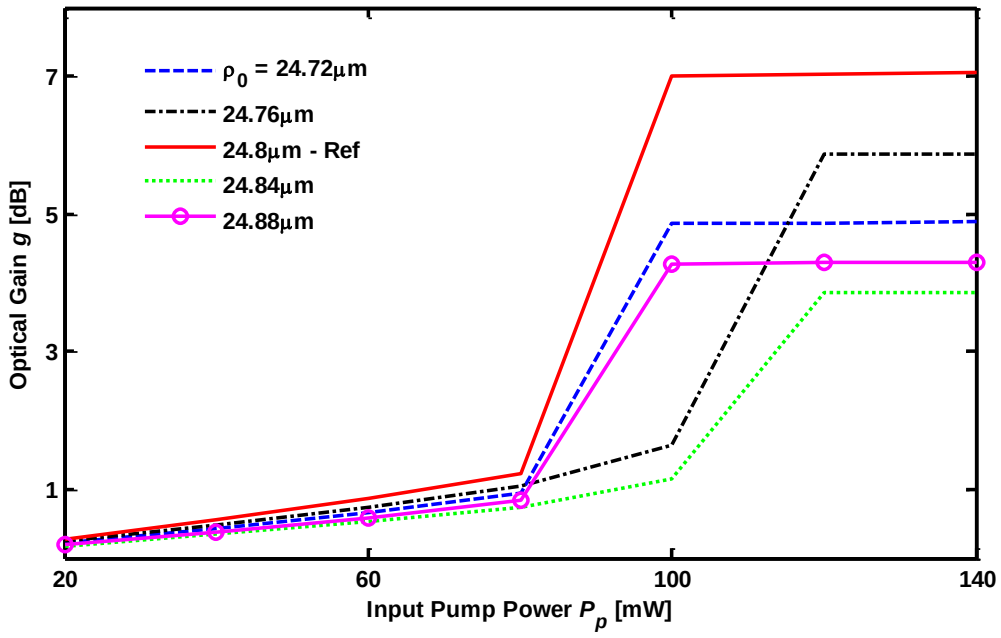

Fig. 5.4 DPSO optimized amplifier. Calculated g_k for linearly spaced pump powers varying microsphere radius ρ_0. The full line is obtained using the reference value ρ_0 = 24.8μm. Input signal power is S_P=-50dBm.

5.4.4. Gain sensitivity to rare-earth coefficients

In chapter 4, the following ions-ions interactions have been considered for erbium-doped glasses: the up-conversion C_{up} ($^4I_{13/2}$, $^4I_{13/2}$)→($^4I_{9/2}$, $^4I_{15/2}$), C_3 ($^4I_{11/2}$, $^4I_{11/2}$)→($^4F_{7/2}$, $^4I_{15/2}$) and C_{14} the cross-relaxation ($^4I_{15/2}$, $^4I_{9/2}$)→($^4I_{13/2}$, $^4I_{13/2}$). The characterization results reported in Table 4.5 showed that the standard deviation on recovered C_{14} values is much greater than that one obtained for C_{up} and C_3 (more than one order of magnitude). Therefore, on C_{14} recovered values there is a great dispersion. Other investigations on the gain sensitivity to the C_{14} parameter have been performed. Figure 5.5 reports the optical gain g as a function of the cross relaxation coefficient C_{14} for different input pump power P_p in the case of the device RSS.

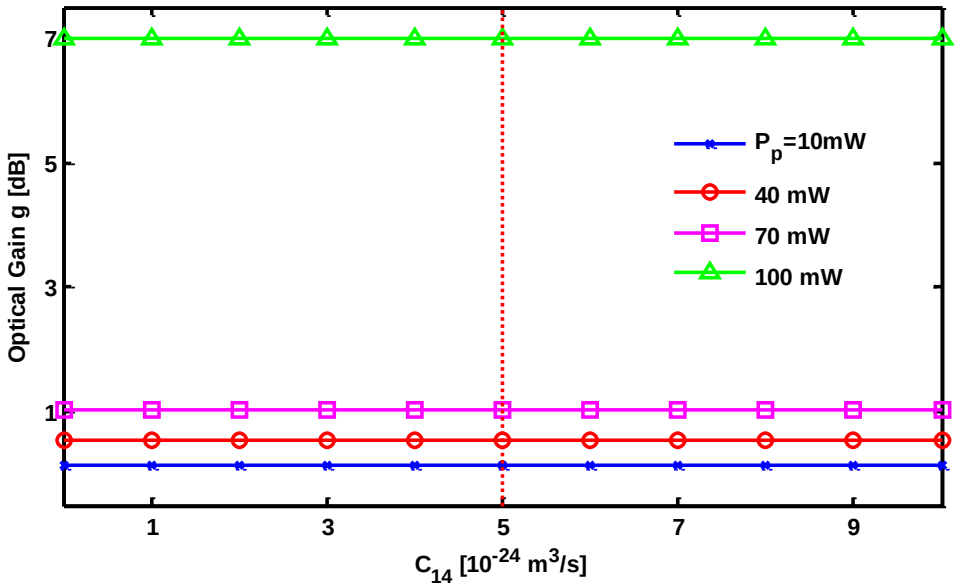

Fig. 5.5 Optical gain g varying C_{14} for the reference device RSS having dimensions reported in Table 5.1. Four different input pump powers are considered: 10mW, 40mW, 70mW and 100mW. Input signal power is S_P=-50dBm. The vertical dot line represents the nominal value C_{14}=5·10^{-24} m^3/s.

The vertical dot line represents the nominal value C_{14}=5·10^{-24} m^3/s. Figure 5.5 shows that the optical gain g is almost constant in the considered range, then the effect of C_{14} is negligible. In the worst case, when input pump power is P_p = 40mW, the percent variation on the optical gain between the case C_{14}=5·10^{-24} m^3/s (nominal value) and C_{14}=0 m^3/s is only Δg = 0.44%. Therefore, C_{14} parameter can be removed from the model.

The CPSO is also used to recover the values of ion lifetimes τ_2, τ_3, τ_4, for the transitions: $^4I_{13/2} \rightarrow {}^4I_{15/2}$, $^4I_{11/2} \rightarrow {}^4I_{15/2}$, $^4I_{9/2} \rightarrow {}^4I_{15/2}$, respectively [59]. Figure 5.6 shows the optical gain g as a function of τ_4 in the range [0.1ms ÷ 3ms] for different input pump power P_p in the case of the reference device RSS (dimensions reported in Table 5.1). For τ_4>0.81ms the gain sensitivity to τ_4 is very small.

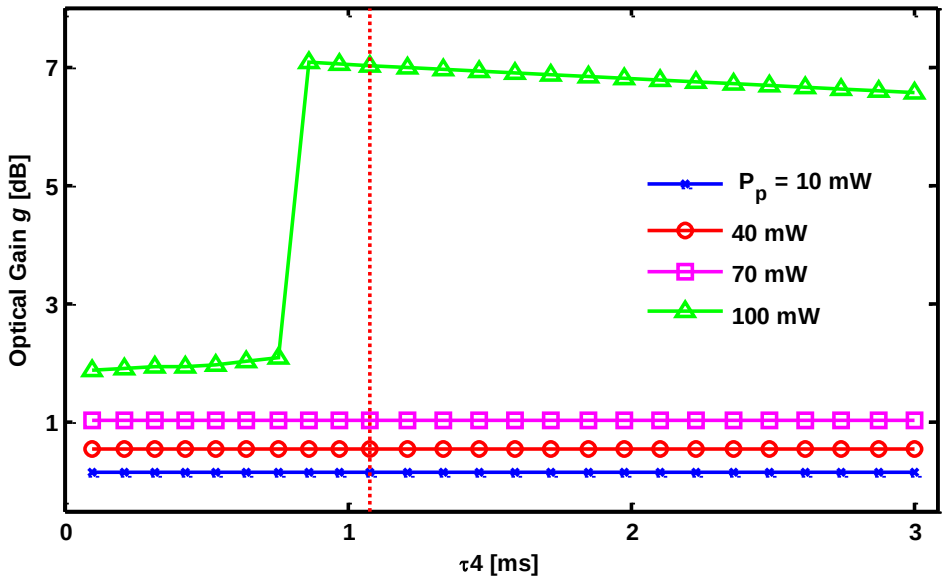

Fig. 5.6 Optical gain g varying τ_4 for the reference device RSS having dimensions reported in Table 5.1. Four different input pump powers are considered: 10mW, 40mW, 70mW and 100mW. Input signal power is S_P=-50dBm.The vertical dot line represents the nominal value τ_4= 1.08ms.

In the worst case, when input pump power is P_p = 100mW, the percent variation on the optical gain between the case τ_4=1.08*ms* (nominal value) and τ_4=3*ms* ($\Delta\tau_4$ = +178%) is only Δg = -6.2%. In particular, focusing on the range $\tau_4 \in$ [0.81ms ÷ 1.35ms] ($\Delta\tau_4$ = ±25%) the maximum variation of the optical gain is only Δg = 0.97%. So it is possible to conclude that with a very good approximation $\tau_4 \in$ [0.81ms ÷ 1.35ms] and it can be removed from the recovering process.

Therefore, these preliminary investigations on the RSS showed that the effect of the cross-relaxation parameter C_{14} ($^4I_{15/2}$, $^4I_{9/2}$) → ($^4I_{13/2}$, $^4I_{13/2}$) on the gain calculation is negligible. Similarly, the ion lifetime τ_4 related to the transition $^4I_{9/2} \rightarrow {}^4I_{15/2}$, varied in the range [0.8 ms ÷ 1.35 ms] does not induce considerable RSS gain changes. We can conclude that the recovery of C_{14} and τ_4 is not a CPSO goal.

Figure 5.7 reports the optical gain g as a function of the percent variation of the remaining rare-earth coefficients. For each curve, only the rare-earth coefficient specified in the legend is changed while the other parameters have the nominal values reported in Table 2.1 and 5.1. The red cross represents the RSS gain obtained by using nominal values for all the rare-earth parameters. The reference optical gain is g = 7.06 dB, obtained with input pump power P_p=140 mW and input signal power S_p= -50 dBm.

In Figure 5.7 it is apparent that the simulated gain g depends on the change of rare-earth coefficients. The gain variation due to the change of rare-earth coefficient C_{up} is slighter than that occurring for the other parameter fluctuations.

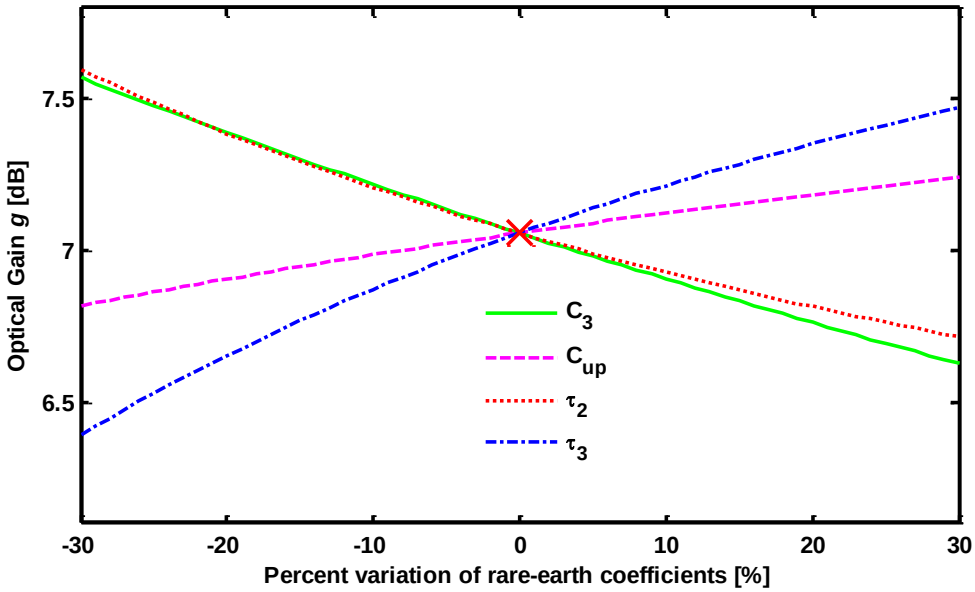

Fig. 5.7 Simulated optical gain g versus the rare earth coefficients. For each curve, only the coefficient specified in the legend is varied, the other parameters have the nominal values of Table 2.1 and 2.5. Input pump power is P_p=140 mW, input signal power is S_p= - 50dBm.

5.5. CPSO characterization

The previous study demonstrates that the model can be sensitive for variations of geometrical dimensions about 1% but the fabrication tolerance is about 10%. Therefore, it is important to take into account the uncertainty of geometrical parameters.

An approach to take into account the uncertainty of geometrical parameters is to use the single-step CPSO in order to recover the geometrical and the rare-earth parameters simultaneously. Therefore, the simulation reported in the following does not refer to the double-step CPSO; it is performed via a single CPSO. The nominal values in Table 2.1 and 5.1 represent the target values of CPSO procedure.

CPSO fitness function Φ_{SC}, to be minimized, is derived by equation 5.1. It is expressed as a function of the optical gain g_k of the amplifier:

$$\Phi_{SC}(\boldsymbol{p}_j) = \sum_{k=1}^{N_p} \left(g_k - g_k^j\right)^2$$
$$\text{with } j = 1,2,\ldots,N_b, \quad k = 1,2,\ldots,N_p \tag{5.5}$$

g_k is the optical gain of the RSS illustrated in Figure 5.2 and reported in Table 5.4 for linearly spaced power pump, g_k^j is the optical gain for the *j-th* particle of the swarm and the *k-th* pump power. In the actual case, after the set-up design and fabrication, the RSS optical gain g_k values can be easily measured.

In CPSO procedure, the cognitive parameter is c_1 = 1.494, the social parameter is c_2 = 1.494, the inertia weight I_w is a vector with I_{PSO} elements linearly spaced from 0.4 to 0.9. The reflecting walls boundary conditions are used, i.e. the particles that hit the boundary of solution space are reflected backward [34]. PSO algorithm is characterized by a very high convergence speed. In some cases, this can be a problem because the PSO could converge in a local minimum/maximum. In order to reduce convergence speed, a mutation operator is introduced. This operator modifies in a stochastic way the positions of the particles [34].

In order to test the method all the geometrical parameters are considered: the microsphere radius ρ_0, taper waist radius T_W, taper angle T_a, taper-microsphere gap G. The up-conversion coefficients C_{up} and C_3 are CPSO recovered. In this case, the dimension of the solution space is D = 6 and the vector position is $\boldsymbol{p}_j = \left[C_3^j, C_{up}^j, \rho_o^j, T_W^j, G^j, \alpha^j\right]$. The CPSO suitable maximum iteration number and the number of particles are fixed to

I_{PSO} = 60 and N_B = 48, respectively. In order to test the CPSO performance, the percent error $E_{\%}$ defined in equation 5.3 is calculated between the recovered and target values. Table 5.5 reports the target values, the solution domain ranges and the results of CPSO characterization. R_{PSO} = 3 is the number of performed CPSO launches. The solution domains are chosen in agreement with the uncertainty due to the fabrication processes.

Table 5.5 Results of characterization. Geometrical and rare-earth parameters are simultaneously recovered

	$C_3 \cdot 10^{-23}$ [m^3/s]	$C_{up} \cdot 10^{-23}$ [m^3/s]	ρ_0 [μm]	W_T [μm]	G [μm]	α [rad]
Target Value	2	3	24.8	1	0.5	0.04
Solution Domain Ranges	1 ÷ 3	2 ÷ 4	24.7 ÷ 24.9	0.9 ÷ 1.1	0.4 ÷ 0.6	0.03 ÷ 0.05
	Execution 1 : Global Best Fitness $\Phi_{SC}(\boldsymbol{p}^{GB}) = 4.1 \cdot 10^{-4}$					
Best Position	1.703	2.177	24.779	1.022	0.500	0.041
Percent Error	-14.9%	- 27.4%	-0.09%	2.2%	0.06%	1.8%
	Execution 2 : Global Best Fitness $\Phi_{SC}(\boldsymbol{p}^{GB}) = 4.6 \cdot 10^{-3}$					
Best Position	2.507	3.160	24.785	1.054	0.499	0.049
Percent Error	25.4%	5.3%	-0.06%	5.4%	-0.04%	21.8%
	Execution 3 : Global Best Fitness $\Phi_{SC}(\boldsymbol{p}^{GB}) = 5.1 \cdot 10^{-3}$					
Best Position	2.63	3.42	24.79	1.048	0.492	0.043
Percent Error	31.5%	13.9%	-0.04%	4.8%	-1.6%	7.6%

The results concerning the geometrical parameters are in good agreement with the target values except for the taper angle T_a (maximum error is $E_{\%}$ = 21.8%). On the contrary, the recovered rare-earth parameters C_3 and C_{up} exhibit large errors and scattered values.

It is interesting to note that in each execution the global best fitness $\Phi_{SC}\left(\boldsymbol{p}^{GB}\right)$ is very small: i.e. the recovered optical gains g_k in the global best position $\boldsymbol{p}^{GB}$ are very close to the reference ones reported in Table 5.4. Therefore the CPSO obtained amplifier models have performance very close to the device RSS. In other words the CPSO finds a set of unknown parameters that gives the same performance of reference device RSS but the error on rare-earth parameters is not satisfactory.

Similarly it is possible to demonstrate that the error for the ion lifetimes τ_2 and τ_3 recovering is $E_{\%} \approx 50\%$.

The single CPSO does not allow an accurate geometrical and spectroscopic parameter recovery. In fact, the strong non-linearities in rare-earth behavior and the high parameters number to be simultaneously recovered makes the algorithm convergence critical. Moreover, the computational cost increases exponentially. However, the method suggested in the previous chapter is not completely reliable if the geometry uncertainty is realistically considered.

5.6. Double-step CPSO: geometrical characterization

The alternative approach is here illustrated. The problem is solved in two subsequent steps: i) geometrical characterization G) and ii) rare-earth spectroscopic characterization S). In G) the recovered parameters are the microsphere radius ρ_0, taper waist radius W_T and taper-microsphere gap G. In order to neglect the rare-earth / light interaction, the pump at $\lambda_p \approx 981$ nm is not considered (it is set equal to zero). Without optical pump power, the erbium level $^4I_{11/2}$ is depopulated and there is not optical gain (see chapter 2).

In the geometrical characterization, the fitness function $\Phi_{GC}(\boldsymbol{p}_j)$ is given by equation 5.6. It is derived by equation 5.1:

$$\Phi_{GC}(\boldsymbol{p}_j) = \left(S_p^{out} - S_{p,CPSO}^{out,j}\right)^2 \quad \text{with } j = 1,2,\ldots,N_b \tag{5.6}$$

S_p^{out} is the RSS output signal power versus the wavelength. Input signal power S_p = 100 mW and the other parameters are listed in Table 2.1 and 5.1. $S_{p,CPSO}^{out,j}$ is the output signal power simulated for the j-th particle.

The RSS output signal power S_p^{out} versus the wavelength is depicted in Figure 5.8, it is used in the fitness function $\Phi_{GC}(\boldsymbol{p}_j)$ calculation. The ten dips in Figure 5.8 refer to the ten WGM resonances listed in Table 5.2. The modal order $l = m$, n is reported for all the dips. The dashed RSS output signal power corresponds to WGM having modal order $l = m = 117$, $n = 1$, which allows the highest amplification in active behavior (it will be considered in the next section).

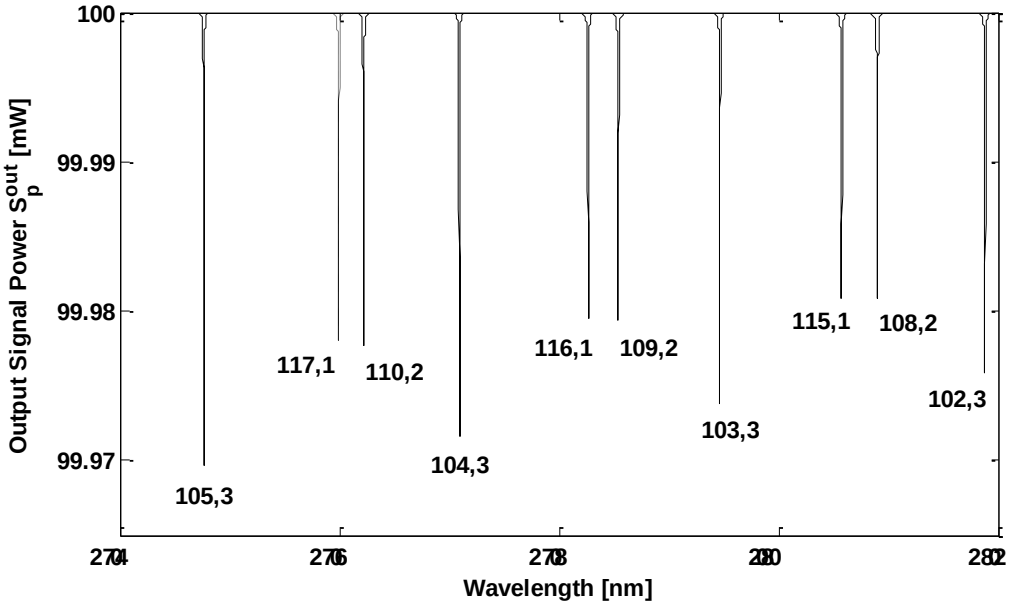

Fig. 5.8 RSS output signal power S_p^{out} versus the wavelength. Input signal power is $S_p = 100$ mW.

In the case of geometrical characterization, the CPSO suitable maximum iteration number is I_{PSO} = 50 and the number of particles is N_b = 50. The space dimension is D = 3 and the position vector is $\boldsymbol{p}_j = \left[\rho_o^j, T_W^j, G^j\right]$, with $j = 1,2,\ldots,N_b$. For each parameter, the solution domain is chosen in agreement with the fabrication process tolerance (about 10%). R_{CPSO} = 20 CPSO executions are performed. The weighted mean WM_{GBP} is calculated via equation 5.2, by choosing, among the 20 executions, the five global best positions $\boldsymbol{p}^{GB} = \left[\rho_o^{GB}, T_W^{GB}, G^{GB}\right]$ with lower global best fitness. Table 5.6 reports the RSS target values, the solution domains, the CPSO recovered weighted mean WM_{GBP} values, the percent error $E_{\%}$ and the CPSO standard deviation SD for each parameter.

Table 5.6 Results of geometrical G) Characterization

Variable	ρ_0 [μm]	W_T [μm]	G [μm]
Target Value	24.8	1	0.5
Solution Domain Ranges	24.7 ÷ 24.9	0.9 ÷ 1.1	0.4 ÷ 0.6
WM_{GBP}	24.8	0.9997	0.5002
SD	$1.7 \cdot 10^{-7}$	$9.9 \cdot 10^{-4}$	$4.1 \cdot 10^{-4}$
Percent Error $E_{\%}$	0%	-0.03%	0.03%

The recovered values are in excellent agreement with the target values. The reason is apparent: the microsphere radius ρ_0 is strictly related to the resonant wavelengths λ_s where the dips of figure 5.8 occur. CPSO can recover the microsphere radius with a negligible error close to $E_{\%} = 1 \times 10^{-8}$, so the three-dimensional solution space (D=3) becomes very close to a bi-dimensional (D=2) one, making easier the problem solution.

It is worthwhile to note that the percent error $E_{\%}$ on the recovered taper radius T_W and gap G have similar absolute value but opposite sign. This behavior is observed not only for the weighted mean WM_{GBP}, but also in each CPSO execution and agrees with Figure 5.3. The reason is apparent: a decrease of the waist radius T_W causes an increase in the fiber evanescent field and therefore a strongest coupling between microsphere and fiber. A similar coupling increase can be also obtained by decreasing the gap G.

In the next section, the recovered geometry is used in order to perform the rare-earth characterization.

5.7. Double-step CPSO: rare-earth characterization

In the second step, the optical pump power is used in order to activate the interaction between light and rare-earth ions and simulate the amplifier gain g_k. This allows the spectroscopic characterization, the geometrical parameters being identified in the previous section. Three different cases are simulated:

- *S) CPSO – I case* : the up-conversion coefficients C_{up} and C_3 and the lifetimes τ_2 and τ_3 are the unknown parameters.
- *S) CPSO – II case* : the branching ratio β_{32} ($^4I_{11/2} \rightarrow {}^4I_{13/2}$) and the up-conversion coefficients C_{up} and C_3 are the unknown parameters.
- S*) CPSO – III case* : the branching ratio β_{32} and the ion lifetimes τ_2 and τ_3 are the unknown parameters.

Very large solution domains are taken into account in order to test the method robustness. Typical measurement uncertainty on lifetimes is about 5-10% (using Judd-Ofelt theory), about 30% on up-conversion coefficient C_{up} and about 20% on C_3 (estimated by fitting the simulated decay curves to the measured ones [60]).

In S) CPSO problem, the fitness function Φ_{SC}, which must be minimized, is defined in equation 5.5. The considered input pump powers are the linearly spaced reported in Table 5.4.

After a preliminary investigation, in *S) CPSO – I case* the CPSO suitable maximum iteration number and the number of particles are I_{PSO} = 50 and N_b = 40 respectively. The space dimension is D = 4 and the position

vector is $\boldsymbol{p}_j = \left[{C_{up}}^j, {C_3}^j, {\tau_2}^j, {\tau_3}^j \right]$, with $j = 1,2,\ldots,N_b$. R_{CPSO} = 10 different CPSO executions are performed.

Table 5.7 reports the solution domain, the recovered weighted mean WM_{GBP}, the percent error $E_{\%}$ and the CPSO standard deviation SD for each parameter, S) CPSO – I case. The high C_{up} dispersion, i.e. the large standard deviation, is originated, as expected in Figure 5.7, from the low RSS sensitivity to this parameter change. The WM_{GBP} calculation allows the recovery of C_{up} parameter very close to the target one in spite of the large dispersion.

The target values and the related CPSO recovered WM_{GBP} are very close. Each of these errors is extremely low and much smaller than the usual measurement uncertainty. In other words, these errors are much smaller than those performed with actual high cost measurement systems. This S) CPSO I-case application shows that, even if i) the search domain is large, ii) the up-conversion coefficients C_{up} and C_3 are not easily measurable, the followed approach allows a very robust characterization. The computation time is about 6 days with an Intel Xeon E5-2620 CPU.

Table 5.7 Results of Spectroscopic Characterization, *S) CPSO – I case*

Variable	C_3 [$\cdot 10^{-23}$ m^3/s]	C_{up} [$\cdot 10^{-23}$ m^3/s]	τ_2 [ms]	τ_3 [ms]
Target Value	2	3	1.83	1.37
Solution Domain Ranges	1 ÷ 3	2 ÷ 4	0.1÷3	0.1÷3
WM_{GBP}	2.01	3.16	1.89	1.38
SD	0.04	0.47	0.15	0.02
Percent Error $E_{\%}$	0.64%	5.49%	3.39%	0.52%

Figure 5.9 shows the global best positions in the C_3-C_{up} and τ_2- τ_3 solution domains for the ten CPSO executions (dots), the target values (red crosses) and the weighted mean WM_{GBP} (green full circles) calculated using Equation 5.2 and reported in Table 5.7. In the inset figure, a very narrow range is used.

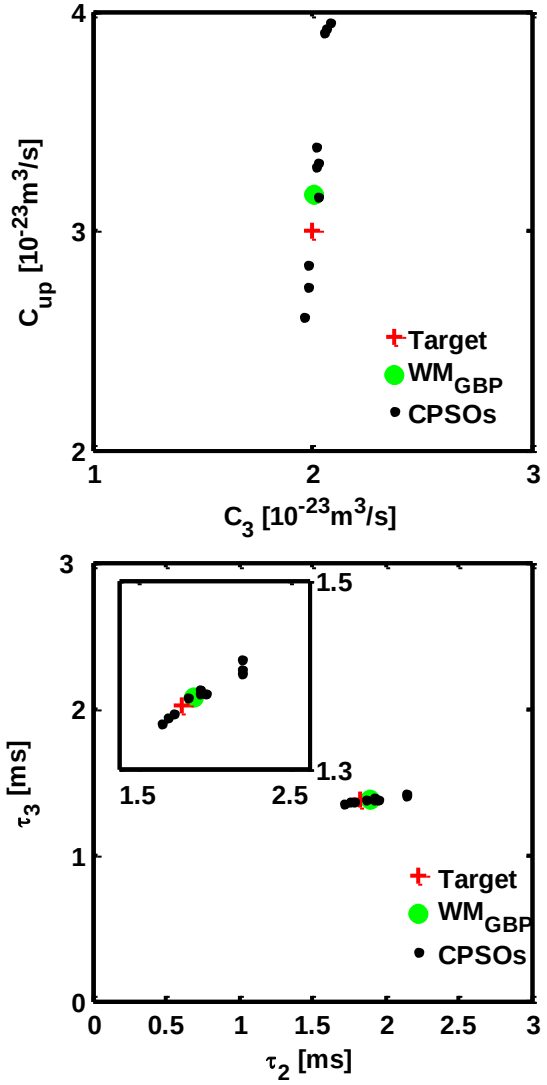

Fig. 5.9 *S) CPSO – I case* : position in C_3-C_{up} and τ_2-τ_3 solution domains of the global best positions (dots) recovered via the R_{CPSO} = 10 CPSO executions, the target values (red crosses) and the weighted means WM_{GBP} reported in Table 5.7 (green full circles).

In *S) CPSO-II ca*se, the branching ratio β_{32} ($^4I_{11/2} \rightarrow {}^4I_{13/2}$) and the up-conversion coefficients C_{up} and C_3 are recovered. For the branching ratio β_{32}, a typical measurement uncertainty is close to 30%. In these S) CPSO case, the fitness function, which must be minimized, is defined in equation 5.5. The input pump powers used are the linearly spaced reported in Table 5.4. The CPSO suitable maximum iteration number and the number of particles are I_{PSO} = 50 and N_b = 40, respectively. The space dimension for the both cases is D = 3 and the position vectors is $\boldsymbol{p}_j = \left[C_{up}{}^j, C_3{}^j, \beta_{32}{}^j\right]$, with $j = 1,2,\ldots,N_b$. In order to minimize the error made on the single parameter, equation 5.2 is employed for evaluating the weighted mean WM_{GBP}.

Table 5.8 reports the solution domain, the recovered weighted mean WM_{GBP}, the percent error $E_{\%}$ and the CPSO standard deviation SD obtained via R_{CPSO} = 10 executions. Table 5.8 shows that, in the worst case, the largest error $E_{\%}$ = 0.75% is made on C_{up} parameter recovery. The computation time in each case is about 6 days with an Intel Xeon E5-2620 CPU.

Table 5.8 Spectroscopic Characterization, *S) CPSO – II case*

Variable	C_3 [$\cdot 10^{-23}\ m^3/s$]	C_{up} [$\cdot 10^{-23}\ m^3/s$]	β_{32} [%]
Target Value	2	3	13.72
Solution Domain Ranges	1 ÷ 3	2 ÷ 4	11 ÷ 17
WM_{GBP}	2	3.02	13.78
SD	0.002	0.257	0.49
Percent Error $E_{\%}$	0.05%	0.75%	0.42%

In *S) CPSO-III case*, the branching ratio β_{32} and the ion lifetimes τ_2 and τ_3 are recovered. In these S) CPSO case, the fitness function, which must be minimized, is defined in equation 5.5. The input pump powers used are the linearly spaced reported in Table 5.4. The CPSO suitable maximum iteration number and the number of particles are I_{PSO} = 50 and N_b = 40, respectively. The space dimension for the both cases is D = 3 and the position vectors is $\boldsymbol{p}_j = \left[\tau_2{}^j, \tau_3{}^j, \beta_{32}{}^j\right]$, with $j = 1,2,\ldots,N_b$. In order to minimize the error made on the single parameter, equation 5.2 is employed for evaluating the weighted mean WM_{GBP}.

Table 5.9 report the solution domain, the recovered weighted mean WM_{GBP}, the percent error $E_{\%}$ and the CPSO standard deviation SD obtained via R_{CPSO} = 10 executions. Table 5.9 shows that, in the worst case, the largest error $E_{\%}$=1.35% is made on τ_2 parameter recovery. The computation time is about 6 days with an Intel Xeon E5-2620 CPU.

Table 5.9. Spectroscopic Characterization, *S) CPSO – III case*

Variable	τ_2 [ms]	τ_3 [ms]	β_{32} [%]
Target Value	1.83	1.37	13.72
Solution Domain Ranges	0.1 ÷ 3	0.1 ÷ 3	11 ÷ 17
WM_{GBP}	1.855	1.369	13.598
SD	0.18	0.002	0.96
Percent Error $E_{\%}$	1.35%	-0.03%	-0.89%

Figure 5.10 reports the fitness function Φ_c as defined in equation 5.5, in logarithmic scale, versus τ_2, τ_3 and β_{32} for the global best positions $\boldsymbol{p}^{GB}$ recovered via the R_{PSO} = 10 executions in *S) CPSO-III case*. The vertical line represents the target value in each dimension. The global best position with the smallest fitness (about $\Phi_c = 5.4 \cdot 10^{-8}$) corresponds to the best solution among the R_{PSO} = 10 executions. In this case, the best global solution is defined by the particle position closer to the target (lying on the vertical line) in the three dimensions space. For this particle, the percent error on lifetimes τ_2 and τ_3 and on branching ratio β_{32} are respectively $E_{\%}$ = 0.78%, $E_{\%}$ = -0.03% and $E_{\%}$ = -0.54%. In other cases, the minimum of the fitness could occur for particle with recovered parameters slightly more distant from the target ones, as expected in a global search approach.

The S) CPSO I, II and III cases demonstrate that the proposed approach provide to recover different spectroscopic parameters with errors lower than the typical measurement uncertainties. Moreover, this approach is a solution to avoid the use of expensive measurement instruments since it requires a simple optical detector and a personal computer.

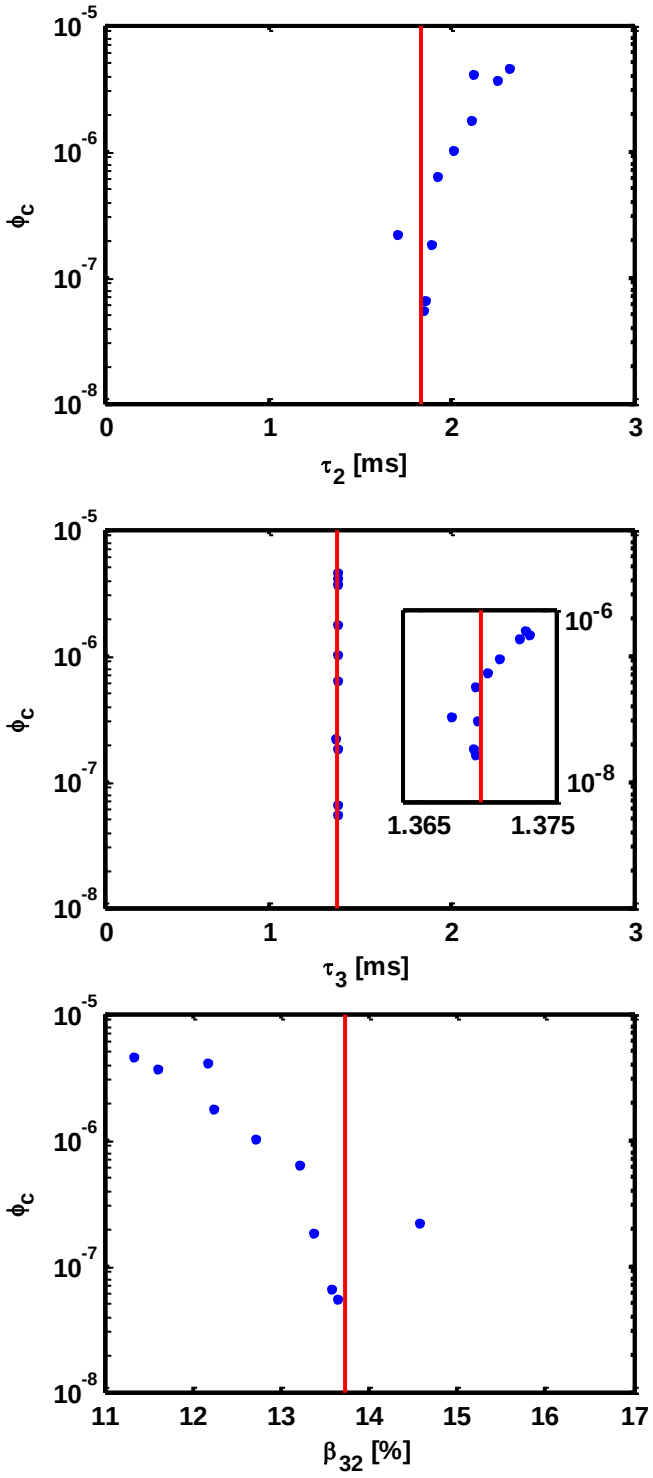

Fig. 5.10 *S) CPSO – III case* : Fitness function Φ_c (in logarithmic scale) versus τ_2, τ_3 and β_{32} for the global best positions $\boldsymbol{p}^{GB}$ recovered by all the R_{CPSO} = 10 executions. The vertical line represents the target position in each dimension.

5.8. Summary

WGM resonance and CPSO approach constitute a solution for complete and robust rare-earth characterization. The procedure, in order to mitigate the effect of uncertainty on geometrical dimensions, follows two steps. In the first one, the geometrical characterization is performed. In the second step, the spectroscopic parameters are recovered. The largest error in geometrical characterization is on the gap between microsphere and taper fiber and it is 0.03%. The developed characterization tool recovers the spectroscopic parameters with an error less than that provided by high-cost measurement instruments. The errors made on the up-conversion coefficients C_{up} and C_3 and the branching ratio β_{32} are 0.75%, 0.05% and 0.42%, respectively. The method can be applied to other rare-earths as an alternative procedure to the use of very expensive instruments. Moreover, the same approach could be applied to other sensing systems. For example, the model of the medium surrounding a passive microsphere or of a microbubble containing a polluted solution or a biological fluid could be considered. In this case, the parameters to be recovered could be those related to the analyte concentration via transmittance measurement instead of resonance wavelength-shift via optical spectrum analyzer.

Chapter 6

Design of microspheres and microbubbles for environmental and biological monitoring[4]

6.1. Introduction

In this chapter it is described an exhaustive model for designing a novel microsphere and microbubble sensing set-ups. The considered system is constituted by a pair of identical LPGs with a fiber taper in between. The microsphere and microbubble resonators are coupled via the tapered fiber. The pair of identical LPGs allow multiple selective coupling and interrogation of several micro-resonators by using the same optical link. The computer code is validated via the comparison of the simulation with the experiment. A good agreement between experimental and simulated results is found. The computer code can be used to design novel set-ups for sensing at different wavelengths and for different chemical/biological contaminants.

[4] Work presented in this chapter has been submitted to *IEEE International Instrumentation and Measurement Technology Conference (2017)*: M. C. Falconi, G. Palma, A. Ameruoso, C. Laterza, S. Popolizio, L. Rinaldi, A. Rizzi, G. Testa, F. Tragni, F. Chiavaioli, F. Baldini, D. Farnesi, G. Nunzi Conti, S. Pelli, G. C. Righini, S. Soria, C. Trono, F. Prudenzano, "Design of Microspheres and Microbubbles for Environmental Chemical/Biological Optical Sensing".

6.2. Sensing via microsphere and microbubble

Microspheres and microbubbles are example of whispering gallery mode (WGM) resonators. These structures allow confinement of light for long time in very small volumes. This increases the interaction between the WGM evanescent electromagnetic field and the external environment in case of microspheres or internal environment in case of microbubbles. Slight changes in resonator size and/or refractive index at the cavity-environment interface induce changes in the resonator Q-factor and/or shifts in the resonance wavelength.

WGM resonators are largely employed for efficient sensing of temperature [76-81], refractive index [82], force [83], pressure [84], biomolecules [85] and spectroscopic parameters [59]. They can be doped with rare-earths in order to obtain light sources as described in the previous chapters. These suitable integrated light sources can be used to provide the evanescent electromagnetic field that interacts with the analyte [1, 59, 79, 81].

An all-in-fiber coupling system for quasi-distributed and wavelength selective addressing by using the same optical link is proposed in [86]. In this chapter two kinds of setup for chemical/biological sensing, similar to those reported in [86], are modeled. In the first one the polluted fluid surrounds a microsphere, in the second one the polluted fluid is within a microbubble. A model for the simulation of both microsphere and microbubble resonators, coupled to a tapered fiber, is developed. The taper fiber is between two identical LPGs. The first LPG allows the coupling between the fiber fundamental core mode and a peculiar cladding mode. The evanescent field of this cladding

mode is used to excite the WGMs in the resonator. The light out-coupling the resonator comes back from the cladding mode into the fiber fundamental core mode through the second LPG. The pair of identical LPGs can operate in different wavelength bands. This allows multiple selective coupling of spatially quasi-distributed micro-resonators.

The model is well validated on the experiment reported in [86] and, to the best of our knowledge, it is the first one for this kind of microsphere/microbubble set-ups.

6.3. Theory

The modelled sensing system is constituted by a micro-resonator coupled to a tapered fiber. The fiber has two identical LPGs on both sides. The system is reported in Figure 6.1. WGM resonator can be a microsphere or a microbubble. The two set-ups are shown in Figure 6.2. The distance between the microsphere / microbubble and the taper fiber is the so-called gap G.

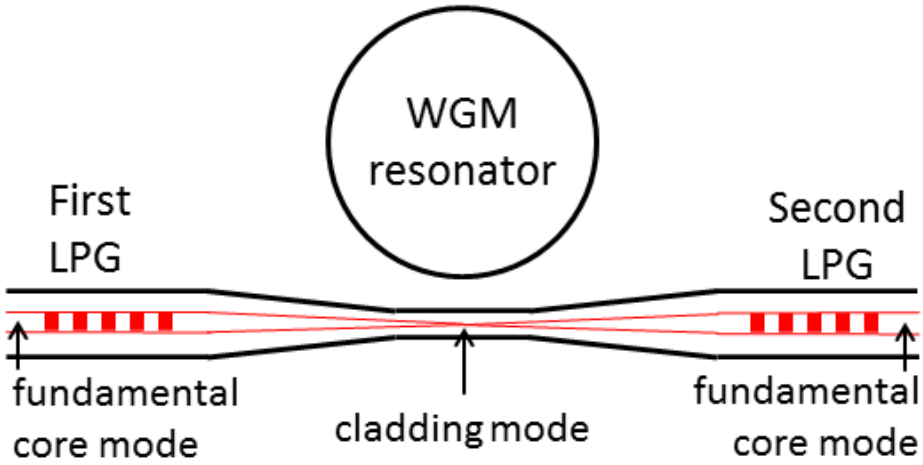

Fig. 6.1 The modelled sensing system is constituted by a microresonator coupled to a tapered fiber. Two identical LPGs on both sides of the tapered fiber allow optical coupling and interrogation of microresonator.

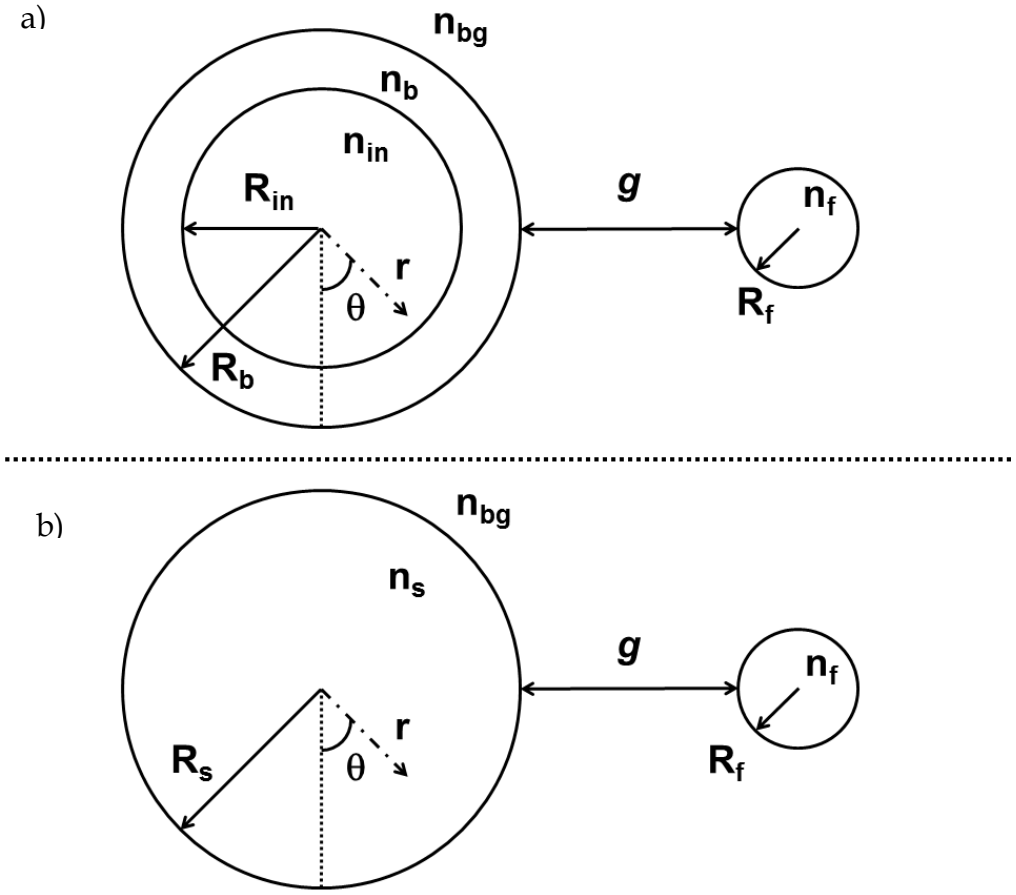

Fig. 6.2 Tapered fiber coupled to a) microbubble and b) microsphere.

The model works in two subsequent steps:

i) solving the Maxwell equations in order to obtain the electromagnetic field distribution of both resonator and fiber;

ii) applying the coupled mode theory in order to calculate the coupling strength between the resonator and the fiber.

6.3.1. Analytical model of a microsphere

In a fiber the electromagnetic field distribution has well-known analytical solutions [6, 15]. In a WGM resonator it can be described using the whispering gallery mode formalism. The WGM formalism is well-described in chapter 1 and here it is briefly reported in order to compare microsphere and microbubble solutions.

The Helmholtz equation in spherical coordinates reported in 1.2, is repeated in equation 6.1:

$$\nabla^2\psi(r,\theta,\phi) = -k^2 n_s \psi(r,\theta,\phi) \tag{6.1}$$

where $k = \omega\sqrt{\mu_0\varepsilon_0}$ is the wave vector in vacuum; n_s is the refractive index of the microsphere; $\psi(r,\theta,\phi) = E_\theta$, for the transverse electric (TE) modes, $\psi(r,\theta,\phi) = H_\theta$, for the transverse magnetic (TM) modes.

Applying the separation of the variables in spherical coordinates:

$$\psi(r,\theta,\phi) = N_s \psi_r(r)\psi_\theta(\theta)\psi_\phi(\phi) \tag{6.2}$$

where N_S is a normalization constant that is obtained by imposing equal to unity the volume integral of ψ^2 over all the space divided by $2\pi R_s$ [6]. R_s is the microsphere radius.

The approximation $\theta << 1$ for the polar angle is considered because the predominant WGMs are those coupled via the tapered fiber close to the equatorial plane. The Helmholtz equation 6.1 is solved using the separation of variables reported in 6.2 [6]. The solutions are illustrated in equation 6.3.

$$\psi_\phi(\phi) = e^{\pm jm\phi}$$

$$\psi_\theta(\theta) = e^{-\frac{m}{2}\theta^2} H_N\left(\sqrt{m}\theta\right), \quad m >> 1 >> \theta \tag{6.3}$$

$$\psi_r(r) = \begin{cases} Aj_l(kn_s r), & r \le R_s \\ Be^{-\alpha_s(r-R_s)}, & r > R_s \end{cases}$$

m is the azimuthal parameter and represents the number of field maxima along the azimuthal dimension; H_N is the Hermite polynomial of order $N = l - m$; l is the polar parameter and $l-m+1$ is the number of field maxima in the polar direction $\hat{\theta}$; j_l is the spherical Bessel function of the first kind of order l; A and B are unknown parameters that are obtained by imposing the boundary conditions. α_s is the exponential decay coefficient in the background and it is expressed by equation 6.4:

$$\alpha_s = \sqrt{\beta_l^2 - k^2 n_{bg}^2} \quad \beta_l = \sqrt{l(l+1)}/R_s \tag{6.4}$$

β_l is the propagation constant parallel to the surface of the microsphere, n_{bg} is the refractive index of the background.

The number n of field maxima along the radial direction within the microsphere radius R_s is called radial parameter.

Each $WGM_{l,m,n}$ mode is characterized by the three integers l, m, n.

Matching the tangential components of electric and magnetic fields at the interface between sphere and background leads to the characteristic equation.

For ***TE modes,*** the electric field components are: $E_\theta = \psi(r,\theta,\phi)$ and $E_\phi = E_r = 0$. The magnetic field is obtained using Maxwell equations with the condition $\frac{\partial E_\theta}{\partial r} >> \frac{1}{r} E_\theta$:

$$\overline{H} = \frac{j}{\omega\mu_0}\frac{\partial E_\theta}{\partial r}\hat{\phi} \pm \frac{m}{\omega\mu_0 r\cos\theta} E_\theta \hat{r} \tag{6.5}$$

Imposing the boundary conditions for E_θ and H_ϕ in $r = R_s$ leads to the system 6.6:

$$\begin{cases} Aj_l(kn_sR_s) = B \\ Akn_s j_l'(kn_sR_s) = -\alpha_s B \end{cases} \tag{6.6}$$

For ***TM modes,*** the magnetic field components are: $H_\theta = \psi(r,\theta,\phi)$ and $H_\phi = H_r = 0$. The electric field is obtained using Maxwell equations with the condition $\frac{\partial H_\theta}{\partial r} >> \frac{1}{r} H_\theta$ [6]:

$$\overline{E} = -\frac{j}{\omega\varepsilon_0 n_s^2}\frac{\partial H_\theta}{\partial r}\hat{\phi} \mp \frac{m}{\omega\varepsilon_0 n_s^2 r\cos\theta} H_\theta \hat{r} \tag{6.7}$$

Imposing the boundary conditions for H_θ and E_ϕ in $r = R_s$ [6] leads to the system 6.8:

$$\begin{cases} Aj_l(kn_sR_s) = B \\ A\frac{k}{n_s} j_l'(kn_sR_s) = -\frac{\alpha_s}{n_0^2} B \end{cases} \tag{6.8}$$

The characteristic equation 6.9 is obtained by calculating the determinant of 6.6 and 6.8:

$$\left(\frac{l}{R_s} + \chi\alpha_s\right) j_l(kn_sR_s) = kn_s j_{l+1}(kn_sR_s) \tag{6.9}$$

Where $\chi = 1$ for TE modes and $\chi = n_s^2/n_{bg}^2$ for TM modes.

Using the characteristic equation is possible to obtain the resonance wavelengths and then the WGM field distributions.

6.3.2. Analytical model of a microbubble

A microbubble is a circular resonator constituted by two parts:

i) the inner volume having radius R_{in}. It contains a solution with the analyte to detect.

ii) the glass shell having radius R_b. It has supporting and protective function.

The analytical solution of the electromagnetic field in a microbubble follows by applying the same procedure of the previous section. The radial component $\psi_r(r)$ of equation 6.3 has to be updated:

$$R_r(r) = \begin{cases} A_0 j_l(kn_{in}r), & r \le R_{in} \\ A_1 j_l(kn_b r) + A_2 y_l(kn_b r), & R_{in} < r \le R_b \\ A_3 e^{-\alpha_s (r-R_b)}, & r > R_b \end{cases} \tag{6.10}$$

y_l is the spherical Bessel function of the second kind of order *l*.

For ***TE modes*** the boundary conditions have to be applied on E_θ and H_ϕ in $r = R_{in}$ and $r = R_b$. Applying the boundary conditions in $r = R_{in}$ leads to the following equations 6.11:

$$\begin{aligned} A_0 j_l(kn_{in}R_{in}) &= A_1 j_l(kn_b R_{in}) + A_2 y_l(kn_b R_{in}) \\ A_0 kn_{in} j_l'(kn_{in}R_{in}) &= A_1 j_l'(kn_b R_{in}) kn_b + A_2 y_l'(kn_b R_{in}) kn_b \end{aligned} \tag{6.11}$$

Applying the boundary conditions H_ϕ in $r = R_b$ leads to the following equations 6.12:

$$\begin{cases} A_1 j_l(kn_b R_b) + A_2 y_l(kn_b R_b) = A_3 \\ A_1 j_l'(kn_b R_b) kn_b + A_2 y_l'(kn_b R_b) kn_b = -A_3 \alpha_s \end{cases} \quad (6.12)$$

From 6.11 and 6.12 it is possible to obtain the coefficients matrix reported in equation 6.13:

$$\begin{bmatrix} j_l(kn_{in} R_{in}) & -j_l(kn_b R_{in}) & -y_l(kn_b R_{in}) & 0 \\ kn_{in} j_l'(kn_{in} R_{in}) & -j_l'(kn_b R_{in}) kn_b & -y_l'(kn_b R_{in}) kn_b & 0 \\ 0 & j_l(kn_b R_b) & y_l(kn_b R_b) & -1 \\ 0 & j_l'(kn_b R_b) kn_b & y_l'(kn_b R_b) kn_b & \alpha_s \end{bmatrix} \quad (6.13)$$

The characteristic equation for a microbubble is obtained by imposing equal to zero the determinant of equation 6.13.

A similar approach is followed for TM polarization.

6.4. Coupling mode theory

The interaction between the tapered fiber and the resonator (microsphere or microbubble) is calculated using the coupling mode theory described in chapter 2 [11]. Some hypotheses are used: i) weak coupling, ii) small internal resonator losses, iii) adiabatic tapered fiber.

The slowly varying amplitude A_{WGM} of the $WGM_{l,m,n}$ in the micro-resonator is expressed via the rate equation 1.2. In equation 6.14 is repeated in case of a passive device [11].

$$\frac{dA_{WGM}}{dt} = \left(-\frac{1}{\tau_0} - \frac{2}{\tau_{ext}} + i\Delta\omega \right) A_{WGM} - i\sqrt{\frac{2}{\tau_{ext}\tau}} A_{in,WGM} \tag{6.14}$$

Where:

- $\tau_0 = Q_0 / \omega_{WGM}$ is the intrinsic lifetime related to the total power loss, Q_0 being the intrinsic quality factor and ω_{WGM} the WGM resonant frequency;
- $\tau_{ext} = m\pi / \left(\omega \kappa^2 \right)$ is the lifetime related to the coupling, κ being the cavity decay rate or coupling coefficient obtained by implementing the overlap integral between the electromagnetic field of the WGM and the fiber mode as reported in equation 2.5;
- $\Delta\omega = \omega_f - \omega_{WGM}$ is the frequency detuning between input fiber frequency ω_f and WGM resonant frequency ω_{WGM};
- $\tau = 2\pi R n_{eff} / c$ is the round trip time inside the resonator with $R = R_S$ for a microsphere and $R = R_b$ for a microbubble; n_{eff} is the effective refractive index of the resonator;
- $A_{in,WGM}$ is the amplitude of the electromagnetic field at the input section of the fiber.

As described in paragraph 1.6, the loss phenomena considered in the evaluation of the quality factor Q_0 are:

i) absorption of the light in the micro-resonator;
ii) surface scattering due to the roughness of the spherical surface;
iii) tunneling of light due to the curvature of the micro-resonator.

It is possible to relate the absorption losses of the fluid that surrounds a microsphere or filling a microbubble to the contaminant concentration in the fluid. The quality factor due to the absorption losses can be expressed as in equation 6.15:

$$Q_{loss} = \frac{2\pi n_{eff}}{\lambda \alpha_P} \tag{6.15}$$

α_P is the power absorption coefficient for the considered WGM. Using the perturbation theory [87-88] α_P can be expressed as following:

$$\alpha_P = \frac{k}{\eta_0} \frac{\iint_{\infty} n^r(x,y) k(x,y) \left|\overline{E}(x,y)\right|^2 dA}{P_0} \tag{6.16}$$

η_0 is the characteristic impedance of the vacuum, $n^r(x,y)$ and $k(x,y)$ are the real and imaginary part of the refractive index along the transversal directions, P_0 is the real part of power flux through the micro-resonator section along the azimuthal direction ϕ. $\overline{E}(x,y)$ is the electric field of the unperturbed mode.

The imaginary part k of the refractive index can be related to the contaminant concentration in water:

$$k = \frac{\lambda}{4\pi} \alpha_{abs} \tag{6.17}$$

where λ is the WGM resonant wavelength and α_{abs} is the absorption coefficient of the considered solution for a certain contaminant concentration.

The transmittance of the device is calculated as the ratio between the slowly varying amplitude at the output and input section of the fiber coupled with the WGM having order *l,m,n*, respectively. It is given in equation 6.18 [12]:

$$T = \left| \frac{A_{out,WGM}}{A_{in,WGM}} \right|^2 \tag{6.18}$$

6.5. Numerical results

The model has been validated by comparing the simulated results with the experimental ones reported in [86]. A single-mode boron-germanium co-doped optical fiber (Fibercore PS1250/1500) with core and cladding diameters of 6.9 µm and 124.6 µm is considered. The adiabatic fiber taper has diameter of 18 µm. Preliminary FEM simulations demonstrated that the core modes of a single refractive index fiber having radius $R_f = 9\mu m$ and refractive index $n_f = 1.4433$ at the wavelength $\lambda = 1613.3nm$ are very similar to the cladding modes of the actual tapered section. The microsphere radius is $R_s = 145\mu m$. The microbubble radius is $R_b = 200\mu m$, the spherical internal volume of the bubble has radius $R_{in} = 196.7\mu m$ and it is filled with water. The simulation is performed in the range from $\lambda_1 = 1605nm$ to $\lambda_2 = 1620nm$, around the nominal wavelength $\lambda = 1613.3nm$ [86]. The refractive index wavelength dispersion for both microsphere/microbubble is calculated using to the Cauchy equation reported in Table 3.1.

The transmittance T is calculated for the different resonant $WGM_{l,m,n}$ as a function of the modal order X of the coupled $LP_{0,X}$ fiber mode for different gaps G = 10, 100, 200, 500 nm and 1 μm.

As an example, in Figure 6.3 is reported the transmittance T for the microsphere set-up. It is calculated for the different resonant $WGM_{l,m,n}$ as a function of the modal order X of the $LP_{0,X}$ for gap $G = 200nm$. The maximum coupling between microsphere and taper fiber is reached at minimum of the transmittance. It is obtained for the $WGM_{774,774,3}$ and fiber mode $LP_{0,7}$. The transmittance of $WGM_{774,774,3}$, coupled with $LP_{0,7}$, as a function of the detuning $\Delta\omega$, for the gap $G = 200nm$, is shown in Figure 6.4. The obtained results are in good agreement with the experiment reported in [86]. The minimum of the calculated transmittance $T = -2.84dB$ is obtained close to the wavelength $\lambda = 1615.5nm$.

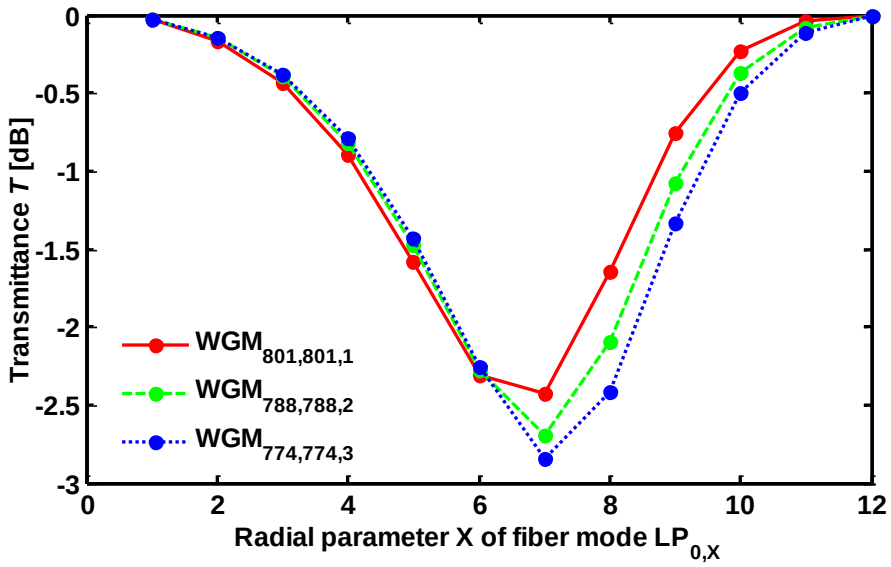

Fig. 6.3 Transmittance T calculated for the different resonant $WGM_{l,m,n}$ as a function of the modal order X of the $LP_{0,X}$ for microsphere set-up. The gap is G = 200 nm.

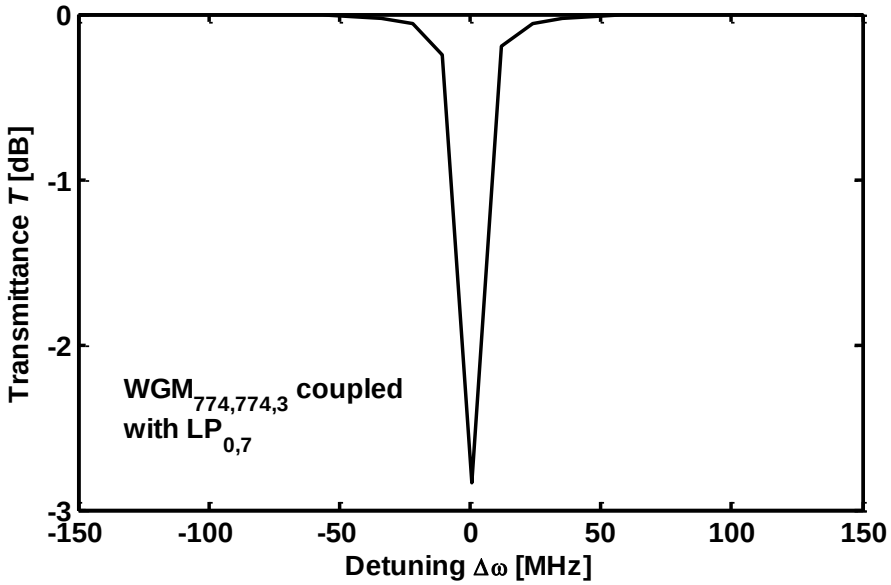

Fig. 6.4 Transmittance T of $WGM_{774,774,3}$, coupled with $LP_{0,7}$, as a function of the detuning $\Delta\omega$, for microsphere set-up. The gap is **G** = 200 nm.

In Figure 6.5 the transmittance T for the microbubble set-up calculated for the different resonant $WGM_{l,m,n}$ is reported as a function of the modal order X of the fiber mode $LP_{0,X}$ for the gap $G = 10nm$. The minimum of the transmittance, i.e. the maximum coupling between the microbubble and the fiber, can be obtained for the $WGM_{1109,1109,1}$ coupled with $LP_{0,10}$. The transmittance of $WGM_{1109,1109,1}$ coupled with $LP_{0,10}$ as a function of the detuning $\Delta\omega$, for the gap $G = 10nm$, is shown in Figure 6.6. The obtained results are in good agreement with the experiment reported in [86]. The minimum of the calculated transmittance $T = -2.97dB$ is obtained close to the wavelength $\lambda = 1605.3nm$. This simulated transmittance is very close to the measured transmittance reported in [86] for the same structure: $T = 0.52a.u. = -2.84dB$. The simulated quality factors of both microsphere and microbubble are in agreement with experiment [86]. Figure 6.7 shows the distribution of the norm of the

electromagnetic field E_θ in the microbubble (at left) and E_x in the fiber section (at right). The ten maxima along radial direction of the electromagnetic field in half fiber section are apparent.

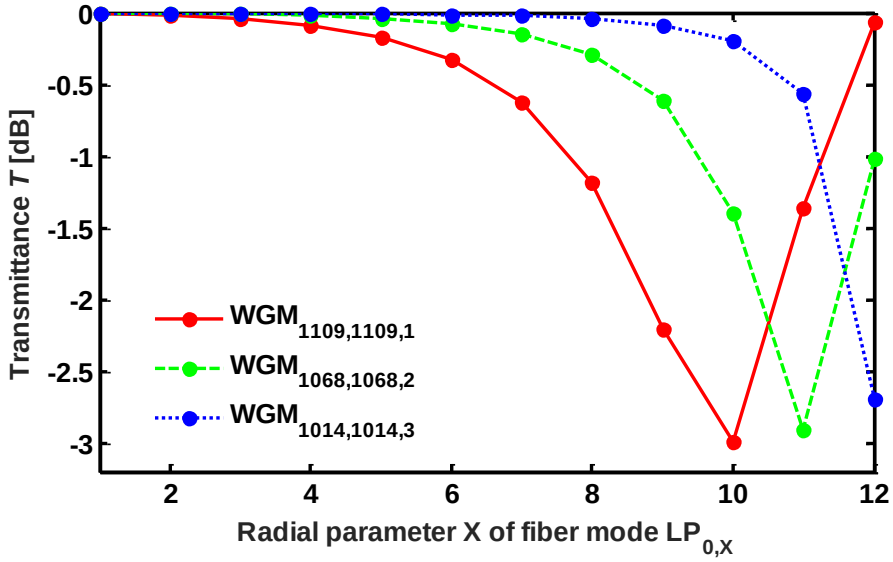

Fig. 6.5 Transmittance T calculated for the different resonant $WGM_{l,m,n}$ as a function of the modal order X of the $LP_{0,X}$ for microbubble set-up. The gap is G = 10 nm.

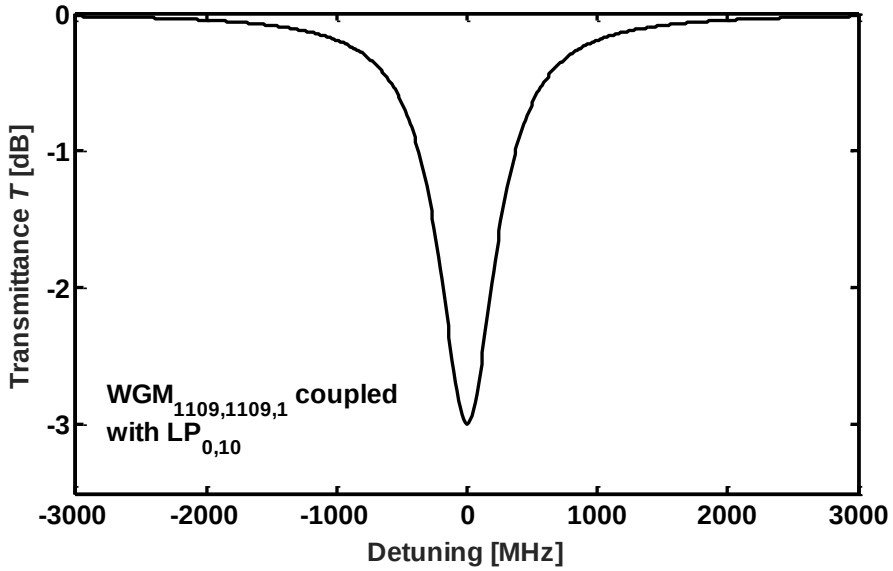

Fig. 6.6 Transmittance T of $WGM_{1109,1109,1}$, coupled with $LP_{0,10}$, as a function of the detuning $\Delta\omega$, for microbubble set-up. The gap is G = 10 nm.

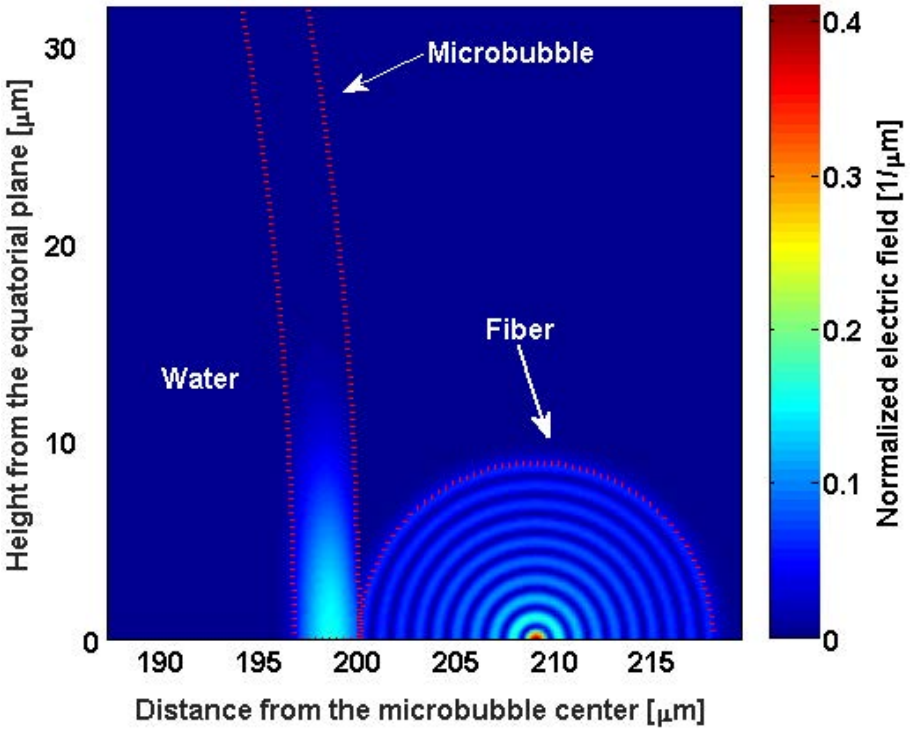

Fig. 6.7 Distribution of the normalized electric field E_θ in the microbubble (at left) and E_x in the fiber section (at right) for $WGM_{1109,1109,1}$ coupled with $LP_{0,10}$. The gap G = 10 nm.

In order to investigate the feasibility of a microbubble-based sensor, the sensitivity of the microbubble set-up to the glucose concentrations has been tested for $WGM_{1109,1109,1}$ coupled with $LP_{0,10}$. The absorption coefficient α_{abs} at the desired glucose concentration is taken from [89] and used in equation 6.17. Figure 6.8 illustrates the transmittance T as a function of glucose concentration C for C = 0, 1, 6, 90.9 g/dL. The variation of the transmittance between the case with pure water ($C = 0g/dL$) and the case of glucose saturation ($C = 90.9g/dL$) is $\Delta T \cong 9.8\%$. The transmittance variation ΔT is small because of the very small absorption of the glucose at $\lambda = 1613.3nm$. However, the transmittance variation reveals that the system is sensitive to the glucose concentration. Therefore,

the system can be optimized to operate for the sensing of different contaminants in water at the suitable absorption wavelength.

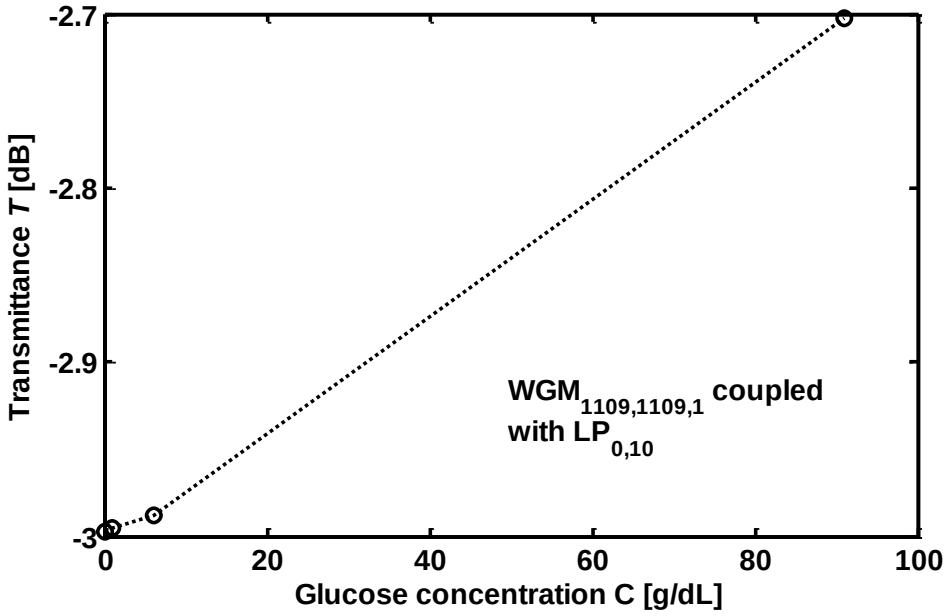

Fig. 6.8 Transmittance T, for the microbubble set-up, calculated for the $WGM_{1109,1109,1}$ coupled with $LP_{0,10}$ for gap G = 10 nm as a function of the glucose concentration. The full curve linearly interpolates the simulated points (circle).

6.6. Summary

A model for the design of all-in-fiber coupling system allowing quasi-distributed and wavelength selective addressing has been developed and validated. The system is based on a micro-resonator excited by a pair of identical LPGs with a fiber taper in between. This pair of identical LPGs operating in different wavelength bands allows selective coupling and interrogation of different micro-resonators by using the same optical link. The feasibility of a glucose sensor based on microbubble set-up has been investigated.

Chapter 7

Rare-earth doped micro-disks for Mid-Infrared applications

7.1. Introduction

In this chapter, results pertaining to the design and fabrication of rare-earth doped chalcogenide micro-disk for lasing in Mid-Infrared wavelength range are illustrated. The unique properties of chalcogenide glass and the whispering gallery mode (WGM) resonances make possible to obtain light emission via rare-earth transitions at long wavelengths. A home-made computer code is developed by taking into account the active behavior of the rare-earth ions interacting with the resonating whispering gallery modes. Firstly, in order to validate the model a light source based on chalcogenide micro-disk doped with erbium is investigated and compared with results obtained in [17]. Secondly, novel results pertaining a praseodymium-doped chalcogenide micro-disk emitting at 4.7 μm are presented. A number of promising applications in different areas such as biology, molecular spectroscopy and environmental monitoring are feasible.

7.2. Rare-earth doped micro-disks

As mentioned previously, whispering gallery mode resonators are characterized by low reflection losses and very small sizes. These peculiarities allow extremely small mode volumes, high power densities and high-quality factors Q.

Microspheres and micro-disks are key elements in a number of optical sensing set-ups. Micro-disks allow potentially higher integration degree, within complex optical circuits, than microspheres [5, 71], mechanical stability and low-cost fabrication. A drawback is the lower quality factor in comparison with microspheres. This is a consequence of the higher optical losses caused by the technological fabrication process [3]. A common technique for fabricating micro-disks is the conventional photolithography process [3]. An alternative technique is based on optical fiber tapering, cleaving and splicing [72]. Micro-disks made through these fabrication procedures exhibit high quality factors, close to $Q = 8 \times 10^6$ [73]. Moreover, Calvez et al. [74] demonstrated a micro-disk resonator vertically coupled to a buried oxide access waveguide, using AlGaAs/AlOx technology. They made some samples that resonate at the wavelength $\lambda = 1.6$ μm and exhibite quality factors up to $Q = 8.5 \times 10^3$.

The performance of biosensors based on micro-disks can be improved by increasing the overlap between electromagnetic mode and the surrounding biological fluid. The use of slot structures allows to overcome this limit [75]. Luminescent horizontal air slotted micro-disk resonators based on Silicon-Rich Nitride (SRN) are proposed for biosensing application [90]. The high refractive index of SRN allows the

fabrication of very small micro-disks, e.g. having a radius r = 4 μm and emitting around the wavelength λ = 0.8 μm.

A number of applications in different fields are feasible in Mid-Infrared wavelength range. Novel sensing set-ups can be designed to detect the vibrational transitions exhibited by many organic species and biomolecules [91]. Moreover, the atmosphere transmission windows at 3–5 μm and 8–13 μm make feasible applications in the field of remote sensing, free propagation communication systems and safety, e.g. remote explosive detection in airports and for border control [92]. Chalcogenide glasses are characterized by a wide transmissivity, in both Near- and Mid-Infrared wavelength ranges. As described in chapter 2, chalcogenide glasses present properties that make feasible applications in Mid-Infrared wavelength range.

In this chapter a home-made code is developed and exploited in order to model and design design a chalcogenide rare-earth-doped micro-disk. It is coupled to two ridge waveguides, the former guiding the pump beam and the latter the signal to be amplified/generated. Firstly, the code is validated by simulating an erbium doped micro-disk and comparing the results with those ones reported in [17]. Secondly, to the best of our knowledge, for the first time a Pr^{3+}-doped micro-disk amplifying/lasing at $\lambda \approx 4700$ nm is optimized and its feasibility is investigated.

7.3. Erbium-doped micro-disks[5]

As described in chapter 1, whispering gallery mode (WGM) formalism is generally employed to describe the electromagnetic field in circular geometries as spheres, disks, rings and toroids (see chapter 1). They are excited by using evanescent field provided by different coupling techniques, e.g. via prisms, waveguides or tapered optical fibers.

Figure 7.1 reports the layout of the device studied in this chapter. It is a rare-earth doped micro-disk coupled to two ridge waveguides, one for the signal at wavelength λ_s and the other for the pump at wavelength λ_p.

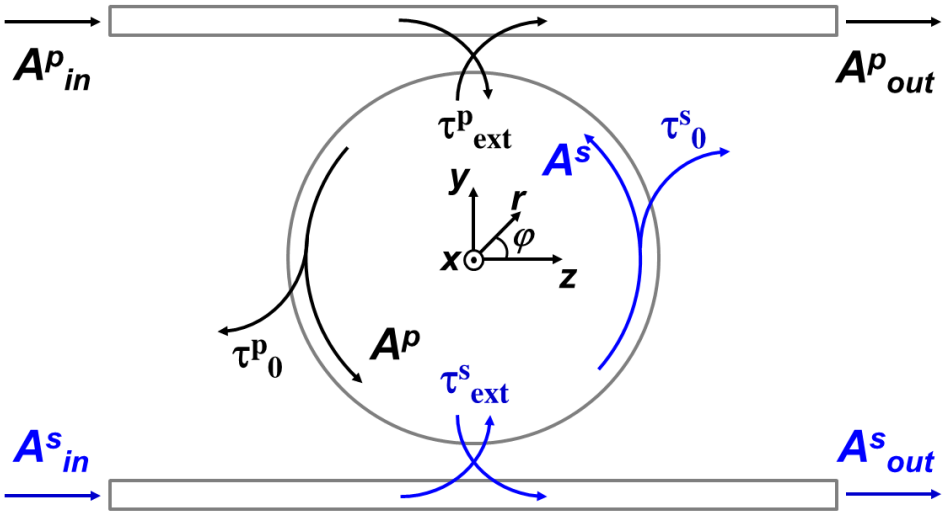

Fig. 7.1 Simulated structure is constituted by a micro-disk coupled to two ridge waveguides, one for the pump *P* and one for the signal *S*. A_{in} and A_{out} represent the amplitude of electromagnetic field at the input and output section of each waveguide. τ_{ext} e τ_0 represent the coupling and intrinsic lifetime, respectively.

[5] Work presented in this section has partially appeared in [70]: G. Palma, M. C. Falconi, F. Starecki, V. Nazabal, L. Bodiou, Y. Dumeige, J. Lemaitre, J. Charrier, F. Prudenzano, "Design of rare-earth doped chalcogenide microresonators for biosensing in mid-IR," *18th International Conference on Transparent Optical Networks*.

As described in section 1.4, a micro-disk $WGM_{m,n,p}$ is identified by three integers: m is the azimuthal parameter that defines the number of electromagnetic field maxima in the azimuthal direction ϕ, p is the longitudinal parameter that defines the number of field maxima in the longitudinal direction z; n is the radial parameter that defines the number of field maxima along the radial direction r.

Figure 7.2 shows the SEM images of (a) the top view of a ridge waveguide coupled to a chalcogenide micro-ring on a silicon substrate and (b) the cross sectional view of the coupling ridge waveguide, fabricated by photolithography process at FOTON Laboratory in Lannion. The ridge waveguide is made of a chalcogenide glass core on a silicon substrate.

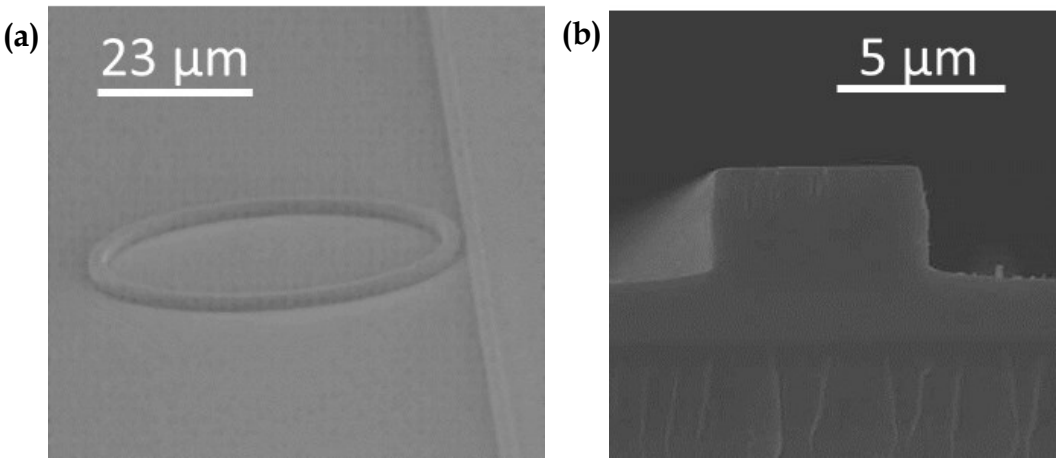

Fig. 7.2 SEM images of (a) the top view of a ridge waveguide coupled to a chalcogenide micro-ring on silicon substrate and (b) the cross sectional view of the coupling ridge waveguide [70].

The WGM electromagnetic field profile is simulated via a finite element method solver (FEM). The home-made software implements:

i) the coupled mode theory [11] in order to evaluate the coupling strength between the resonator and the coupling waveguide;

ii) the rate equations model of rare-earth ions population in order to simulate the light amplification. The most important phenomena of rare-earth/light interaction are taken into account, e.g. the absorption rates, the stimulated emission rate, the amplified spontaneous emission noise, the lifetime and branching ratios of the energy levels, the ion-ion energy transfers and the excited state absorption.

In order to validate the home-made software, an erbium-doped chalcogenide micro-disk has been taken into account. The signal wavelength is λ_s = 4500nm and the pump wavelength is at λ_p = 800nm.

7.3.1. Design of an erbium-doped micro-disk

The micro-disk and the waveguides are made of gallium lanthanum sulphide (GLS) glass [17]. Table 7.1 reports the main parameters employed in simulation, properly optimized by an ad-hoc design or taken by literature [17, 59] or measured on samples of glasses. The erbium concentration is $C_{Er} = 2.8 \times 10^{20}$ ions/cm^3.

The waveguides height h_w = 1.0μm and width w = 2.5μm have been identified in order to obtain the best trade-off between signal waveguiding and evanescent field requirement. In fact, waveguides with large

transversal dimension allow good electromagnetic field propagation but the tails of the evanescent field outside the waveguides are very weak and then the coupling with the disk WGMs is not strong enough. Figure 7.3 shows the intensity distribution in the waveguides at signal wavelength obtained using the aforesaid dimensions.

Table 7.1. Characteristics of simulated device [17, 59].

Parameter	Value
Disk radius $R_{\mu disk}$	40 µm
Disk thickness $h_{\mu disk}$	600 nm
Gap between signal waveguide and disk G_s	1.9 µm
Waveguides height h_w	1.0 µm
Waveguides width w	2.5 µm
Refractive index n_s at λ_S = 4500nm	2.35
Refractive index n_p at λ_P = 800nm	2.42
Uniform erbium concentration C	2.8×10^{20} ions/cm^3

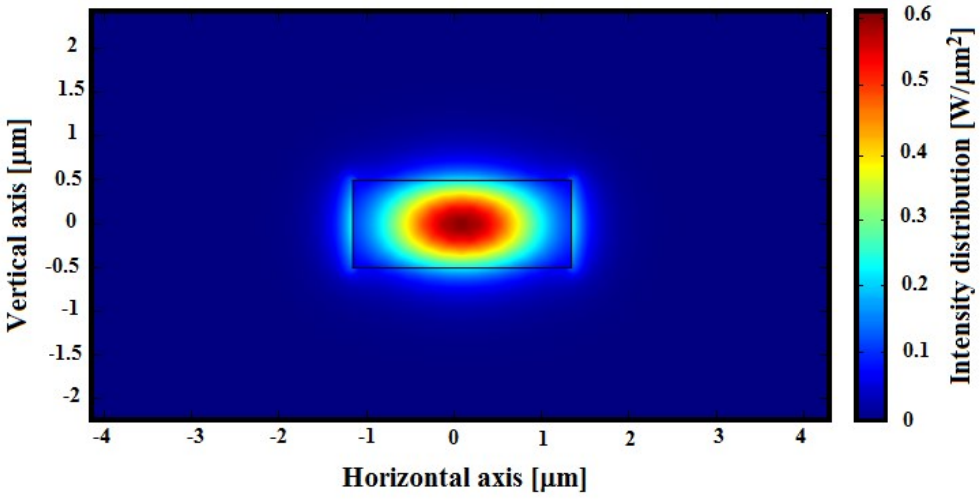

Fig. 7.3 Intensity distribution of the waveguide signal mode with the total mode power normalized to 1 W. The signal wavelength is λ_S = 4.5µm. The waveguide characteritics are reported in Table 7.1.

A preliminary study is conducted in order to recognize the value of gap G_P between micro-disk and waveguide pump that maximizes the gain. The gain of the amplifier is defined as the ratio of the signal power at output P_{out}^{signal} and input P_{in}^{signal} section of the signal waveguide:

$$g = 10\log_{10}\left(\frac{P_{out}^{signal}}{P_{in}^{signal}}\right) \tag{7.1}$$

Figure 7.4 reports the gain (blue line) as a function of the gap between micro-disk and pump waveguide. The designed device has dimensions reported in Table 7.1, input pump power $P_{in}^{pump} = 1W$ and input signal power $P_{in}^{signal} = 10nW$. The gap between micro-disk and signal waveguide is fixed to G_s = 1.9 μm. The vertical red line represents the value g_p = 100nm. It is apparent that an increase of g_p involves a decrease of the gain g because the coupling is less strong and then the inversion of population is too weak. For g_p = 100nm, the gain is g = 6.75dB. In order to observe the hypothesis of "weak coupling" in coupled mode theory, it is not advisable to use values of G_p less than 100nm.

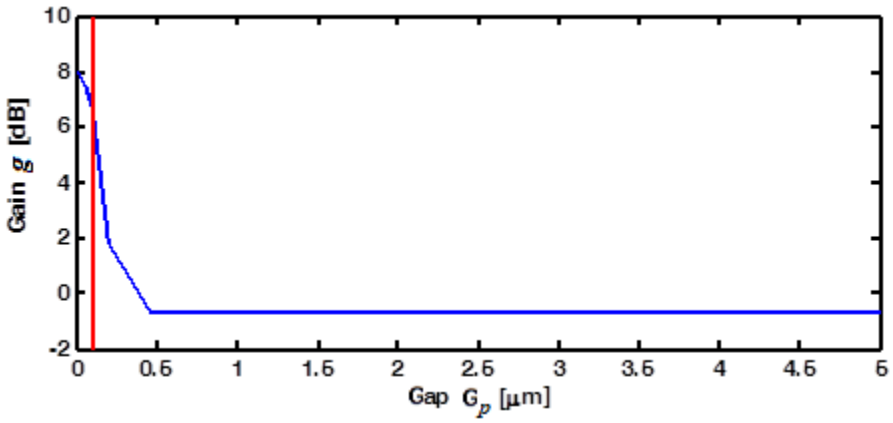

Fig. 7.4 Device gain g as a function of the gap G_p between micro-disk and pump waveguide (blue line). Input pump power is $P_{in}^{pump} = 1W$, input signal power is $P_{in}^{signal} = 10nW$ and the gap between micro-disk and signal waveguide G_s= 1.9 μm. Vertical red line marks G_p = 100nm.

7.3.2. Numerical results

The micro-disk supports hundreds resonating WGMs. Figure 7.5 shows the WGMs resonating in the micro-disk within a wavelengths range of 400nm centered on the nominal signal wavelength λ_S = 4.5µm. The simulation is carried out by imposing $p = m$. WGMs with $p \neq m$ can be neglected because they exhibit low overlapping factor Ω^{y}_{WGM} between mode distribution and the uniform rare-earth doping profile (see equation 2.3 in chapter 2). N = 73 WGM resonances with n parameter varying from 1 to 8 and m parameter varying from 56 to 91 are calculated. The obtained mean Free Spectral Range (FSR) is about FSR = 37 nm. Among all these solutions, one exhibits a strong interaction with rare-earth ions. It is the fundamental one $WGM_{86,86,1}$ having resonant wavelength close to the nominal wavelength λ_S = 4.5µm, where the $(^4I_{9/2} \rightarrow {}^4I_{11/2})$ erbium emission occurs.

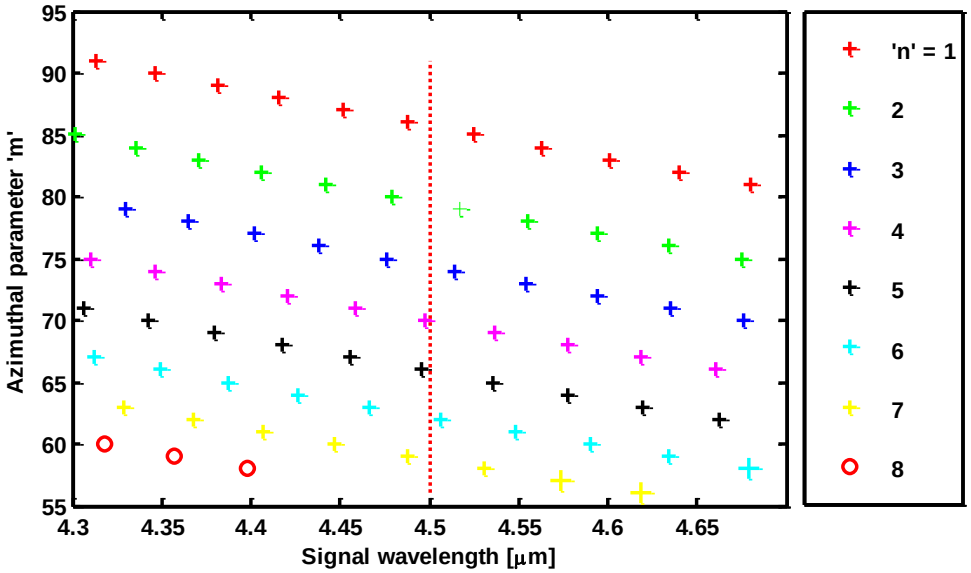

Fig. 7.5 WGMs resonances in the chalcogenide micro-disk with radius $R_{\mu disk}$= 40µm and height $h_{\mu disk}$=600nm around the nominal signal wavelength λ_S = 4.5µm . 'n' is the radial parameter.

Figure 7.6 shows the WGMs resonating in the micro-disk within a wavelengths range of 200nm centered on the nominal pump wavelength λ_p = 800nm. In the case of the pump, N = 2008 different modes, with *n* parameter varying from 1 to 8 and *m* parameter varying from 560 to 760, are identified. The mean FSR = 1.1 nm is calculated. The first seven radial order pump modes strongly interact with the signal via the rare-earth. Table 7.2 reports the characteristics of the WGMs strongly interact with the rare-earth close to signal λ_s = 4500nm and pump λ_p = 800nm.

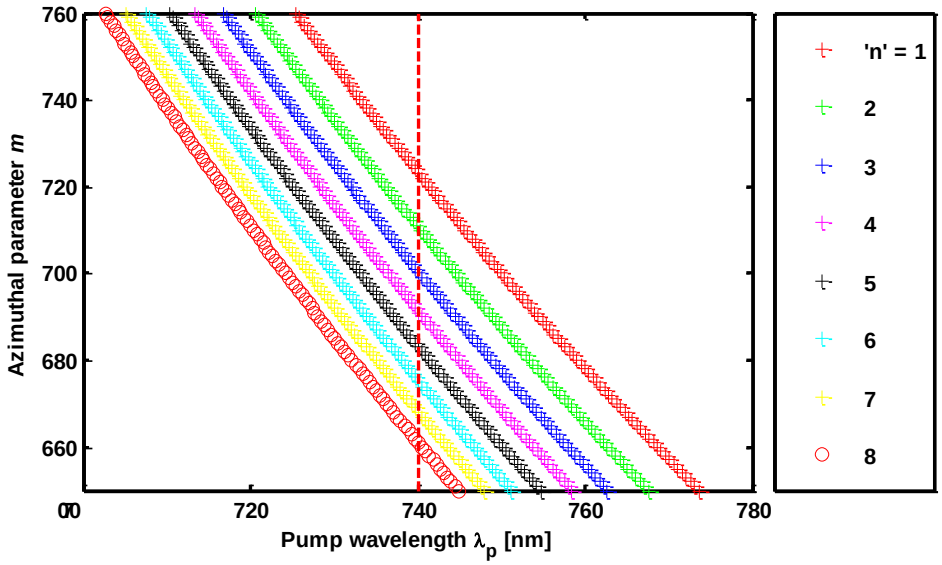

Fig. 7.6 WGMs resonances in the chalcogenide micro-disk with radius $R_{\mu disk}$= 40μm and height $h_{\mu disk}$=600nmaround the nominal pump wavelength λ_p = 800nm. 'n' is the radial parameter.

Table 7.2 Signal and pump WGM modes

	Resonance wavelength [nm]	*l* = *m* parameter	*n* parameter
Signal	4487.95	86	1
Pump	800.19	723	1
	799.63	711	2
	800.42	700	3
	800.37	691	4
	800.09	683	5
	800.41	675	6
	800.14	668	7

Figure 7.7 shows the distribution of the norm $|E|$ of the electromagnetic field along the radial direction r in a cut plane placed at half disk height. The electromagnetic amplitude is normalized so that integral of $|E|^2$ over all-space is equal to the unity. The plots refer to the fundamental signal mode $WGM_{86,86,1}^{SIGNAL}$ and to the three pump modes $WGM_{723,723,1}^{PUMP}$, $WGM_{711,711,2}^{PUMP}$ and $WGM_{668,668,7}^{PUMP}$. The abovementioned three pump modes overlap the signal field distribution along the r coordinate. However, all the seven pump modes with n = 1÷7 listed in Table 7.2 strongly interact with the signal via the rare-earth and are taken into account.

Figures 7.8a and 7.8b report the intensity distribution and resonant wavelengths of the signal and pump modes of Table 7.2 with the total mode power normalized to 1W.

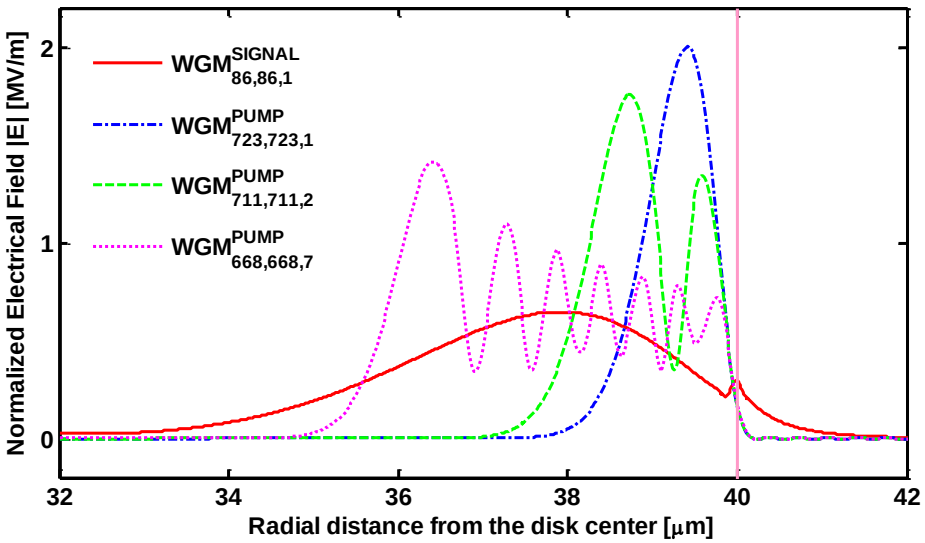

Fig. 7.7 Norm $|E|$ of the electromagnetic field for the fundamental signal $WGM_{86,86,1}^{SIGNAL}$ and three pump $WGM_{723,723,1}^{PUMP}$, $WGM_{711,711,2}^{PUMP}$ and $WGM_{668,668,7}^{PUMP}$, cross section view at half disk height. Micro-disk radius is $R_{\mu disk}$= 40μm and height is $h_{\mu disk}$=600nm.

Mode	Mode intensity distribution	λ [nm]
Signal $WGM_{86,86,1}$	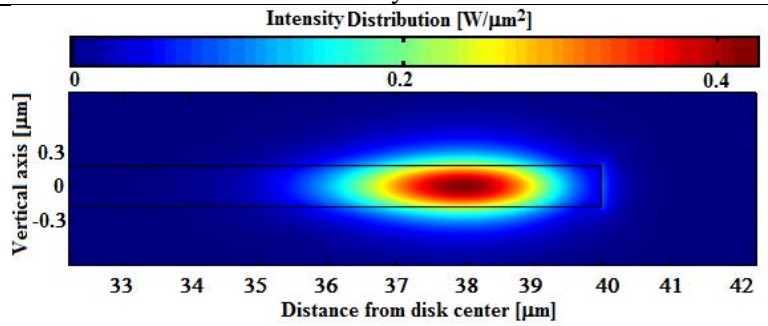	4487.95
Pump $WGM_{723,723,1}$	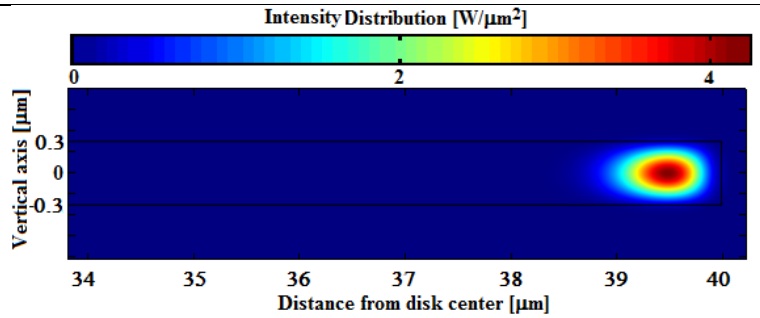	800.19
Pump $WGM_{711,711,2}$	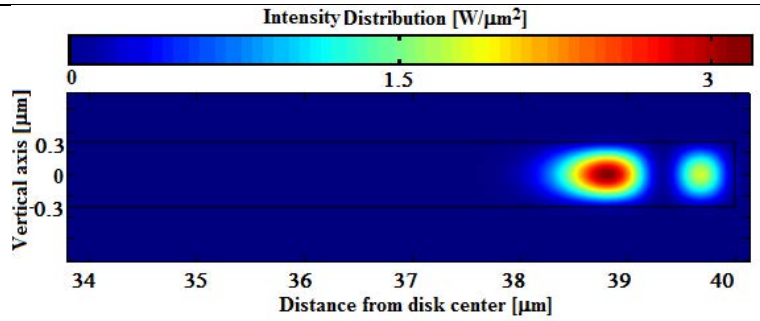	799.63
Pump $WGM_{700,700,3}$	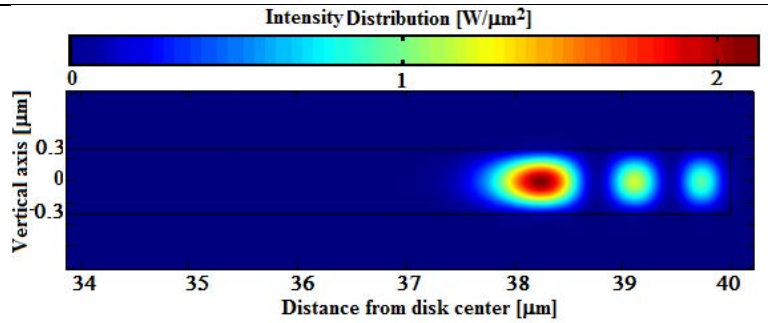	800.42

Figure 7.8a. Intensity distribution and resonant wavelengths of the signal mode and first three pump modes reported in Table 7.2 with the total mode power normalized to 1W. Micro-disk radius is $R_{\mu disk}$= 40μm and height is $h_{\mu disk}$=600nm.

Mode	Mode intensity distribution	λ [nm]
Pump $WGM_{691,691,4}$	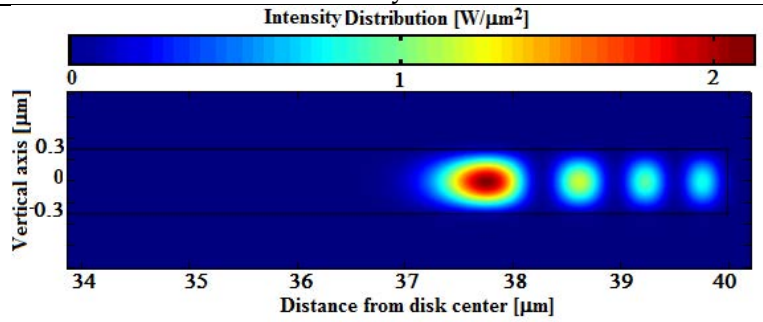	800.37
Pump $WGM_{683,683,5}$	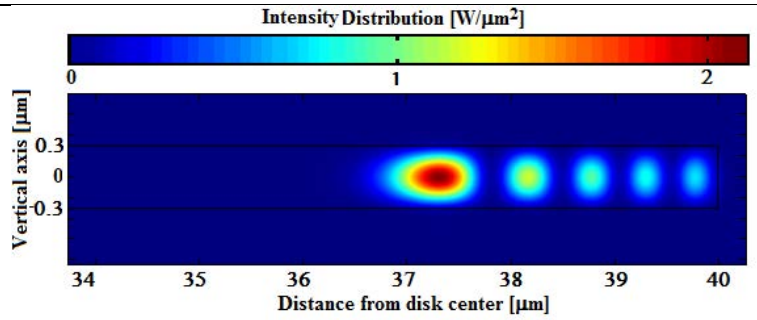	800.09
Pump $WGM_{675,675,6}$	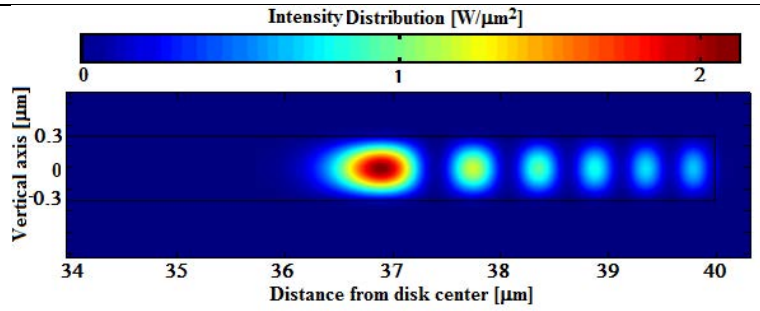	800.41
Pump $WGM_{668,668,6}$	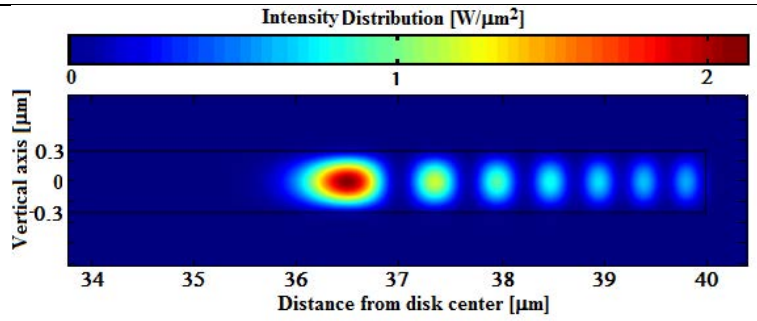	800.14

Figure 7.8b. Intensity distribution and resonant wavelengths of last four pump modes reported in Table 7.2 with the total mode power normalized to 1W. Micro-disk radius is $R_{\mu disk}$= 40μm and height is $h_{\mu disk}$=600nm.

Figure 7.9 reports the output signal power P_{out}^{signal}, collected at the end section of the signal waveguide, as a function of both the gap G_S between disk and signal waveguide and the input pump power P_{in}^{pump}.

The output signal strongly varies with the gap between signal waveguide and micro-disk. For a gap higher than G_S =3μm the coupling strength is low and thus the inversion of rare-earth population is weak. By reducing the gap, the coupling increases and thus a higher gain occurs. If the gap is less than G_S = 1.8μm the coupling is too strong and then most part of the signal leaves the micro-disk before obtain a gain level high enough. The maximum output signal power is P_{out}^{signal} = 10.21 μW and it is obtained for the input pump power P_{in}^{pump} = 0.5W and the gap G_S = 2.1μm. Concerning the pump, an increase of power involves an increase of population inversion and a gain increase till saturation.

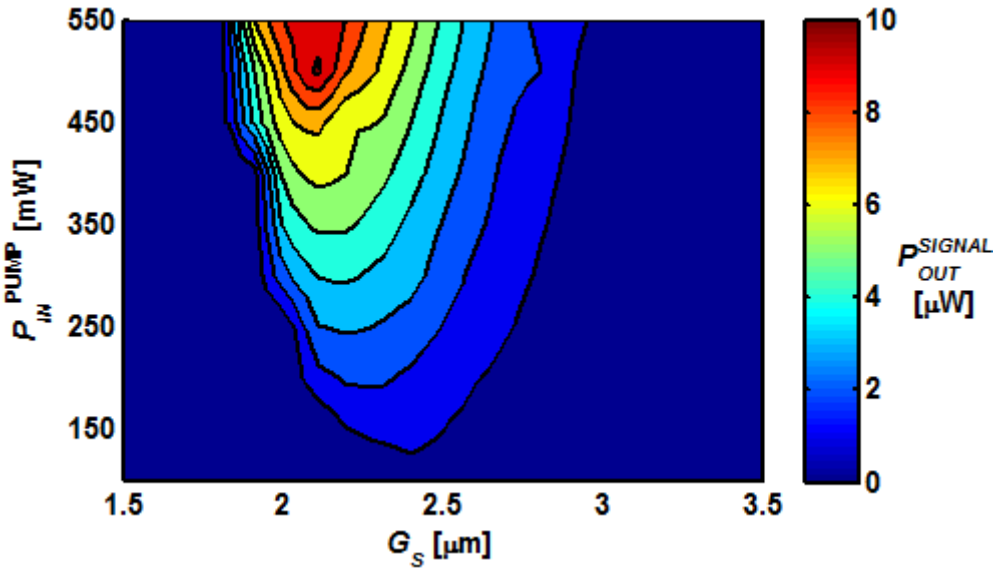

Fig. 7.9 Output signal power P_{out}^{signal} as a function of gap G_S between disk and signal ridge waveguide and input pump power P_{in}^{pump}. Erbium doped chalcogenide micro-disk with radius $R_{\mu disk}$= 40μm coupled with two ridge waveguides for signal at λ_S = 4500nm and pump at λ_P = 800nm.

Lasing at λ_S = 4500nm in the erbium-doped chalcogenide micro-disk is apparent. The results are in good agreement with those reported in [17]. The efficiency is low and thus in the next chapter praseodymium (Pr^{3+}) will be investigated in order to obtain higher lasing performance.

7.4. Praseodymium-doped micro-disks [6]

The designed structure is reported in Figure 7.10. It is constituted by a Pr^{3+}-doped chalcogenide micro-disk coupled to two coplanar ridge waveguides. A waveguide is designed for signal propagation at λ_s = 4700 nm and the other one for the pump at λ_p = 1550 nm.

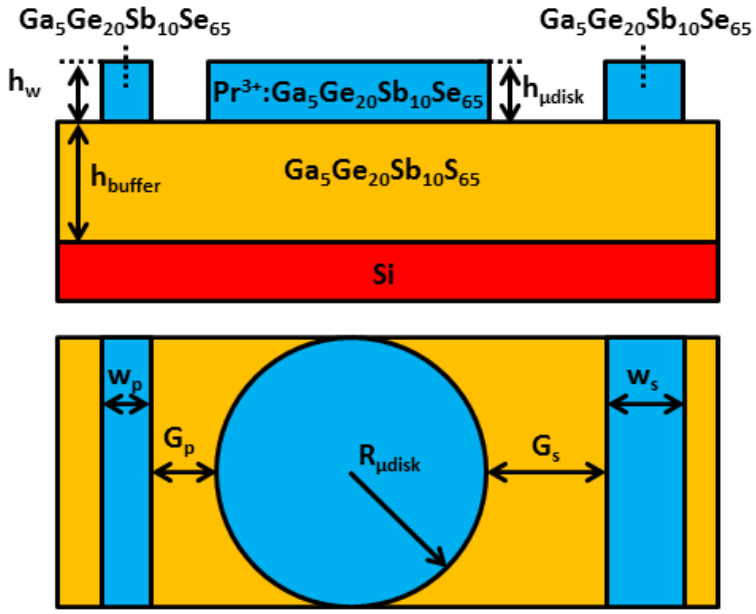

Fig. 7.10 The praseodymium doped Pr^{3+}:$Ga_5Ge_{20}Sb_{10}Se_{65}$ micro-disk coupled to the two waveguides made of the same glass. A buffer layer of $Ga_5Ge_{20}Sb_{10}S_{65}$ separates the micro-disk from the Si substrate.

[6] Work presented in this section has been submitted to *Journal of Lightwave Technology:* G. Palma, M. C. Falconi, F. Starecki, V. Nazabal, J. Ari, L. Bodiou, J. Charrier, Y. Dumeige, E. Baudet and F. Prudenzano, "Design of Praseodymium-Doped Chalcogenide Micro-Disk Emitting at 4.7 μm"

w_p and w_s are the widths of pump and signal waveguides, respectively; h_w, $h_{\mu disk}$ and h_{buffer} are the thicknesses of waveguides, micro-disk and buffer, respectively; G_p and G_s are the distances between the micro-disk and the pump/signal waveguide, respectively. In the model, the Si substrate is a semi-infinite layer. In order to prevent interaction between light and Si substrate, the buffer thickness is h_{buffer}=5µm.

7.4.1. Design of a praseodymium-doped micro-disk

The design procedure is divided in three main sections:

i) **passive structure design**, solving the Maxwell equations in order to obtain the electromagnetic field profile of both micro-resonator and optical waveguides, by neglecting the rare earth.
   This section is subdivided in two subsections for resonator:
   a) *passive structure coarse design* : by using WGM approximation (see section 1.5);
   b) *passive structure refined design* : by using FEM solver.

ii) **optical coupling**, performed by applying the coupled mode theory in order to model the coupling between the resonator and the guides;

iii) **active behavior simulation**, solving the rate equations for the rare-earth ions population densities in order to simulate the optical gain/lasing.

These steps can be followed, more in general, for the simulation of any active WGM micro-resonator.

The suitable geometrical parameters of the micro-disk and the coupling waveguides are chosen by considering:

i) a suitable micro-disk radius in order to have resonance at both the pump and signal wavelengths;

ii) waveguide dimensions in order to have single-mode propagation resonance at both the pump and signal wavelengths and maximize the overlapping factor Ω;

iii) the same thickness for waveguides and micro-disk because of sputtering process;

iv) buffer thickness in order to prevent interaction between waveguide and Si substrate.

The micro-disk and the two waveguides are made of $Ga_5Ge_{20}Sb_{10}Se_{65}$ selenide glass. The buffer layer is made of $Ga_5Ge_{20}Sb_{10}S_{65}$ sulphide glass. The refractive index wavelength dispersion are measured via ellipsometry and taken into account in the model. Figure 7.11 reports the measured refractive index as a function of wavelength. Table 7.3 reports the refractive indices at signal and pump wavelengths.

Table 7.3 Refractive indices at signal and pump wavelengths

Wavelength	Pr^{3+}:$Ga_5Ge_{20}Sb_{10}Se_{65}$	$Ga_5Ge_{20}Sb_{10}S_{65}$
1550 nm	2.60713	2.24778
4700 nm	2.56453	2.21683

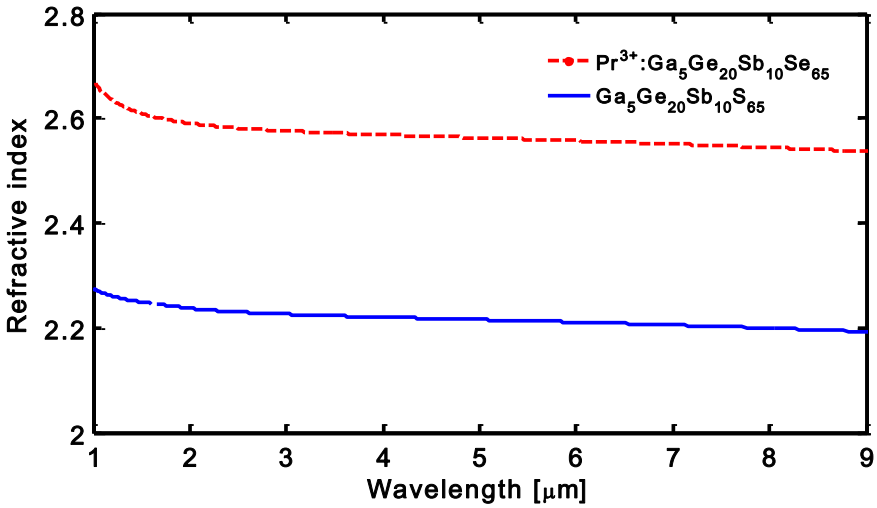

Fig. 7.11 Measured refractive index as a function of wavelength for Pr^{3+}:$Ga_5Ge_{20}Sb_{10}Se_{65}$ and $Ga_5Ge_{20}Sb_{10}S_{65}$. The measurement is made by ellipsometry.

Figure 7.12 reports the absorption coefficient α measured on $Ga_5Ge_{20}Sb_{10}Se_{65}$ un-doped glass. The spatially averaged absorption ζ of equation 1.28 is related to the absorption α as illustrated in equation 7.2:

$$\zeta = \alpha \frac{\iint_{\substack{\mu disk \\ cross-section}} \left|E^{P/S}\right|^2 dV}{\iint_{all-space} \left|E^{P/S}\right|^2 dV} \tag{7.2}$$

$E^{P/S}$ is the normalized electric field profile of the considered WGM mode. The integrals are calculated over the micro-disk cross section and over the whole space.

The quality factor related to the scattering surface losses $Q_{ss}^{P/S}$ (see equation 1.29) is calculated by using correlation length L_c = 150 nm and standard deviation σ_r = 10 nm [17]. The quality factor related to the radiation $Q_{rad}^{P/S}$ is evaluated by using the equation 1.31 and the electromagnetic field obtained via FEM simulation.

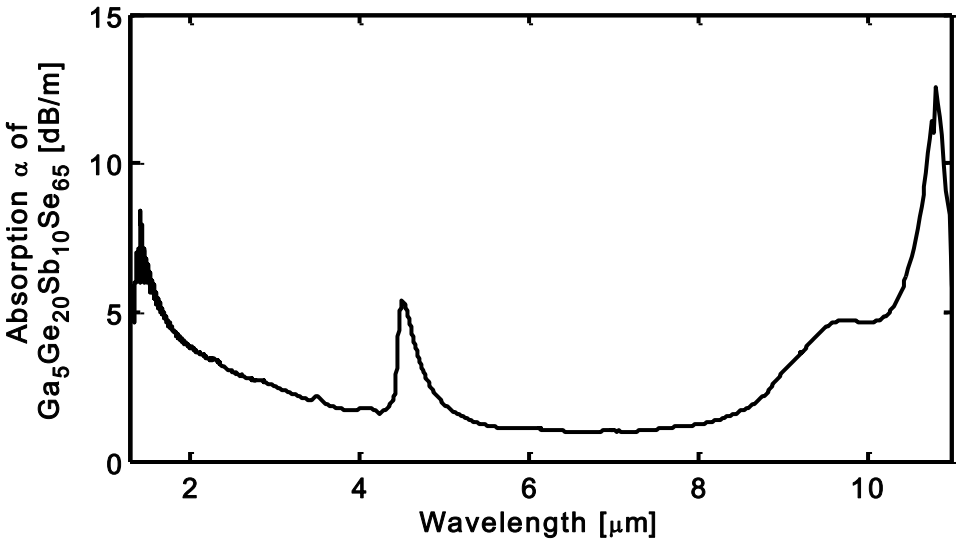

Fig. 7.12 Absorption coefficient α measured on $Ga_5Ge_{20}Sb_{10}Se_{65}$ un-doped fiber as a function of wavelength.

The praseodymium spectroscopy parameters are reported in chapter 2 and they are here summarized. Table 7.4 reports branching ratios β_{ij}, pure-radiative lifetimes τ_i and non-radiative lifetimes T_i measured for the considered Pr^{3+}-doped $Ga_5Ge_{20}Sb_{10}Se_{65}$ glass. Figure 7.13 illustrates the absorption and emission cross-sections of the same glass.

Table 7.4 Spectroscopic parameters of the Pr^{3+}:$Ga_5Ge_{20}Sb_{10}Se_{65}$

Transition	Wavelength [nm]	Branching ratio β	Pure-radiative lifetime τ_i [ms]	Non-radiative lifetime T_i[ms]
$^3H_5 \rightarrow {}^3H_4$	4604	$\beta_{21} = 1.00$	$\tau_2 = 11.36$	$T_2 = 16.70$
$^3H_6 \rightarrow {}^3H_5$	4351	$\beta_{32} = 0.43$	$\tau_3 = 4.66$	$T_3 = 6.09$
$^3H_6 \rightarrow {}^3H_4$	2237	$\beta_{31} = 0.57$		
$^3F_{34} \rightarrow {}^3H_6$	5769	$\beta_{43} = 0.02$		
$^3F_{34} \rightarrow {}^3H_5$	2481	$\beta_{42} = 0.18$	$\tau_4 = 0.21$	$T_4 = 1.26$
$^3F_{34} \rightarrow {}^3H_4$	1612	$\beta_{41} = 0.80$		

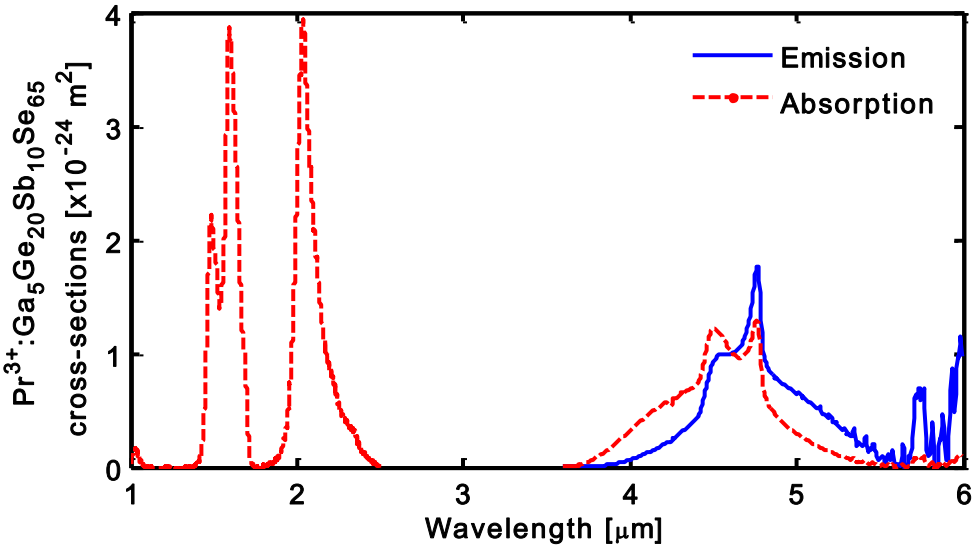

Fig. 7.13 Calculated emission and absorption cross-sections for the Pr3+: Ga5Ge20Sb10Se65 glass.

The signal waveguide is simulated with FEM solver by changing the thickness in the range $0.5 \div 1.5 \mu m$ with a step of 0.1 μm and the width in the range $1 \div 10 \mu m$ with a step of 0.5 μm. The confinement factor Ω is evaluated for each waveguide mode. It is defined as the ratio of the integrals of normalized electric field profile E_w of the considered waveguide mode calculated over the waveguide cross-section and over the whole space:

$$\Omega = \frac{\iint\limits_{\substack{waveguide \\ cross-section}} |E_w|^2 \, dxdy}{\iint\limits_{all-space} |E_w|^2 \, dxdy} \tag{7.3}$$

Figure 7.14 reports the confinement factor Ω as a function of width and height for a single-mode waveguide. For a fixed height, for small widths the waveguide is at first below the cut-off and then exhibits single-mode propagation, while for large widths it exhibits multi-mode propagation. Only single mode propagation is represented.

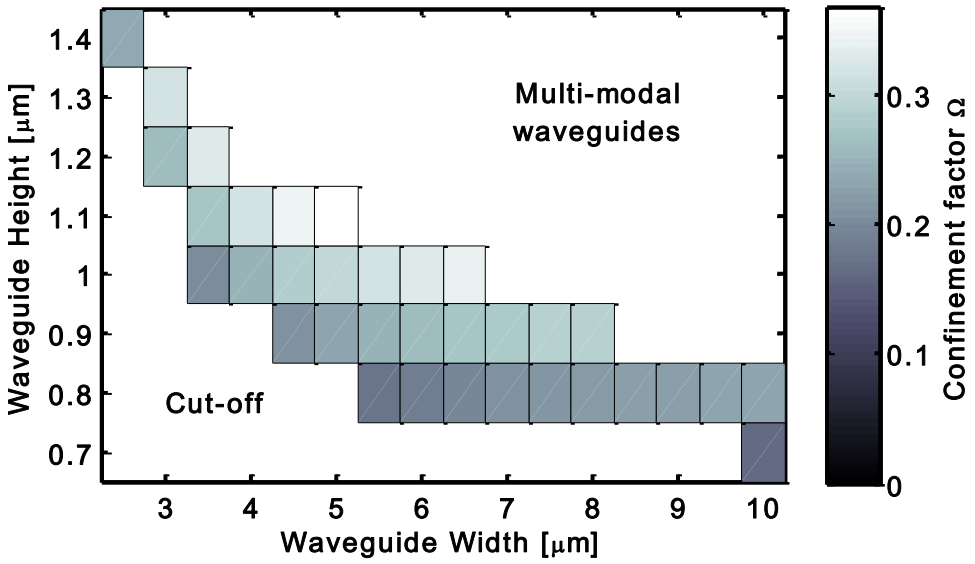

Fig. 7.14 Confinement factor Ω as a function of width and height for single-mode signal waveguide.

The confinement factor Ω increases with the waveguide width, i.e. the evanescent field becomes weaker. As an example, Figure 7.15 illustrates the electric field norm distribution for single-mode waveguides at signal wavelength having height h_w = 1 µm and width a) w_s = 3.5 µm and b) w_s = 6.5 µm. The confinement factors are Ω = 0.20 and Ω = 0.34. It is apparent that a large confinement factor Ω indicates small evanescent tails.

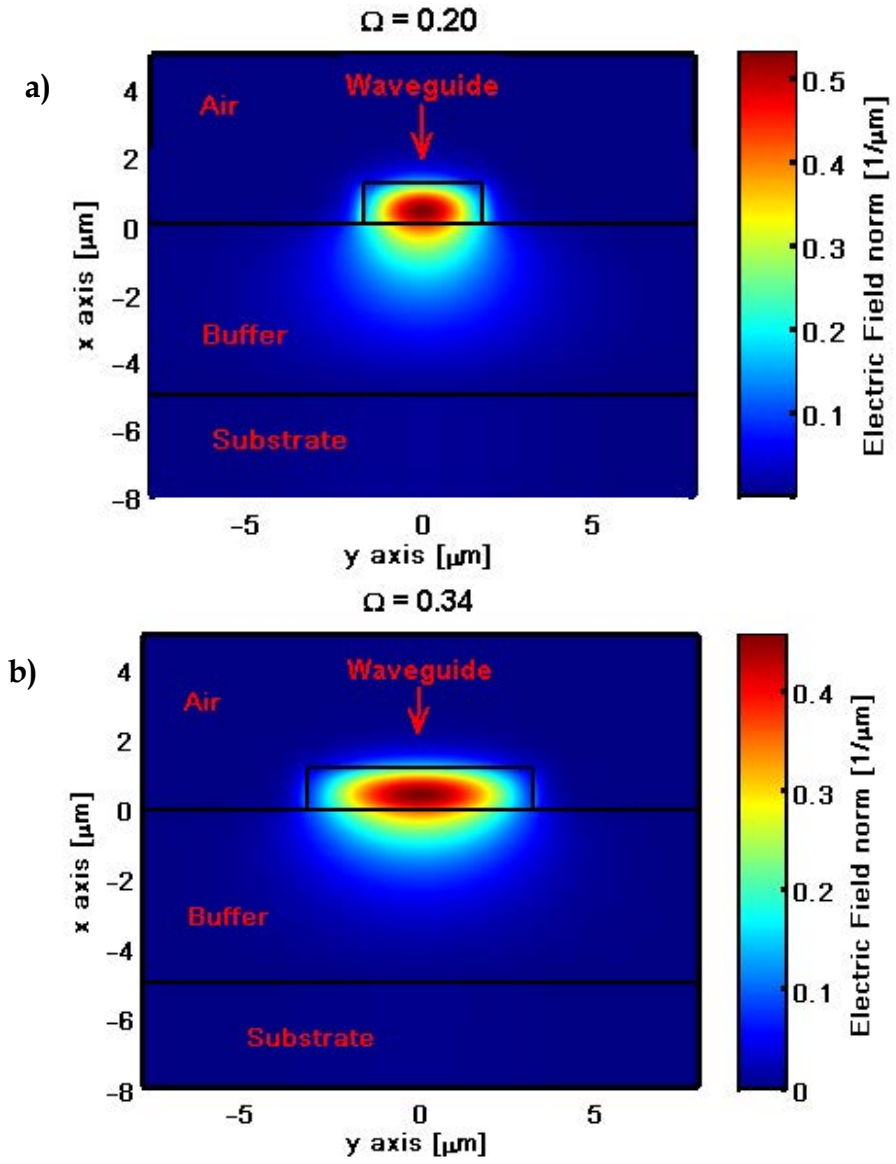

Fig. 7.15 Distribution of the electric field norm for the fundamental mode in signal waveguide having h_w = 1 µm and a) w_s = 3.5µm, b) w_s = 6.5 µm.

A height $h_w = 1.2\mu m$ and a width $w_s = 3.5\mu m$ are chosen for the signal waveguide. The micro-disk and the two waveguides have the same thickness, $h_{\mu disk} = h_w = 1.2\mu m$. This choice is made by supposing to exploit an RF sputtering process for the device construction.

The FEM solver is used to simulate the pump waveguide and a width w_p = 0.5 µm is identified in order to obtain single-mode propagation. In the signal waveguide the fundamental mode polarization is quasi-TE, while in the pump waveguide it is quasi-TM.

The coarse design of micro-disk is performed by using the WGM approximation (see section 1.5). Figure 7.16 reports the micro-disk effective refractive index n_{eff} as a function of micro-disk thickness obtained via equation 1.22 for λ_s = 4700 nm. In case of $h_{\mu disk} = 1.2\mu m$, the effective refractive index is $n_{eff} = 2.33$ for fundamental mode having longitudinal parameter p = 1.

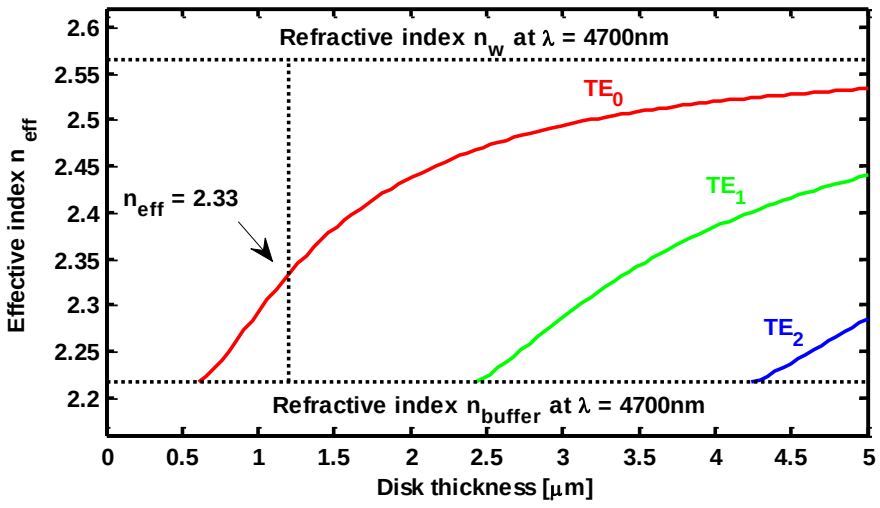

Fig. 7.16 Micro-disk effective refractive index n_{eff} as a function of disk-thickness for λ_s = 4700 nm. The subscript p in TE_p is the longitudinal parameter of the considered $WGM_{m,n,p}$.

The characteristic equation 1.26 is solved by imposing fundamental WGM solution, i.e. by putting $l = m$ and $n = 1$. The micro-disk radius $R_{\mu disk}$ and the azimuthal parameter m of the WGM having resonant wavelength close to λ_s = 4700 nm are identified. Figure 7.17 illustrates the micro-disk radius $R_{\mu disk}$ as a function of wavelength obtained by solving equation 1.26. The smallest admissible micro-disk radius is chosen: $R_{\mu disk}$ = 65 μm. This allows to reduce the computational cost of the simulation. Table 7.5 summerizes the designed geometry.

Table 7.5 Geometry of the optimized amplifier

Dimension	Value [μm]
Micro-disk radius $R_{\mu disk}$	65.0
Micro-disk and waveguides thicknesses $h_{\mu disk} = h_w$	1.2
Buffer thickness h_{Buffer}	5.0
Signal waveguide width w_s	3.5
Pump waveguide width w_p	0.5

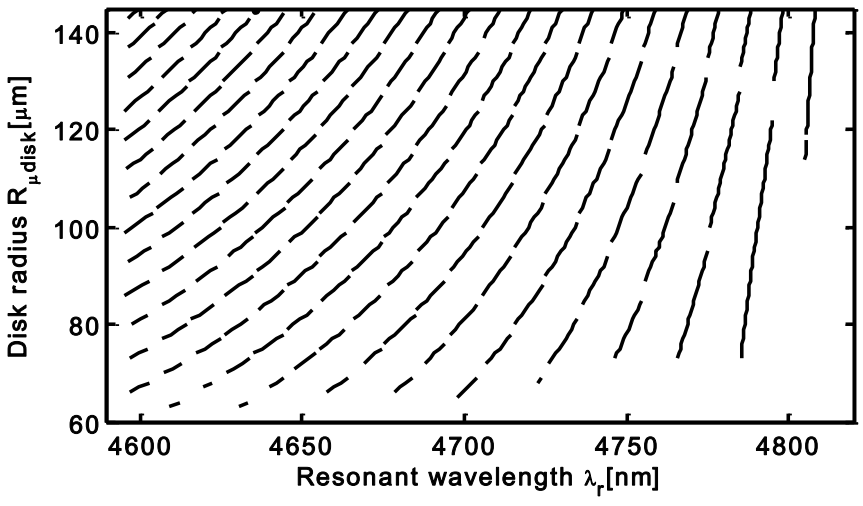

Fig. 7.17 Micro-disk radius $R_{\mu disk}$ as a function of the wavelength obtained by solving equation 1.26.

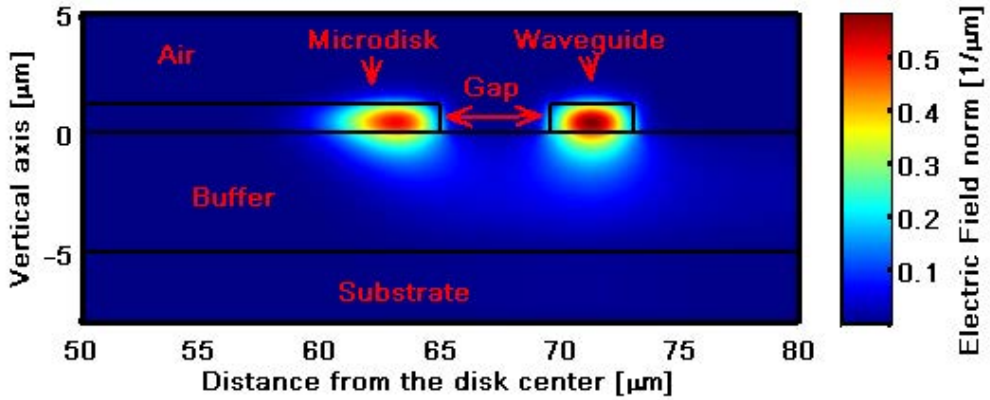

Fig. 7.18 Distribution of the electric field norm for the fundamental signal mode $WGM_{194,1,1}$ and the fundamental waveguide mode with g_s = 4.3 µm.

The micro-disk obtained using the coarse design method is tested with FEM solver in order to verify the resonance at signal and pump wavelengths.

Figure 7.18 illustrates the distribution of the electric field norm of the fundamental signal mode $WGM_{194,1,1}$ and of the fundamental waveguide mode with g_s = 4.3 µm for the passive device.

7.4.2. Numerical Results

The FEM solver is used to simulate the micro-disk WGMs and waveguide propagation modes by considering the geometrical parameters of Table 7.5. In the simulation, the fundamental mode $WGM_{194,1,1}$ at the signal wavelength λ_s = 4700 nm is considered. Moreover, the first seven WGMs are considered at the pump wavelength λ_p = 1550 nm. The signal gain is maximized by exploiting different pump modes in order to increase the interaction between pump and rare-earth, in order to

generate/amplify signal [17]. Table 7.6 reports the parameters of the simulated modes.

The output signal power P_{out}^{signal} versus the distance g_p between micro-disk and pump waveguide is simulated for the input signal power $P_{in}^{signal} = -30dBm$ and input pump power $P_{in}^{pump} = 100mW$, praseodymium concentration C_{Pr} = 3000 ppm and distance G_s between micro-disk and signal waveguide G_s = 4.45 μm. By increasing the distance g_p between micro-disk and pump waveguide, an almost constant and maximized signal power P_{out}^{signal} is simulated till G_p = 350 nm. Then, for larger G_p values, the output signal power P_{out}^{signal} decreases. A value G_p = 200 nm is chosen.

Table 7.6 WGM Characteristics at signal and pump wavelengths

$WGM_{m,n,p}$	λ_r [nm]	Q_{abs} [$\cdot 10^6$]	Q_{ss} [$\cdot 10^4$]	Q_{rad} [$\cdot 10^7$]	Q [$\cdot 10^4$]
		Signal mode			
$WGM_{194,1,1}$	4669.0	5.58	132.71	1.48	99.96
		Pump modes			
$WGM_{657,1,1}$	1550.4	7.71	4.90	96.4	4.87
$WGM_{645,2,1}$	1550.0	7.57	4.86	96.1	4.83
$WGM_{635,3,1}$	1550.2	7.45	4.83	95.7	4.79
$WGM_{626,4,1}$	1550.7	7.35	4.81	95.1	4.77
$WGM_{618,5,1}$	1550.7	7.26	4.78	93.7	4.51
$WGM_{611,6,1}$	1549.7	7.18	4.74	91.3	4.71
$WGM_{604,7,1}$	1549.6	7.10	4.72	90.8	4.69

The maximum output signal power $P_{out,MAX}^{signal}$ as a function of input pump power P_{in}^{pump} and praseodymium concentration C_{Pr} is illustrated in Figure 7.19. The maximum output signal power $P_{out,MAX}^{signal}$ is the largest value obtained within the G_s range 0.5 ÷ 5.5 μm. The simulations are performed by changing the input pump power P_{in}^{pump} in the range 0.01 ÷ 50 mW and the praseodymium concentration C_{Pr} in the range 100 ÷ 10000 ppm. The input signal power is $P_{in}^{signal} = -30dBm$. By increasing the input pump power P_{in}^{pump} or praseodymium concentration C_{Pr}, the maximum output signal power $P_{out,MAX}^{signal}$ increases. The increase of P_{in}^{pump} or C_{Pr} induces a similar effect. The population inversion is improved and thus the output signal power P_{out}^{signal} is maximized.

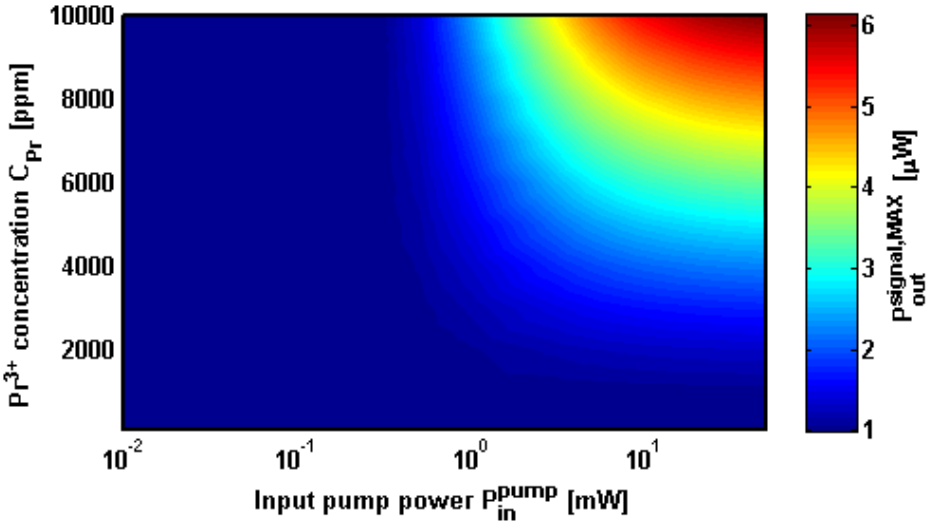

Fig. 7.19 Maximum output signal power $P_{out,MAX}^{signal}$ as a function of input pump power P_{in}^{pump} and praseodymium concentration C_{Pr}. The input pump power P_{in}^{pump} varies in the range 0.01 ÷ 50 mW and the praseodymium concentration C_{Pr} in the range 100 ÷ 10000 ppm. The input signal power is $P_{in}^{signal} = -30dBm$.

Figure 7.20 illustrates the optical gain g, as defined in equation 7.1, as a function of distance G_s between micro-disk and signal waveguide for the input pump power $P_{in}^{pump} = 0.01mW$. It is apparent that the input pump power is too weak to achieve the inversion of population. The optical gain is negative because the losses due to the light propagation in the micro-disk are higher than the gain.

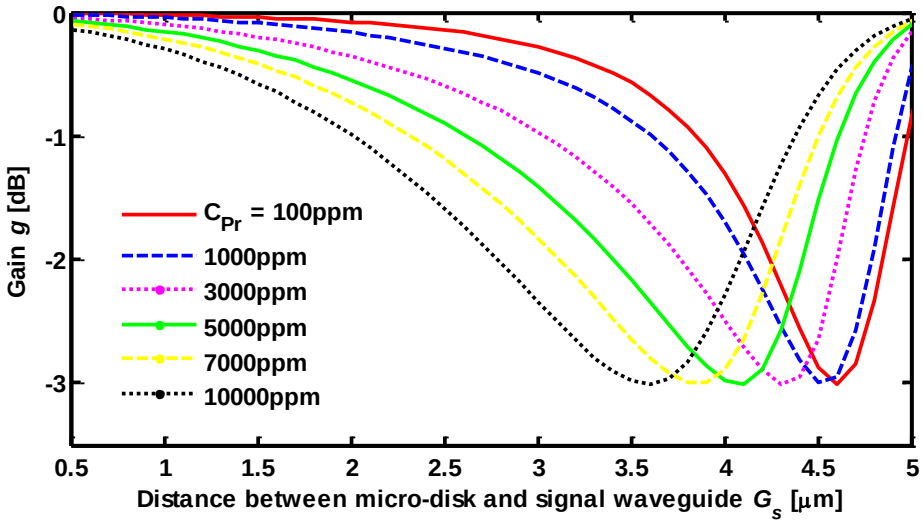

Fig. 7.20 Optical gain g as a function of distance G_s between micro-disk and signal waveguide for different praseodymium concentration. The input pump power is $P_{in}^{pump} = 0.01mW$ and the input signal power is $P_{in}^{signal} = -30dBm$.

Figure 7.21 illustrates the optical gain g as a function of distance G_s between micro-disk and signal waveguide for the input pump power $P_{in}^{pump} = 50mW$. For C_{Pr} = 100 ppm and C_{Pr} = 1000 ppm, the concentration is too low in order to have optical gain. By increasing the praseodymium concentration C_{Pr}, the input pump power activates the interaction between light and rare-earth. The maximum gain is $g \approx 7.9$ dB and it is obtained with C_{Pr} = 10000 ppm and $G_s \approx 4.1$ μm. By increasing the concentration, the peak of the optical gain g is obtained for smaller value of the distance G_s between micro-disk and signal waveguide. In fact, by increasing the ions populations, the signal absorption increases due to the transition $^3H_4 \rightarrow {}^3H_5$. In order to compensate this larger absorption, a stronger optical coupling is needed.

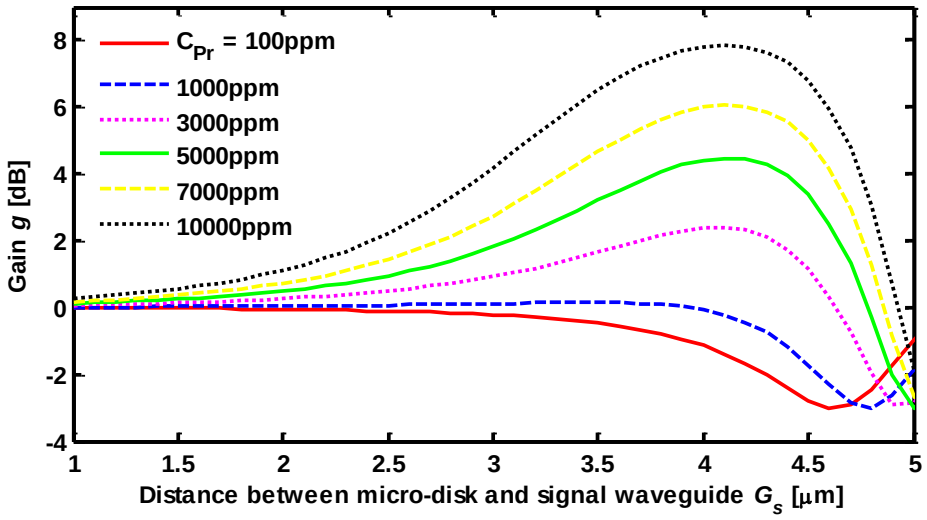

Fig. 7.21 Optical gain g as a function of distance G_s between micro-disk and signal waveguide for different praseodymium concentrations. The input pump power is $P_{in}^{pump} = 50mW$ and the input signal power is $P_{in}^{signal} = -30dBm$.

Figure 7.22 reports the ions populations as a function of the time t in the case of the highest gain $g \approx 7.9$ dB, obtained for $P_{in}^{pump} = 50$ mW, $C_{Pr} = 10000$ ppm and $G_s = 4.1$ μm. At the initial time $t = 0$ s, the pump signal is applied. The pump absorption at the wavelength $\lambda_p \approx 1.55$ μm induces a fast decrease of the population N_1 of the ground level $^3H_4$ and an increase of the population N_4 of the level $^3F_{34}$. Afterwards, the spontaneous decays (radiative and non-radiative) lead to an increase of the populations N_3 and N_2 of levels $^3H_6$-$^3F_2$ and $^3H_5$, respectively. The light emission at $\lambda_s \approx 4.7$ μm is related to the transition $^3H_5 \rightarrow {}^3H_4$ (ions populations N_2 and N_1).

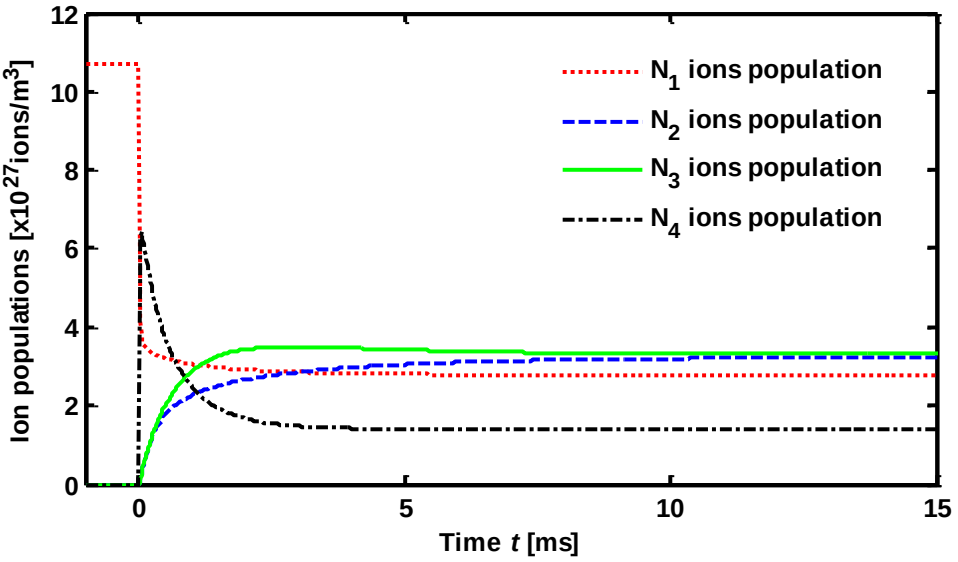

Fig. 7.22 Ions populations as a function of the time in the case of the highest gain: $P_{in}^{pump} = 50$ mW, $P_{in}^{signal} = -30 dBm$, $C_{Pr} = 10000$ ppm, $g_s = 4.1$ μm. In $t = 0$ s the pump signal is applied.

Finally, the laser behavior, i.e. without input signal is simulated. Figure 7.23 illustrates the output signal power P_{out}^{signal} as a function of the input power P_{in}^{pump}, with C_{Pr} = 10000 ppm. In the laser behavior, the maximum value of output signal power P_{out}^{signal} is obtained with the distance between micro-disk and signal waveguide $G_s \approx 4.1$ μm. The pump threshold is close to 0.4 mW. The slope efficiency S_E is defined as the ratio between the output signal power and the input pump power. The best slope efficiency is close to $S_E = 8.08\times10^{-4}$ in the range of input pump power P_{in}^{pump} from 2 to 6 mW. This slope efficiency is about six times higher than that one calculated for the erbium-doped micro-disk reported in [17] and simulated in the previous chapter.

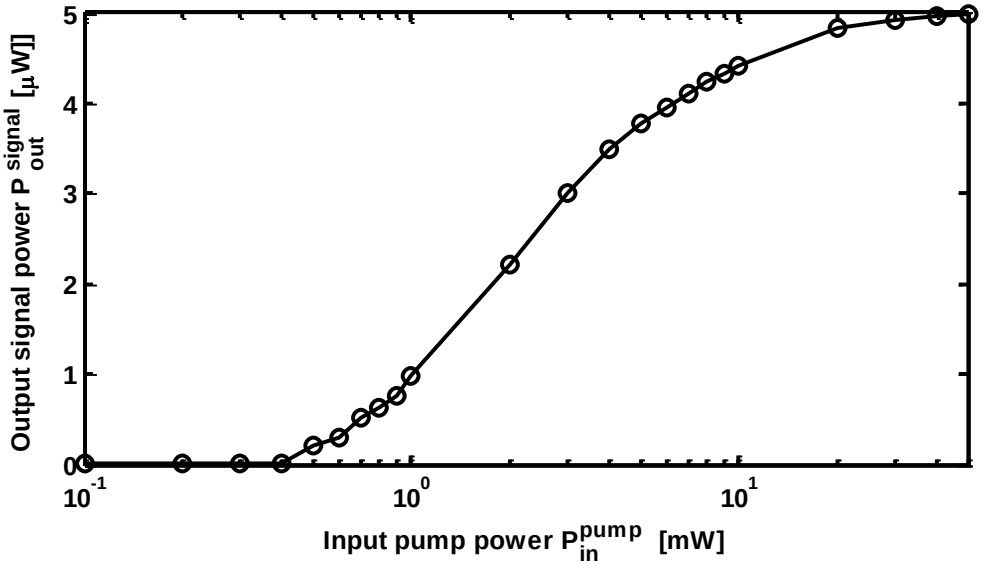

Fig. 7.23 Output signal power P_{out}^{signal} as a function of the input pump power P_{in}^{pump} with C_{Pr} = 10000 ppm, G_s = 4.3 μm.

7.5. Summary

A home-made computer code is developed in order to simulate rare-earth doped micro-disks. The code is validated by simulating an erbium-doped micro-disk. To the best of our knowledge the design of an amplifier based on a chalcogenide Pr^{3+}-doped micro-disk coupled to two ridge waveguides is performed. The micro-disk has a radius of 65 µm and a thickness of 1.2 µm. A very high gain $g \approx 7.9$ dB is simulated for a Pr^{3+} concentration of 10000 ppm, an input signal power of -30 dBm and an input pump power of 50 mW. In the laser behavior, the maximum slope efficiency 8.08×10^{-4} is obtained for Pr^{3+} concentration of 10000 ppm and input pump power in the range 2 - 6 mW. The pump threshold is 0.4 mW.

Conclusions

In this thesis an accurate 3D numerical model is developed in order to simulate active/passive devices based on WGM resonators excited/interrogated by a fiber/waveguide. The computer code is developed in three steps: i) solving Maxwell equations in order to obtain the electromagnetic distribution in the structures, ii) applying coupled mode theory in order to obtain the coupling strength between micro-resonator and fiber/waveguide and iii) solving the rate equations in order to simulate the light/rare-earth interaction.

The model is suitably integrated with a global optimization approach: the particle swarm optimization (PSO). This allows to develop an useful and versatile algorithm. The algorithm can be used in two manners : i) to develop a novel designing method applied for the first time to WGM resonators; ii) to define a innovative procedure to evaluate the spectroscopic parameters of rare-earth doped glass microspheres.

Firstly the model is used for an accurate design of Er^{3+}-doped chalcogenide microsphere coupled to a tapered fiber using the PSO procedure. The method proved surprising performance in terms of convergence and efficiency in the design of an amplifying system working close to 2700nm. As results it is possible to design a microsphere amplifier having simulated gain of g = 33.7 dB, much higher than the gain g = 6.9 dB found with the deterministic approach for a very similar device [12]. The designed Er^{3+}-doped chalcogenide microsphere amplifier, evanescently coupled with a tapered fiber, is very promising and could find interesting applications. However some technological efforts have to be dedicated in

future to overcome some drawbacks such as the fragility of the very tiny fiber taper, as the use of an integrated optical system.

Moreover the model using WGM resonance and PSO approach is used for a complete and robust characterization of rare-earth doped glasses. The innovative procedure follows two subsequent steps in order to mitigate the effect of uncertainty on geometrical dimensions. In the first one, the geometrical parameters are recovered. In the second step, the spectroscopic characterization is performed. The largest error in geometrical characterization is 0.03% obtained on the gap between microsphere and taper fiber. The errors on the spectroscopic parameters are less than that provided by high-cost measurement instruments. The errors made on the up-conversion coefficients C_{up} and C_3 and the branching ratio β_{32} are 0.75%, 0.05% and 0.42%, respectively. The recovering of rare-earth parameters via PSO is successfully applied in standard fiber amplifiers, but WGM resonance allows much higher accuracy. Indeed, WGMs propagate in the resonators along circular orbits allowing the interaction of the electromagnetic field with the structure for long effective distances.

The developed characterization tool is very versatile: it can be applied to the characterization of different kinds of rare-earths. Moreover it could be applied to develop innovative sensing systems. For example it can be applied to the set-up constituted by a passive microsphere surrounded with a medium or for a microbubble containing a polluted solution. The parameters related to the analyte concentration could be recovered via simple transmittance measurements instead of resonance wavelength-shift via optical spectrum analyzer.

Some efforts are dedicated to the development of a model for the design of all-in-fiber coupling system allowing quasi-distributed and wavelength selective addressing. The system is based on a micro-resonator excited by taper fiber with two identical LPGs on the sides. Using different pairs of identical LPGs operating in different wavelength bands allows selective coupling of different micro-resonators by using the same optical link. The model is validated using microspheres and microbubbles. Furthermore the feasibility of a glucose sensor based on microbubble set-up is investigated.

Whereas microspheres have interesting properties, such as very high quality factors and exceptionally low modal volume, the general trend is to privilege planar structures like micro-disks in order to obtain circuit integration, stability and cost-saving manufacturing. A numerical model is developed in order to simulate a lasing system based on rare-earth doped micro-disk coupled to two ridge waveguides. Firstly, the model is validated simulating an erbium doped chalcogenide micro-disk emitting at 4.5 μm. Then, novel design of a praseodymium-doped chalcogenide micro-disk emitting at 4.7 μm is developed. A number of promising applications in different areas such as biology, molecular spectroscopy and environmental monitoring are feasible.

List of publications

Peer-reviewed scientific articles:

1. G. Palma, P. Bia, L. Mescia, T. Yano, V. Nazabal, J. Taguchi, A. Moréac, F. Prudenzano, "Design of fiber coupled Er3+: Chalcogenide microsphere amplifier via particle swarm optimization algorithm," *Optical Engineering*, vol. 53, no. 7, pp. 071805-071805, July 2014.
2. G. Palma, P. Bia, L. Mescia, T. Yano, V. Nazabal, J. Taguchi, A. Moréac, F. Prudenzano, "Chalcogenide glass microspheres for biosensing, (invited)" *SPIE Newsroom*, 18 March 2014.
3. G. Palma, C. Falconi, V. Nazabal, T. Yano, T. Kishi, T. Kumagai, M. Ferrari, F Prudenzano, "Modeling of Whispering Gallery Modes for Rare Earth Spectroscopic Characterization," *IEEE Photonics Technology Letters*, vol. 27, no. 17, pp. 1861-1863, September 2015.
4. W. Scarcia, G. Palma, M. C. Falconi, F. de Leonardis, V. M. N. Passaro, F. Prudenzano, "Electromagnetic Modelling of Fiber Sensors for Low-Cost and High Sensitivity Temperature Monitoring," *Sensors*, vol. 15, no. 12, pp. 29855-29870, November 2015.
5. M. C. Falconi, G. Palma, F. Starecki, V. Nazabal, J. Troles, S. Taccheo, M. Ferrari, F. Prudenzano, "Design of an Efficient Pumping Scheme for Mid-IR Dy3+:Ga5Ge20Sb10S65 PCF Fiber Laser" *IEEE Photonics Technology Letters*, vol. 28, no. 18, pp. 1984-1987, September 2016.
6. G. Palma, M. C. Falconi, F. Starecki, V. Nazabal, T. Yano, T. Kishi, T. Kumagai, F. Prudenzano, "Novel double step approach for optical sensing via microsphere WGM resonance," *Optics Express*, vol. 24, Issue 23, pp. 26956-26971, November 2016.
7. M. C. Falconi, G. Palma, F. Starecki, V. Nazabal, J. Troles, J.-L. Adam, S. Taccheo, M. Ferrari, F. Prudenzano, "Dysprosium-Doped Chalcogenide Master Oscillator Power Amplifier (MOPA) for Mid-IR Emission," *Journal of Lightwave Technology*, vol. PP, no. 99, pp. 1-1, November 2016.

8. L. Bodiou, F. Starecki, V. Nazabal, J. Lemaitre, J-L Doualan, E. Baudet, R. Chahal, A. Gutierrez-Arroyo, Y. Dumeige, I. Hardy, A. Braud, R. Soulard, P. Camy, P. Nemec, G. Palma, F. Prudenzano, J. Charrier, "Mid-infrared guided photoluminescence from integrated Pr3+-doped selenide ridge waveguides". Submitted for publication to *Applied Physics Letters*.
9. G. Palma, M. C. Falconi, F. Starecki, V. Nazabal, J. Ari, L. Bodiou, J. Charrier, Y. Dumeige, E. Baudet and F. Prudenzano, "Design of Praseodymium-Doped Chalcogenide Micro-Disk Emitting at 4.7 μm,. Submitted for publication to *Journal of Lightwave Technology (2017)*.

Conference proceedings:

1. G. Palma, L. De Palma, T. Yano, V. Nazabal, T. Kishi, A. Moreac, M. Ferrari, D. Ristic, A. Lukowiak, G. C. Righini, G. Nunzi Conti, F. Prudenzano, "Fiber coupled erbium doped microsphere: NIR and mid-IR wavelength ranges," *16th International Conference on Transparent Optical Networks* (ICTON), Graz (Austria), July 6th-10th, 2014.
2. G. Palma, T. Castellano , O. Losito, T. Yano, V. Nazabal, J. Taguchi, A. Moréac, F. Prudenzano, "Fiber coupled Er3+:chalcogenide microsphere amplifier operating at 4.5 micron wavelength," *16º Convegno italiano delle tecnologie fotoniche* (FOTONICA), Napoli (Italia), May 12th-14th, 2014.
3. G. Palma, T. Castellano, O. Losito, T. Yano, V. Nazabal, J. Taguchi, A. Moréac, M. Ferrari, F. Prudenzano, "Fiber coupled Er3+:chalcogenide microsphere amplifier in Mid-IR wavelength range," *3th Mediterranean Photonics Conference*, Trani (Italy), May 7th-9th, 2014.
4. G. Palma, L. De Palma, T. Yano, V. Nazabal, J. Taguchi, A. Moréac, F. Prudenzano, "Feasibility investigation of fiber coupled Er3+:chalcogenide microsphere amplifier in Mid-IR," *5th International Workshop on Photoluminescence in Rare Earth* (PRE), San Sebastian (Spain), May 14th-16h, 2014.

5. G. Palma, L. De Palma, T. Yano, V. Nazabal, T. Kishi, A. Moréac, M. Ferrari, F. Prudenzano, "Exploitation of Whispering Gallery Mode Resonances for Characterization of Rare-Earth Doped Glass Devices," *20ª Riunione Nazionale di Elettromagnetismo* (RINEM), Padova (Italia), September 15th – 18th, 2014.
6. M.C. Falconi, W. Scarcia, G. Palma, R. Chahal, F. Starecki, V. Nazabal, J. Troles, J.-L. Adam, F. Prudenzano, "Optimization of Mid-IR microstructured fiber laser based on dysprosium doped chalcogenide glass," *17th International Conference on Transparent Optical Networks* (ICTON), Budapest (Hungary), July 5th-9th, 2015.
7. T. Landeau, O. Losito, G. Palma, V. Portosi, A. Jouanneaux, F. Prudenzano, "Multiple rhombus monopole antenna," *German Microwave Conference* (GeMiC), Nuremberg (Germany), March 16th-18th, 2015.
8. W. Scarcia, M. Surico, G. Palma, C. Falconi, C.E. Campanella, F. De Leonardis, V.M.N. Passaro, F. Prudenzano, "Design of an Integrated Optical Fiber Temperature Sensor for Harsh Environment," *17º Convegno italiano delle tecnologie fotoniche* (FOTONICA), Torino (Italia), May 6th - 8th, 2015.
9. F. Prudenzano, M.C. Falconi, W. Scarcia, G. Palma, V. Nazabal, J. Troles, R. Chahal, F. Starecki, "Design of MID-IR Fiber Laser Based on Dysprosium Doped Chalcogenide Glass," *17º Convegno italiano delle tecnologie fotoniche* (FOTONICA), Torino (Italia), May 6th -8th, 2015.
10. M.C. Falconi, G. Palma, R. Chahal, F. Starecki, V. Nazabal, J. Troles, J.-L. Adam, F. Prudenzano, "Design of mid-IR microstructured fiber light source based on dysprosium doped chalcogenide glass," *15th IEEE Mediterranean Microwave Symposium* (MMS), Lecce (Italy), November 30th – December 2th, 2015.
11. G. Palma, M.C. Falconi, F. Starecki, V. Nazabal, France, J. Charrier, L. Bodiou , F. Prudenzano, "Rare-Earth Doped Microdisks for Mid-Infrared Applications," *18º Convegno italiano delle tecnologie fotoniche* (FOTONICA), Roma (Italia), June 6th - 8th, 2016.

12. M.C. Falconi, G. Palma, F. Starecki, V. Nazabal, J. Troles, S. Taccheo, M. Ferrari, F. Prudenzano, "Design of a High Efficiency Mid-IR laser at 4400 nm," *18º Convegno italiano delle tecnologie fotoniche* (FOTONICA), Roma (Italia), June 6th - 8th, 2016.
13. M. C. Falconi, G. Palma, F. Starecki, V. Nazabal, J. Troles, J. L. Adam, S. Taccheo, M. Ferrari, F. Prudenzano, "Novel pumping schemes of mid-IR photonic crystal fiber lasers for aerospace applications (Invited)," *18th International Conference on Transparent Optical Networks* (ICTON), Trento (Italy), July 10th-14th, 2016.
14. G. Palma, M. C. Falconi, F. Starecki, V. Nazabal, L. Bodiou, Y. Dumeige, J. Lemaitre, J. Charrier, F. Prudenzano, "Design of rare-earth doped chalcogenide microresonators for biosensing in mid-IR," *18th International Conference on Transparent Optical Networks* (ICTON), Trento (Italy), July 10th-14th, 2016.
15. G. Palma, M. C. Falconi, F. Starecki, V. Nazabal, L. Bodiou, Y. Dumeige, J. Lemaitre, J. Charrier, F. Prudenzano, "Design of Erbium Doped Chalcogenide Microdisk Emitting at 4.5 μm," *21ª Riunione Nazionale di Elettromagnetismo* (RINEM), Parma (Italia), September 12th – 14th, 2016.
16. M. C. Falconi, G. Palma, F. Starecki, V. Nazabal, J. Troles, S. Taccheo, M. Ferrari, F. Prudenzano, "Dysprosium-doped Chalcogenide Fiber Laser for Medical Applications," *21ª Riunione Nazionale di Elettromagnetismo (RINEM)*, Parma (Italia), September 12th – 14th, 2016.
17. M. C. Falconi, G. Palma, A. Ameruoso, C. Laterza, S. Popolizio, L. Rinaldi, A. Rizzi, G. Testa, F. Tragni, F. Chiavaioli, F. Baldini, D. Farnesi, G. Nunzi Conti, S. Pelli, G. C. Righini, S. Soria, C. Trono, F. Prudenzano, "Design of Microspheres and Microbubbles for Environmental Chemical/Biological Optical Sensing". Submitted to *IEEE International Instrumentation and Measurement Technology Conference*, Torino (Italia), May 22th – 25th, 2017.

Publications without peer review process:

1. O. Losito, T. Castellano, C. Grisorio, F. Illuzzi, D. Laneve, M. Palieri, G. Palma, V. Portosi, D. Mencarelli, W. Scarcia, G. Venanzoni, M. Bozzetti, F. Prudenzano, "Design and Fabrication of Microwave Devices and Radiating Systems for Satellite Communication via Substrate Integrated Waveguide (SIW) Technology," *1st WORKSHOP on the State of the art and Challenges of Research Efforts at POLIBA*, Bari (Italy), December 3th – 5th, 2014.
2. F. Adamo, G. Andria, F. Attivissimo, N. Bellantuono, M. Ben Meftah, G. Cavone, D. Ettorre, F. De Serio, D. De Padova, G. De Santis, A. Di Nisio, D. Laneve, G. Intini, A.M.L. Lanzolla, L. Liberti, M. Mossa, M. Notarnicola, G. Palma, A. F. Petrillo, P. Pontrandolfo, V. Portosi, F. Prudenzano, W. Scarcia, B.Scozzi, M. Spadavecchia, "Development of a Flexible and Scalable System for Environmental Measurement Network," *1st WORKSHOP on the State of the art and Challenges of Research Efforts at POLIBA - Ongoing Research Projects-Grandi progetti di ricerca*, Bari (Italy), December 3th – 5th, 2014.
3. V. Portosi, G. Palma, T. Landeau, A. L. Ricchiuti, F. Prudenzano, "SIW and Optical Technologies in MOE-Lab at Magna Grecia Center, Politecnico di Bari," *Conference on substrate integtrated waveguides and related Technology (CSIWT)*, Bari (Italy), May 15th, 2015.

Bibliography

[1] L. Mescia, P. Bia, O. Losito, F. Prudenzano, "Design of Mid-IR Er^{3+} - Doped Microsphere Laser," *IEEE Photonics Journal*, vol. 5, no.4 , 2013.

[2] G. Righini, Y. Dumeige, P. Féron, M. Ferrari, G. Nunzi Conti, D. Ristic, S. Soria, "Whispering gallery mode microresonators, Fundamentals and applications, "*Rivista del Nuovo Cimento*," Società Italiana di Fisica, vol. 34, no. 7, pp.435-488, 2011.

[3] P. Girault, N. Lorrain, J. Lemaitre, L. Poffo, M. Guendouz, I. Hardy, M. Gadonna, A. Gutierrez, L. Bodiou, J. Charrier, "Racetrack micro-resonators based on ridge waveguides made of porous silica," *Optical Materials*, vol. 50, no. B, pp.167-174, 2015.

[4] H. Lin, L. Li, Y. Zou, S. Danto, J. D. Musgraves, K. Richardson, S. Kozacik, M. Murakowski, D. Prather, P. T. Lin, V. Singh, A. Agarwal, L.l C. Kimerling, J. Hu, "Demonstration of high-Q mid-infrared chalcogenide glass-on-silicon resonators," *Optics Letters*, vol. 38, no. 9, pp. 1470-1472, 2013.

[5] T. Yano, T. Kishi, T. Kumagai, " Glass Microspheres for Optics," *International Journal of Applied Glass Science*, vol. 6, no.4, pp. 375 – 386, 2015.

[6] B. E. Little, J. P. Laine, and H. A. Haus, "Analytic Theory of Coupling from Tapered Fibers and Half-Blocks into Microsphere Resonators," *Journal of Lightwave Technology*, vol. 17, no. 4, pp. 704–715, 1999.

[7] P. Bia, "Progetto di nanosfere drogate con terre rare per la generazione di segnale nell'infrarosso," Master's Thesis, Department of Electrical and Information Engineering, Technical University of Bari, 2010.

[8] G. Palma, "Progetto di Microsfere per applicazioni laser," Master's Thesis, Department of Electrical and Information Engineering, Technical University of Bari, 2013.

[9] A. H. W. Choi, "(Al,Ga)N Microdisk Cavities," in *Handbook of Optical Microcavities*, 1st ed. Pan Stanford Publishing Pte. Ltd., 2015.

[10] R.R.A.Syms, J.R.Cozens, "The slab waveguide," in *Optical Guided Waves and Devices*, 1st ed. McGraw-Hill Companies, Dec. 1992.

[11] B. E. Little, S. T. Chu, H. A. Haus, J. Foresi, J. P. Laine, "Microring resonator channel dropping filters," *Journal of Lightwave Technology*, vol. 15, no. 6, pp. 998–1005, 1997.

[12] L. Mescia, P. Bia, M. De Sario, A. Di Tommaso, F. Prudenzano, "Design of mid-infrared amplifiers based on fiber taper coupling to erbium-doped microspherical resonator," *Optics Express*, vol. 20, no. 7, pp. 7616–7629, 2012.

[13] L. Mescia, F. Prudenzano, M. De Sario, T. Palmisano, M. Ferrari, G. C.Righini, "Design of Rare-Earth-Doped Microspheres," *IEEE Photonics Technology Letters*, vol. 22, pp. 422-424, 2010.

[14] M. Borselli, T. J. Johnson, O. Painter, "Beyond the Rayleigh scattering limit in high-Q silicon microdisks: theory and experiment," *Optics Express*, pp. 1515 – 1530, vol. 13, no. 5, 2005.

[15] C. A. Balanis, *Advanced Engineering Electromagnetics*, 2nd ed., Wiley, May 1989.

[16] A. B Seddon, Z. Tang, D.d Furniss, S. Sujecki, T. M Benson, "Progress in rare-earth-doped mid-infrared fiber lasers," *Optics Express*, vol. 18, no. 25, pp. 26704 – 26719, 2010.

[17] F. A. Tal, C. Dimas, J. Hu, A. Agarwal, L. C. Kimerling, "Simulation of an erbium-doped chalcogenide micro-disk mid-infrared laser source," *Optics Express*, vol. 19, no. 3, pp. 11951 – 11962, 2011.

[18] F. Starecki, F. Charpentier, J.L. Doualan, L. Quetel, K. Michel, R. Chahal, J. Troles, B. Bureau, A. Braud, P. Camy, V. Moizan, V. Nazabal, "Mid-IR optical sensor for CO2 detection based on fluorescence absorbance of Dy3+:Ga5Ge20Sb10S65 fibers," *Sensors and Actuators B: Chemical*, vol. 207, pp. 518-525, 2015.

[19] Z. Han, L. Zhang, L. C. Kimerling, A. M. Agarwal, "Integrated Midinfrared Laser Based on an Er-Doped Chalcogenide Microresonator," *IEEE Journal of Selected Topics in Quantum Electronics*, vol. 21, no. 1, 2015.

[20] Z. Tang, D. Furniss, M. Fay, H. Sakr, L. Sójka, N. Neate, N. Weston, S. Sujecki, T. M. Benson, A. B. Seddon, "Mid-infrared photoluminescence in small-core fiber of praseodymium-ion doped selenide-based chalcogenide glass," *Optical Material Express*, vol. 5, no.4, pp. 870 – 886, March 2015.

[21] M. L. Gorodetsky, V. S. Ilchenko, "Optical microsphere resonators: optimal coupling to high-Q whispering-gallery modes," *Journal of the Optical Society of America B*, vol. 16, pp. 147-154, 1999.

[22] Chang-Ling Zou, Y. Yang, Chun-Hua Dong, Yun-Feng Xiao, Xiao-Wei Wu, Zheng-Fu Han, Guang-Can Guo, "Taper-microsphere coupling with numerical calculation of coupled-mode theory," *Journal of the Optical Society of America B*, vol. 25, pp. 1895-1898, 2008.

[23] H.A. Haus, *Waves and fields in optoelectronics*, Prentice Hall Inc., New Jersey (1984).

[24] M.J.F. Digonnet, *Rare-Earth-Doper Fider Lasers and Amplifiers*, New York: Marcel Dekker Inc. (2001).

[25] K. Vahala, *Optical microcavities*, World Scientific Publishing, Singapore, (2004).

[26] A.W. Snyder, J.D. Love, *Optical Waveguide Theory*, Chapman and Hall, London (1988).

[27] F. Prudenzano, L. Mescia, L. Allegretti, V. Moizan, V. Nazabal, F. Smektala, "Theoretical Study of Cascade Laser in Erbium-Doped Chalcogenide Glass Fibers," *Optical Materials*, vol. 33, no. 2, pp. 241–245, 2010.

[28] V. Moizan, V. Nazabal, J. Troles, P. Houizot, J.-L. Adam, F. Smektala, G. Gadret, S. Pitois, J.-L. Doualan, R. Moncorgé, G. Canat, "Er3+-doped GeGaSbS glasses for mid-IR fibre laser application: Synthesis and rare earth spectroscopy," *Optical Materials*, vol.31, no. 1, pp. 39-46, 2008.

[29] G. Palma, P. Bia, L. Mescia, T. Yano, V. Nazabal, J. Taguchi, A. Moréac, and F. Prudenzano "Design of fiber coupled Er3+: chalcogenide microsphere amplifier via particle swarm optimization algorithm," *Optical Engineering*, vol. 53, no. 7, pp. 071805-071805-8, 2013.

[30] J. Robinson, Y. Rahmat-Samii, "Particle Swarm Optimization in Electromagnetics," *IEEE Transaction on Antennas and Propagation*, vol. 52, no. 2, pp. 397-407, 2004.

[31] N. Jin, Y. Rahmat-Samii, "Advances in Particle Swarm Optimization for Antenna Designs: Real-Number, Binary, Single-Objective and Multiobjective Implementations," *IEEE Transaction on Antennas and Propagation* , vol. 55, no. 3, pp. 556-567, 2007.

[32] A. Giaquinto, L. Mescia, G. Fornarelli, and F. Prudenzano, "Particle swarm optimization-based approach for accurate evaluation of upconversion parameters in Er3+-doped fibers," *Optics Letters*, vol.36, no. 2, pp. 142–144, 2011.

[33] L. Mescia, A. Giaquinto, G. Fornarelli, G. Acciani, M. De Sario, F. Prudenzano, "Particle swarm optimization for the design and characterization of silica-based photonic crystal fiber amplifiers," *Journal of Non-Crystalline Solids*, vol. 357, no. 8-9, pp. 1851–1855, 2011.

[34] C. A. Coello Coello, G. T. Pulido, M. S. Lechuga, "Handling Multiple Objectives With Particle Swarm Optimization," *IEEE Transactions on Evolutionary Computation*, vol. 8, no. 3, pp. 256–270, 2004.

[35] F. Prudenzano, L. Mescia, A. D'Orazio, M. De Sario, V. Petruzzelli, A. Chiasera, M. Ferrari, "Optimization and Characterization of Rare Earth Doped Photonic Crystal Fiber Amplifier Using Genetic Algorithm," *Journal of Lightwave Technology*, vol. 25, pp. 2135–2142, 2007.

[36] S. Girard, L. Mescia, M. Vivona, A. Laurent, Y. Ouerdane, C. Marcandella, F. Prudenzano, A. Boukenter, T. Robin, P. Paillet, V. Goiffon, M. Gaillardin, B. Cadier, E. Pinsard, M. Cannas, R. Boscaino, "Design of Radiation-Hardened Rare-Earth Doped Amplifiers through a Coupled Experiment/Simulation Approach," *Journal of Lightwave Technology*, vol. 31, pp. 1247-1254, 2013.

[37] A. B. Matsko, and V. S. Ilchenko, "Optical Resonators With Whispering-Gallery Modes—Part I: Basics," *IEEE Journal of Selected Topics in Quantum Electronics*, vol. 12, no. 1, pp. 3-13, 2006.

[38] M. L. Gorodetsky and V. V. Ilchenko, "High-Q optical whisperinggallery microresonators: Precession approach for spherical mode analysis and emission patterns with prism couplers," *Optics Communications*, vol. 113, pp. 133–143, 1994.

[39] A. Serpenguzel, S. Arnold, and G. Griffel, "Excitation of resonances of microspheres on an optical fiber," *Optics Letters*, vol. 20, no. 7, pp. 654–656, 1995.

[40] F. Treussart, N. Dubreuil, J. C. Knight, V. Sandoghdar, J. Hare, V. Lefevre-Seguin, J. M. Raimond, and S. Haroche, "Microlasers based on silica microspheres," *Annales Des Télécommunications,* vol. 52, no. 11–12, pp. 557–568, 1997.

[41] J. C. Knight, G. Cheung, F. Jacques, and T. A. Birks, "Phase-matched excitation of whispering gallery mode resonances using a fiber taper," *Optics Letters*, vol. 22, no. 15, pp. 1129–1131, 1997.

[42] Hai-Cang Ren, F. Vollmer, S. Arnold, A. Libchaber, "High-Q microsphere biosensor-analysis for adsorption of rodlike bacteria," *Optics Express*, vol. 15, pp. 17410-17423, 2007.

[43] F. Vollomer, A. Stephen, "Whispering-gallery-mode biosensing: label-free detection down to single molecules," *Nature Methods*, vol.5, pp. 591-596, 2008.

[44] L. Yang, K. J. Vahala, "Gain functionalization of silica microresonators," *Optics Letters*, vol. 28, pp. 592-594, 2003.

[45] P. Wang, M. Ding, T. Lee, G. S. Murugan, L. Bo, Y. Semenova, Q. Wu, D.Hewak, G. Brambilla, G. Farrell, "Packaged chalcogenide microsphere resonator with high Q-factor," *Applied Phisics Letters*, vol. 102, pp. 131110 1-5, 2013.

[46] G. S. Murugan, M. N. Zervas, Y. Panitchob, J. S. Wilkinson, "Integrated Nd-doped borosilicate glass microsphere laser," *Optics Letters*, vol. 36, pp. 73-75, 2011.

[47] S.Y. Chen, T. Sun, K.T.V. Grattan, K. Annapurna, R. Sen, "Characteristics of Er and Er–Yb–Cr doped phosphate microsphere fibre lasers," *Optics Communications*, vol. 282, pp. 3765–3769, 2009.

[48] P. Feron, "Whispering Gallery Mode Lasers in Erbium doped fluoride glasses," *Annales de la Fondation Louis de Broglie*, vol. 29, pp. 317-329, 2004.

[49] G. Nunzi Conti, A. Chiasera, L. Ghisa, S. Berneschi, M. Brenci, Y. Dumeige, S. Pelli, S. Sebastiani, P. Feron, M. Ferrari and G.C. Righini, "Spectroscopic and lasing properties of Er3+ doped glass microspheres," *Non-Crystalline Solids*, vol. 352, pp. 2360–2363, 2006.

[50] K. Miura, K. Tanaka, K. Hirao, "CW laser oscillation on both the 4F3/2 –4I11/2 and 4F3/2 –4I13/2 transitions of Nd3+ ions using a fluoride glass microsphere," *Journal of Non-Crystalline Solids*, vol. 213-214, pp. 276–280, 1997.

[51] G.R. Elliot, D.W. Hewak, G. Senthil Murugan, JS. Wilkinson, "Chalcogenide glass microspheres; their production, characterization and potential," *Optics Express*, vol. 15, pp. 17542-17553, 2007.

[52] P. Wang, G. S. Murugan, G. Brambilla, M. Ding, Y. Semenova, Q. Wu, and G. Farrell, "Chalcogenide Microsphere Fabricated from Fiber Tapers Using Contact With a High-Temperature Ceramic Surface," *IEEE Photonics Technology Letters*, vol. 24, no. 13, pp.1103-1105, 2012.

[53] C. Grillet, S. N. Bian, E. C. Magi, and B. J. Eggleton, "Fiber taper coupling to chalcogenide microsphere modes," *Applied Physics Letters,* vol. 92, no. 17, pp. 171109–171111, 2008.

[54] D. H. Broaddus, M. A. Foster, I. H. Agha, J. T. Robinson, M. Lipson, and A. L. Gaeta, "Silicon-waveguide-coupled high-Q chalcogenide microspheres," *Optics Express*, vol. 17, no. 8, pp. 5998–6003, 2009.

[55] T. Yano,S. Shibata, T. Kishi, "Fabrication of micrometer-size glass solid immersion lens," *Applied Physics B*, vol. 83, pp. 167-170, 2006.

[56] T. Kouki, T. Makoto, "Optical microsphere amplification system," *Optics Letters*, vol. 32, pp. 3197–3199, 2007.

[57] Y.G. Boucher, P. Féron, "Generalized transfer function: A simple model applied to active single-mode microring resonators," *Optics Communications*, vol. 282, pp. 3940–3947, 2009.

[58] J. Charrier, M. L. Anne, H. Lhermite, V. Nazabal, J. P. Guin, T. Jouan, F. Henrio, D. Bosc, and J. L. Adam, "Sulphide GaxGe25-xSb10S65 (x =0, 5) sputtered films: elaboration and optical characterisation of planar and rib optical waveguides," *Journal of Applied Physics*, vol.104, no. 7, pp. 073110, 2008.

[59] G. Palma, C. Falconi, V. Nazabal, T. Yano, T. Kishi, T. Kumagai, M. Ferrari, and F. Prudenzano, "Modeling of Whispering Gallery Modes for Rare Earth Spectroscopic Characterization," ," *IEEE Photonics Technology Letters*, vol. 27, no. 17, pp. 1861–1863, 2015.

[60] K. Kadono, T. Yazawa, S. Jiang, J. Porque, BC Hwang, N. Peyghambarian,"Rate equation analysis and energy transfer of Er^{3+}-doped Ga_2S_3-GeS_2-La_2S_3 glasses," *Journal of Non-Crystalline Solids*, vol. 331, pp. 79–90, 2003.

[61] G. Palma, M. C. Falconi, F. Starecki, V. Nazabal, T. Yano, T. Kishi, T. Kumagai, and F. Prudenzano, "Novel double step approach for optical sensing via microsphere WGM resonance," *Optics Express*, vol. 24, no. 23, pp. 26956 – 26971, 2016.

[62] N. Miri, and M. Mohammadzaheri, "Optical Sensing Using Microspheres With Different Size and Material," *IEEE Sensors Journal*, vol.14, no. 10, pp. 3593–3598, 2014.

[63] M. Charlebois, A. Paquet, L. S. Verret, K. Boissinot, M. Boissinot, M. G. Bergeron, and C. Nì Allen, "Differentiation Between Analyte Absorption and Homogenous Index Sensing in

WGM Biodetection," *IEEE Sensors Journal*, vol.13, no. 1, pp. 229–232, 2013.

[64] K. J. Vahala, "Optical microcavities," *Nature*, vol. 424, pp. 839–846, 2003.

[65] L. He, S. K. Özdemir, J. Zhu, W. Kim, and L. Yang, "Detecting single viruses and nanoparticles using whispering gallery microlasers," *Nature Nanotechnology*, vol. 6, pp. 428–432, 2011.

[66] S. Arnold, D. Keng, S. I. Shopova, S. Holler, W. Zurawsky, and F. Vollmer, "Whispering gallery mode carousel − a photonic mechanism for enhanced nanoparticle detection in biosensing," *Optics Express*, vol. 17, no. 8, pp. 6230–6238, 2009.

[67] Y-Z Yan, C-L Zou, S-B Yan, F-W Sun, J L, C-Y Xue, Y-G Zhang, L. Wang, W-D Zhang, and J-J Xiong, "Robust Spot-Packaged Microsphere-Taper Coupling Structure for In-Line Optical Sensors," *IEEE Photonics Technology Letters*, vol. 23, no. 22, pp. 1736–1738, 2011.

[68] J. M. Ward, P. Féron, and S. N. Chormaic, "A Taper-Fused Microspherical Laser Source," *IEEE Photonics Technology Letters*, vol. 20, no. 6, pp. 392–394, 2008.

[69] M. C. Falconi, G. Palma, F. Starecki, V. Nazabal, J. Troles, S. Taccheo, M. Ferrari, and F. Prudenzano, "Design of an Efficient Pumping Scheme for Mid-IR Dy3+:Ga5Ge20Sb10S65 PCF Fiber Laser," *IEEE Photonics Technology Letters*, vol. 28, no. 18, pp. 1984–1987, 2016.

[70] G. Palma, M. C. Falconi, F. Starecki, V. Nazabal, L. Bodiou, Y. Dumeige, J. Lemaitre, J. Charrier, and F. Prudenzano, "Design of rare-earth doped chalcogenide microresonators for biosensing in mid-IR", *18th International Conference on Transparent Optical Networks*, July 10th- 14th 2016, Trento, Italy.

[71] H. Yu, Q. Huang, and J. Zhao, "Fabrication of an optical fiber micro-sphere with a diameter of several tens of micrometers," *Materials*, vol. 7, pp. 4878-4895, 2015.

[72] Z. Tian, C. Chen, and D. V. Plant, "Single- and dual-wavelength fiber ring laser using fiber microdisk resonator," *IEEE Photonics Technology Letters*, vol. 22, no. 22, pp. 1644–1646, Nov. 15, 2010.

[73] Z. Tian, P. Bianucci, and D. V. Plant, "Fiber Ring Laser Using Optical Fiber Microdisk as Reflection Mirror," *IEEE Photonics Technology Letters*, vol. 24, no. 16, pp. 1396–1398, Aug. 15, 2012.

[74] S. Calvez, G. Lafleur, A. Larrue, P.-F. Calmon, A. Arnoult, G. Almuneau, and O. Gauthier-Lafaye, "Vertically Coupled Microdisk Resonators Using AlGaAs/AlOx Technology," *IEEE Photonics Technology Letters*, vol. 27, no. 9, May 2015.

[75] S. C. Eom and J. H. Shin, "Design and optimization of horizontal slot microdisk sensors," *IEEE Photonics Technology Letters*, vol. 25, no. 19, Oct. 2013.

[76] J. M. Ward, Y. Yang, and S. N. Chormaic, "Highly Sensitive Temperature Measurements With Liquid-Core Micro bubble Resonators," *IEEE Photonics Technology Letters*, vol. 25, no. 23, pp. 2350-2353 Dec. 2013.

[77] B. Ozel, R. Nett, T. Weigel, G. Schweiger, and A. Ostendorf, "Temperature sensing by using whispering gallery modes with hollow core fibers," *Measurement Science and Technology*, vol. 21, no. 9, pp. 094015–094020, 2010.

[78] C. H. Dong, L. He, Y.-F. Xiao, V. R. Gaddam, S. K. Ozdemir, Z.-F. Han, G.-C. Guo and L. Yang, "Fabrication of high-Q polydimethylsiloxane optical microspheres for thermal sensing," *Applied Physics Letters*, vol. 94, no. 24, pp. 231119–231121, 2009.

[79] J. M. Ward and S. Nic Chormaic, "Thermo-optical tuning of whispering gallery modes in Er:Yb co-doped phosphate glass microspheres," *Applied Physics B*, vol. 100, no. 4, pp. 847–850, 2010.

[80] Q. Ma, T. Rossmann, and Z. Guo, "Whispering-gallery mode silica microsensors for cryogenic to room temperature measurement," *Measurement Science and Technology*, vol. 21, no. 12, pp. 025310–025317, 2010.

[81] Z. P. Cai, L. Xiao, H. Y. Xu, and M. Mortier, "Point temperature sensor based on green decay in an Er:ZBLALiP microsphere," *Journal of Luminescence*, vol. 129, no. 12, pp. 1994–1996, 2009.

[82] N. M. Hanumegowda, C. J. Stica, B. C. Patel, I. White, and X. Fan, "Refractometric sensors based on microsphere resonators," *Applied Physics Letters*, vol. 87, no. 20, pp. 201107–201110, 2005.

[83] T. Ioppolo, U. K. Ayaz, and M. V. Ötügen, "High-resolution force sensor based on morphology dependent optical resonances of

polymeric spheres," *Journal of Applied Physics*, vol. 105, no. 1, pp. 013535–013544, 2009.

[84] R. Henze, T. Seifert, J. Ward, and O. Benson, "Tuning whispering gallery modes using internal aerostatic pressure," *Optics Letters*, vol. 36, no. 12, pp. 4536–4538, 2011.

[85] S. Soria, S. Berneschi, M. Brenci, F. Cosi, G. Nunzi Conti, S. Pelli, and G. C. Righini, "Optical Microspherical Resonators for Biomedical Sensing," *Sensors*, vol. 11, 785-805, 2011.

[86] D. Farnesi, F. Chiavaioli, F. Baldini, G. C. Righini, S. Soria, C. Trono, and G. Nunzi Conti, "Quasi-distributed and wavelength selective addressing of optical micro-resonators based on long period fiber gratings," *Optics Express*, vol. 23, no. 16 , pp. 21175-21180, 2015.

[87] G. Stewart, J. Norris, D. F. Clark, and B. Culshaw, "Evanescent wave chemical sensors – a theoretical evaluation," *International Journal of Optoelectronics*, vol. 6, no. 3, pp. 227-238, 1991.

[88] A. D'Orazio, M. De Sario, C. Giasi, L. Mescia, V. Petruzzelli, and F. Prudenzano, "Design of planar optic sensors for hydrocarbon detection", *Optical and Quantum Electronics*, vol. 36, pp. 507-526, 2004.

[89] Y. Jung, and J. Hwang, "Near-infrared studies of glucose and sucrose in aqueous solutions: water displacement effect and red shift in water absorption from water-solute interaction," *Applied Spectroscopy*, vol. 67, no. 2, 2013.

[90] G. Kim and J. H. Shin, "Luminescent silicon-rich nitride horizontal air-slot microdisk resonators for biosensing," *IEEE Photonics Technology Letters*, vol. 28, no. 21, Nov. 2016.

[91] M.-L. Anne, J. Keirsse, V. Nazabal, K. Hyodo, S. Inoue, C. Boussard-Pledel, H. Lhermite, J. Charrier, K. Yanakata, O. Loreal, J. Le Person, F. Colas, C. Compère, and B. Bureau, "Chalcogenide Glass Optical Waveguides for Infrared Biosensing," *Sensors*, vol. 9, pp. 7398-7411, Sept. 2009.

[92] E. Luzhansky, F.-S. Choa, S. Merritt, A. Yu, and M. Krainak, "Mid-IR free-space optical communication with quantum cascade lasers" *SPIE Proceedings*, vol. 9465, May 2015.

[93] J.-L. Adam, L. Calvez, J, Trolès, and V. Nazabal, "Chalcogenide Glasses for Infrared Photonics," *International Journal of Applied Glass Science*, vol. 6, no. 3, pp. 287-294, Aug. 2015.

[94] R. Chahal, F. Starecki, C. Boussard-Plédel, J. L. Doualan, K. Michel, L. Brilland, A. Braud, P. Camy, B. Bureau, and V. Nazabal, "Fiber evanescent wave spectroscopy based on IR fluorescent chalcogenide fibers," *Sensors and Actuators B: Chemical*, vol. 229, no. 28, pp. 209-216, June 2016.

[95] J. Hu, V. Tarasov, A. Agarwal, L. Kimerling, N. Carlie, L. Petit, and K. Richardson, "Fabrication and testing of planar chalcogenide waveguide integrated microfluidic sensor," *Optics Express*, vol. 15, no.5, pp. 2307-2314, Mar. 2007.

[96] J. Hu, J. D. Musgraves, N. Carlie, B. Zdyrko, I. Luzinov, A. Agarwal, K. Richardson, and L. Kimerling, "Development of chipscale chalcogenide glass based infrared chemical sensors," *SPIE Proceedings*, vol. 7945, Jan. 2011.

[97] A. K. Mairaj, C. Riziotis, A. M. Chardon, P. G. R. Smith, D. P. Shepherd, and D. W. Hewak, "Development of channel waveguide lasers in Nd3+-doped chalcogenide (Ga:La:S) glass through photoinduced material modification," *Applied Physics Letters*, vol. 81, no. 20, pp. 3708–3710, 2002.

[98] K. Sasagawa, Z.-o. Yonezawa, R. Iwai, J. Ohta, and M. Nunoshita, "S-band Tm3+-doped tellurite glass microsphere laser via a cascade process," *Applied Physics Letters*, vol. 85, no. 19, pp. 4325–4327, 2004.

[99] J. Wu, S. Jiang, T. Qua, M. Kuwata-Gonokami, and N. Peyghambarian, "2 μm lasing from highly thulium doped tellurite glass microsphere," *Applied Physics Letters*, vol. 87, no**.** 21, pp. 211118, 2005.

[100] A. L. Pele, A. Braud, J. L. Doualan, F. Starecki, V. Nazabal, R. Chahal, C. Boussard-Pledel, B. Bureau, R. Moncorge, and P. Camy, "Dy3+ doped GeGaSbS fluorescent fiber at 4.4 μm for optical gas sensing: Comparison of simulation and experiment," *Optical Materials*, vol. 61, pp. 37-44, Nov. 2016.

[101] R. C. Eberhart, Y. Shi, "Particle Swarm Optimization: Developments, Applications and Resources," Proceedings of the IEEE International Conference: Evolutionary Computation, vol. 1, pp. 81–86. Feb. 2001.